Synthesis of Highly Luminescent Cesium Tin Halide Perovskite Nanocrystals

(高発光効率セシウムスズハライドペロブスカイトナノ粒子の合成)

Binbin ZHANG

Graduate School of Chemical Sciences and Engineering

Hokkaido University

2024

Content

Abstract

Colloidal halide perovskite nanocrystals (NCs) have garnered substantial attention in recent years due to their excellent optoelectronic properties, which include tunable bandgaps, high photoluminescence efficiency, and substantial absorption coefficients. These attributes have propelled their widespread utilization across diverse optoelectronic applications, including lasers, light-emitting diodes, and solar cells. However, with the growing interest in using metal halide perovskite for optoelectronic devices, concerns about the toxicity of lead in lead-based halide perovskite materials make it necessary to look for lead-free alternatives. Tin halide perovskites have emerged as promising substitutes owing to their reduced toxicity and comparable perovskite-like characteristics. Nonetheless, the synthesis of high-quality colloidal $CsSnX_3$ (X= Cl, Br, I) perovskite NCs presents a formidable challenge, impeding their widespread adoption in next-generation optoelectronic applications. This thesis delves into the synthesis mechanism and precursor chemistry governing the formation of tin halide perovskite NCs, culminating in the development of effective synthetic methodologies conducive to yielding high-quality products.

Chapter 1 provides an introduction to the research background of metal halide perovskite materials, including synthetic methods for metal halide perovskites, and summarizes the effective strategies reported to enhance the optical properties of metal halide perovskite materials. Additionally, it outlines the research progress of tin-based halide perovskite NCs. Finally, it elucidates the research topic's conceptual framework.

In chapter 2, the investigation focuses on elucidating the precursor chemistry involved in the hot-injection synthesis method for representative tin halide perovskite NCs, particularly $CsSnI_3$ NCs. Through comprehensive analysis, including nuclear magnetic resonance (NMR) spectroscopy, significant insights are gleaned regarding the role of polymeric alkanoate iodides, formed as intermediate products during the reaction between tin and iodide precursors, in modulating NCs properties such as

photoluminescence quantum yield (PLQY), size, morphology, and uniformity.

In chapter 3, a straightforward method based on ion exchange is proposed, showcasing its effectiveness in generating high-quality $CsSnX_3$ NCs with excellent PLQY and adjustable size. $CsSnI_3$ NCs with a remarkable PLQY of 34.4% were obtained, surpassing the previously reported maximum value of 18.4%. The controlled reaction kinetics inherent in this approach enable the synthesis of NCs with excellent size uniformity, crucial for optoelectronic applications.

In chapter 4, further exploration into controlled ion exchange processes, facilitated by incorporating an additional tin source during the synthesis of $CsSnI_3$ NCs, unveils a pathway to enhance crystal quality. This endeavor resulted in a significant enhancement of the PLQY of $CsSnI_3$ NCs to 49.7%, accompanied by uniform size distribution. In-depth analysis, including in-situ photoluminescence (PL) and high-resolution transmission electron microscopy (HRTEM), elucidates the role of the additional tin source in accelerating the reaction rate that minimizes uncoordinated Sn and I atoms and thus boosts the PLQY of $CsSnI_3$ NCs. Additionally, the versatility of this methods is demonstrated through the synthesis of tin halide perovskite NCs with varied halide compositions.

In summary, this thesis advances the understanding of synthesis strategies for high-quality tin halide perovskite NCs, offering valuable insights into precursor chemistry, reaction mechanisms, and synthetic methodologies. The developed approaches hold immense potential for facilitating the widespread utilization of tin halide perovskite NCs in diverse optoelectronic applications, thereby propelling the evolution of next-generation optoelectronic devices.

Chapter 1 Introduction

1.1 General background for perovskite materials

1.1.1 Perovskite

Perovskite, initially discovered by German scientist Gustav Rose in 1839, was later named after Russian geologist Lev Perovski. Perovskite represents a category of materials with a crystal structure identical to that of $CaTiO_3$.[1] The material can be broadly classified into two categories: inorganic oxide perovskites, which have the general formula ABO_3, and metal halide perovskites, which have the general formula ABX_3 (Figure 1.1a), both sharing similar crystal structures.[2, 3] In the case of inorganic oxide perovskites, the A component typically includes alkali metals or rare earth metal cations such as Ca^{2+}, Sr^{2+}, K^+, La^{3+}, and Pr^{3+}, while the B component consists of transition metal cations like Ti^{3+}, Al^{3+}, and Cr^{3+}, among others.[4, 5] On the other hand, for metal halide perovskites, the A component can be a metal or an organic monovalent cation, such as Cs^+, Rb^+, FA^+ ($FA^+ = CH(NH_2)_2^+$; formamidinium), and MA^+ ($MA^+ = CH_3NH_3^+$; methylammonium).[6, 7] The B components represents divalent transition metal cations like Pb^{2+}, Sn^{2+}, and Ge^{2+}, while X stands for halide anions or their mixtures.[7-10] When the A cation is a metal such as Cs^+, it becomes a fully inorganic halide perovskite. In contrast, when A is an organic cation like FA^+ or MA^+, it is termed as organic–inorganic halide perovskite. Currently known perovskite compounds are predominantly oxides, constituting approximately 70%, while halides make up only about 16%.[11]

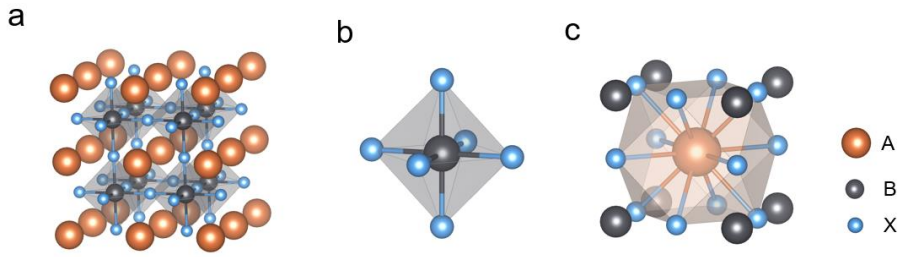

Figure 1.1 (a) An ideal cubic perovskite structure of ABX_3. (b) the coordination of B-site cation; and (c) the coordination of A-site cation.

The crystal structure of perovskite materials was deduced as early as the1900s.[6, 12, 13] Taking the example of the metal halide perovskite structure, B cations coordinate with X anions in a 6-fold coordination, forming an octahedral structure, while A cations coordinate with X anions in a 12-fold coordination (Figure 1.1b, c).[14-16] Therefore, the perovskite structure can be visualized as a network of corner-sharing [BX_6] octahedra with A cations occupying the interstitial spaces, ideally forming a stable cubic unit cell. The formation of an ideal cubic structure in perovskites imposes relatively strict requirements on the relative ion sizes of A, B, and X. Any alteration in the elemental composition or deformations due to other reasons will lead to the existence of perovskite structures with different symmetries, such as orthorhombic and tetragonal structures. In summary, the crystallographically stable structure of perovskites can be inferred using the Goldschmidt tolerance factor (t),[17-19] defined by the following equations:

$$t = \frac{r_A + r_X}{\sqrt{2}(r_B + r_X)}$$

Here, r_A is the radius of the A cation, r_B is the radius of B cation, and r_X is the radius of X anion. Typically, the t for perovskites with a stable perovskite phase structure falls within the range of 0.8–1.0.[17, 19, 20] Smaller t values are prone to distortions in the cubic structure, leading to a reduction in crystal symmetry. For instance, orthorhombic (γ phase) or tetragonal (β phase) structures may form (Figure 1.2), and the specific numerical values may vary slightly depending on the type of perovskite. Also, for a t greater than 1, the A cation is too large to form a perovskite structure, where a hexagonal structure will be formed instead of layers that, which includes face-sharing octahedra.[20] It is worth noting that to satisfy an appropriate t value, the A cation must be significantly larger than the B cation. In metal halide perovskites, the B site is typically occupied by large Pb or Sn atoms, necessitating a correspondingly large A cation. Therefore, A cations such as Cs, FA, and MA are commonly found to stabilize the perovskite structure.

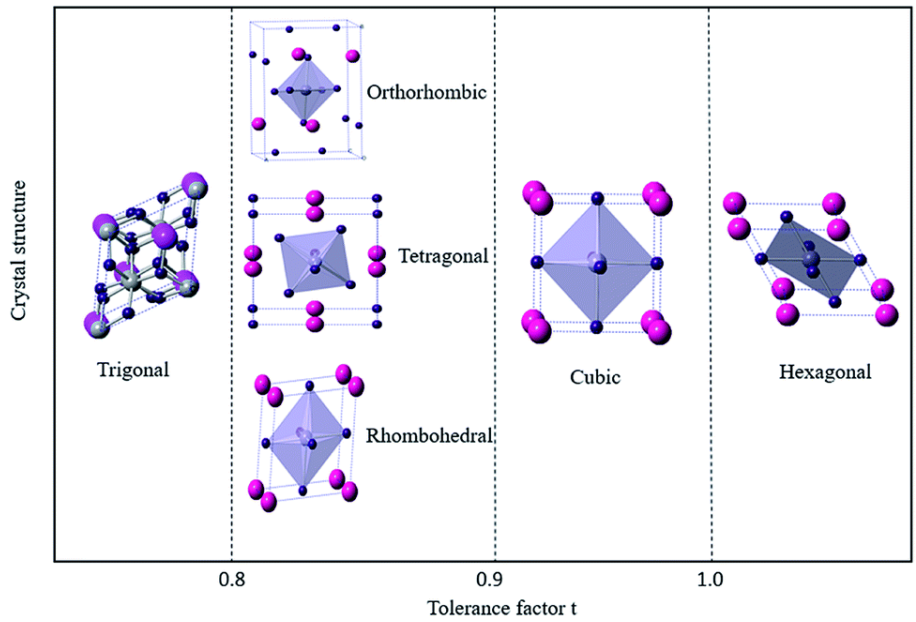

Figure 1.2 Correlation between the crystal structure of perovskite and value of tolerance factor t.[20]

Another crucial parameter determining the stability of perovskites is the octahedral factor (μ), as it is related to the stability of the [BX_6] octahedra. Its suitable range generally falls between 0.44 and 0.88,[17] and it is defined as follows:

$$\mu = \frac{r_B}{r_X}$$

Furthermore, besides having intriguing structures, perovskite materials also possess excellent performance, offering multiple applications. Perovskite materials made their initial appearance in devices in the 1990s and 2000s, as pioneered by Mitzi et al.,[21, 22] these materials experienced a period of relative obscurity. It wasn't until 2009 when Kojima et al. reported the use of metal halide perovskites as sensitizers in solar cells, achieving a notable photovoltaic conversion efficiency (PCE) of 3.1%.[23] This breakthrough propelled perovskite materials back into the spotlight. Since then, many scholars have contributed to the understanding and development of perovskite materials, making significant strides in the fields of structure, synthesis, and applications.

1.1.2 Crystal Structure and Band Gap Origins of Metal Halide Perovskites

Metal halide perovskites, a crucial subgroup of perovskite materials, stand out as a unique class of light-sensitive semiconductors. Their popularity arises from their easy

production, customizable band gaps, strong light absorption, weak exciton binding, and effective carrier diffusion, offering promising optoelectronic features. [10, 15] Metal halide perovskites are multi-component halide salts, display distinct ionic bonding characteristics, enabling synthesis at remarkably low temperatures.[24, 25] However, this ionic nature makes them prone to instability, especially susceptible to phase transitions. For example, $CsPbI_3$, a representative metal halide perovskite, exhibits four phases: cubic α phase (Pm3m), tetragonal β phase (P4/mbm), orthorhombic γ phase (Pbnm, commonly known as the black phase), and non-perovskite δ phase (Pnma, referred to as the yellow phase) (Figure 1.3).[17] These phases can transform under specific conditions, yet external factors like light, water, heat, oxygen, polar solvents, and ligands can trigger complete decomposition, posing challenges for stability.

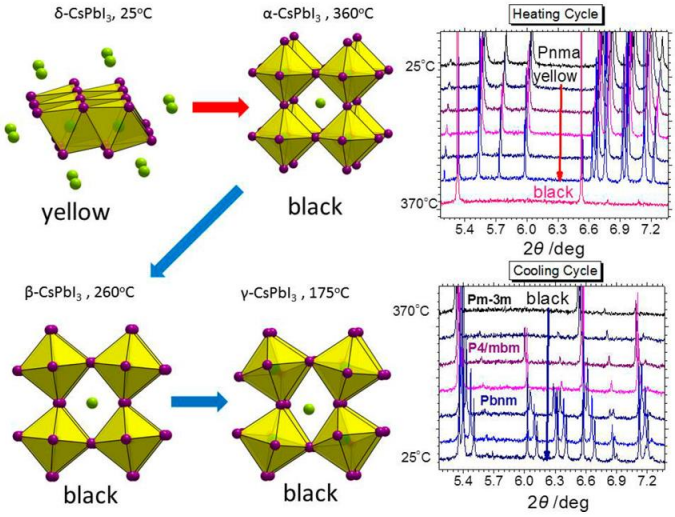

Figure 1.3 Phase transition scheme as observed with synchrotron powder diffraction (λ = 0.413906 Å) for the $CsPbI_3$ compound. Initially, the room temperature stable δ-phase (yellow) converts to the black perovskite α-phase upon heating above 360 °C. On cooling, the perovskite structure remains kinetically stabilized converting to the black perovskite β- and γ-phases at 260 and 175 °C, respectively. Full conversion of the γ- to the initial yellow δ-phase occurs after ~48h.[17]

The varied structures of metal halide perovskites contribute to fascinating optoelectronic properties. Classified as direct band gap semiconductors, their electronic structure has been extensively explored both theoretically and experimentally. In the case

of ABX_3-structured metal halide perovskites, the position of the valence band maximum (VBM) is primarily determined by the anti-bonding hybridization of B s orbitals and X np states orbitals (Figure 1.4a),[26, 27] with a significant contribution from X np orbitals (with n = 3, 4, 5 corresponding to X = Cl, Br, I). Conversely, the conduction band minimum (CBM) comprises B p and X np orbitals, with B p orbitals playing a major role. Hence, the B-X-B bond angles within the octahedra are crucial structural factors controlling the variation in band gaps (Figure 1.4b).[17, 28] For instance, studies have indicated that deviating the Sn-I-Sn bond angle away from 180°, where maximal orbital overlap occurs, leads to a diminished antibonding interaction between the Sn s orbitals and the I px and py orbitals, consequently causing shifts in the valence and conduction bands. Specifically, a reduction in the Sn-I-Sn bond angle results in an increase in the band gap (Figure 1.4c).[28]

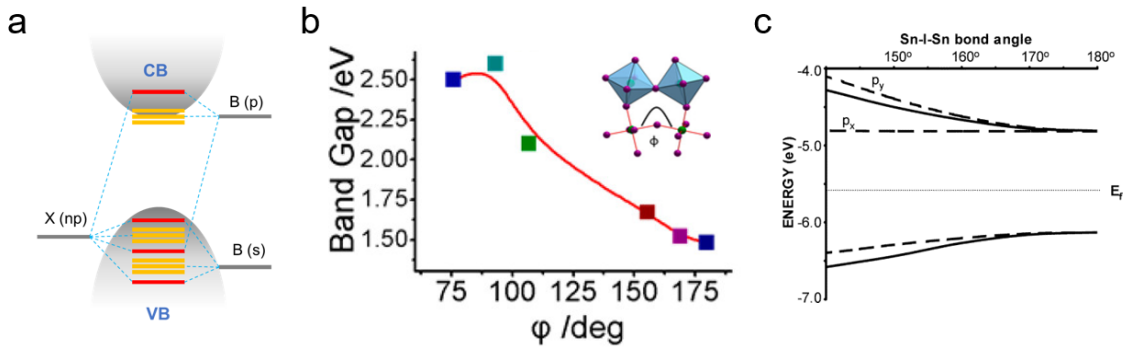

Figure 1.4 (a) Schematic of the electronic band structure of ABX_3 perovskite compound. Shaded regions show the valence band (VB) and conduction band (CB), and the thick lines represent the molecular orbital picture. (b) Experimental band gaps of $APbI_3$, highlight the influence of structural distortions and the connectivity of the $[PbI_6]^{4-}$ octahedra.[17] (c) Plot of the energy of the top of the valence band and bottom of the conduction bands upon in-plane (solid lines) and out-of-plane (dashed lines) distortions to the $[SnI_4]^{2-}$ perovskite lattice (calculated with an average Sn-I distance of 3.16 Å) which demonstrates the origin of the band gap variation with structural distortion. The Fermi energy is marked by a dotted line.[28]

Changing the halide ion from I to Br and then to Cl strengthens the binding of X p orbitals, inducing a significant downward shift of the VBM. This feature contributes to

the adjustable optical band gap in metal halide perovskite materials.

Although the A-site cations don't directly impact the electronic properties, they can induce lattice distortions through spatial and Coulomb interactions.[29] These distortions indirectly affect the hybridization of B and X atomic orbitals, resulting in changes in the band gap energy. For instance, replacing Cs with MA or FA in $CsSnCl_3$ results in a downward shift of the VBM, indicating an increased band gap.[29]

1.1.3 Optical Properties of Metal Halide Perovskites

Metal halide perovskite materials are renowned for their intriguing and outstanding optical characteristics, playing a crucial role in achieving high-performance optoelectronic devices. These properties include tunable emission spectra, high absorption coefficients, defect tolerance, among others.[10, 15]

Tunable Emission

Metal halide perovskites exhibit tunable emission colors, covering the visible spectrum and extending into the near-infrared range. By altering the halide composition from chlorine-rich to iodine-rich, the bandgap of metal halide perovskites gradually decreases, allowing for easy tuning of photoemission across the ultraviolet-visible-near-infrared wavelength range.[16] Additionally, adjusting the emission position can be achieved by modifying the B-site cations; for instance, substituting Pb^{2+} with Sn^{2+} significantly reduces the bandgap, further extending the emission towards the near-infrared. And the PL peaks for the $CsSnI_3$ at 950 nm. Owing to the band gap anomaly of Sn/Pb alloy perovskites, $MASn_{0.8}Pb_{0.2}I_3$ exhibits the most red-shifted peak at 1080 nm (1.15 eV) (Figure 1.5).[30-33]

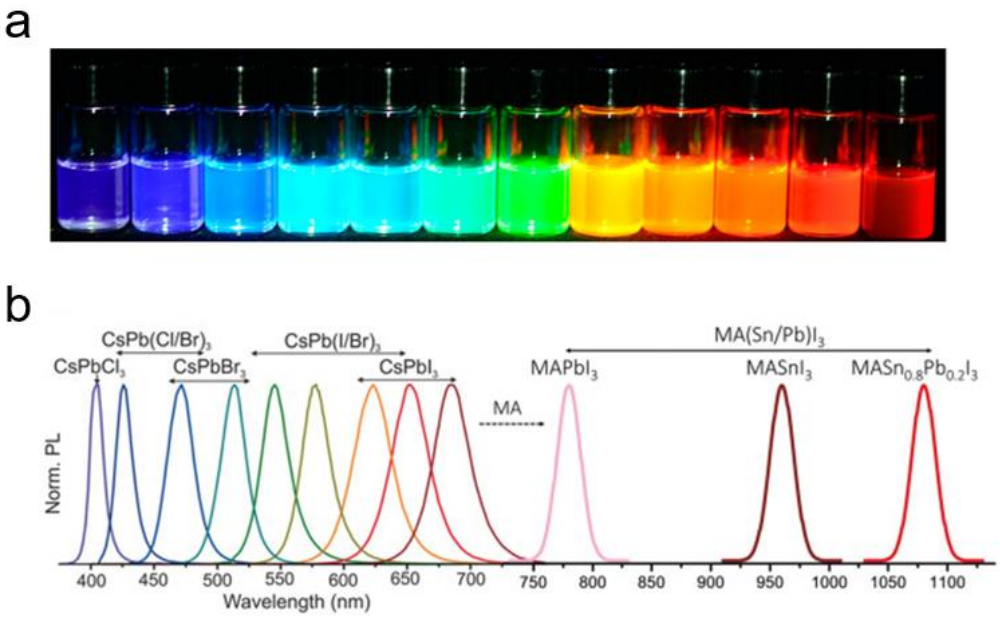

Figure 1.5 Band gap tunability for ABX_3 perovskite ranging from 1.15 to 3.06 eV. (a) Colloidal library of $CsPbX_3$ (X=Cl, Br, I) solutions under UV light (λ = 365 nm).[30] (b) Representative PL spectra of $CsPbX_3$ extended towards $MA(Sn/Pb)I_3$ perovskites.[30, 31]

Optical Absorption Characteristics

Similar to their luminescent performance, metal halide perovskite materials exhibit a rich and diverse optical absorption spectrum. Their absorption edge spans the entire visible light range and shows some absorption in the near-infrared region. Moreover, these materials demonstrate high absorption coefficients; for instance, research indicates that the absorption coefficient of $MAPbI_3$ in the visible light range can exceed 10^5 cm^{-1}, notably higher than second-generation solar cells like GaAs.[34] In the field of photovoltaics, efficient absorption in the visible light range is crucial for high-performance solar cells, making metal halide perovskites an ideal candidate for third-generation photovoltaic materials.

Defect Tolerance

The defect characteristics of semiconductors, especially intrinsic point defects, are always crucial for their performance.[35] Despite the low defect concentrations in traditional semiconductors (in the range of one part per million or one part per billion), defects significantly impact carrier mobility, lifetime, and recombination rates. Therefore,

a comprehensive understanding of defect properties is essential for practical applications. Metal halide perovskites, as direct bandgap semiconductors, exhibit photoluminescence (PL) even at room temperature. Remarkably, perovskite nanocrystals (NCs), unlike other semiconductor NCs without surface passivation, maintain high photoluminescence quantum yield (PLQY).[1, 36] This exceptional phenomenon is attributed to the high tolerance to defects, known as the defect tolerance effect. Several factors contribute to this effect.[1]

Firstly, among various point defects, only vacancy defects have relatively low formation energy, while interstitial defects and antisite defects are almost impossible to exist, despite forming deep trap states in the electronic structure. Secondly, due to the unique electronic structure of metal halide perovskite materials, vacancies only minimally affect the electronic structure, acting as shallow traps or forming deep localized states that do not capture charges. Thirdly, the soft and dynamic nature of the metal halide perovskite lattice seems to protect carriers from being captured and scattered Coupled with its partially ionic nature, the intense structural dynamics of the $[PbX_6]^{4-}$ lattice at room temperature results in strong coupling between electrons and holes with ionic displacements, forming polarons. These polarons reduce the scattering of carriers with defects and longitudinal optical phonons (Figure 1.6). Lastly, the type of A-site cation is not a crucial factor affecting defect tolerance;[37] moreover, the introduction of organic cations can increase the dielectric constant of perovskite materials. A high dielectric constant is advantageous for protecting carriers from the impact of grain boundary scattering and charged defects.[38]

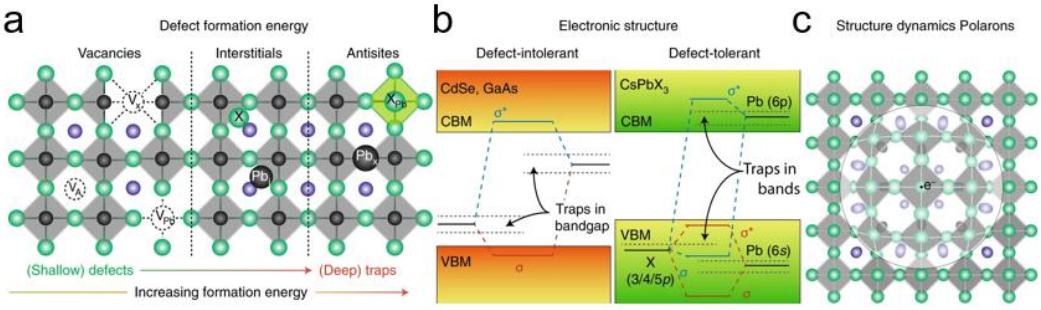

Figure 1.6 (a) Typical point defects in metal halide perovskite, including vacancies, interstitial and antisite atoms, in order of increasing formation energy (or decreasing probability of occurrence), and their depths in the bandgap.[1] (b) Schematic representation of electronic band structure of typical defect-intolerant semiconductors and metal halide perovskite. In conventional semiconductors, point defects or dangling bonds emerge as weak bonding or non-bonding states within the bandgap. In metal halide perovskite, defects states will thus form only shallow traps or will be enclosed in the conduction or valance band.[1] (c) Schematic representation of local structural deformation of the Pb–Br framework that, combined with a charge carrier (electron or hole), forms a polaron.[1]

1.1.4 Applications of Metal Halide Perovskites

The exceptional optical properties of metal halide perovskites have made them highly sought after in various optoelectronic applications, including solar cells,[23, 39, 40] light-emitting diodes (LEDs),[41-43] lasers,[44-46] and photodetectors.[47]

Perovskite Solar Cells

In the field of photovoltaics, metal halide perovskites have emerged as promising materials for highly efficient solar cells. The typical architecture of a perovskite solar cell involves using metal halide perovskite materials as the intrinsic light-absorbing semiconductor layer sandwiched between electron transport materials (ETM) and hole transport materials (HTM), with metal cathodes (e.g., Au) and transparent conductive oxide anodes (e.g., ITO) on either side. The working principle involves the absorption of sunlight by the metal halide perovskite layer, generating electron-hole pairs. These electrons and holes are then absorbed by the electron and hole transport layers, respectively, leading to the generation of electric current.

Since Miyasaka and colleagues first reported perovskite solar cells with a PCE of 3.8%,[23] these solar cells have garnered widespread attention. After a decade of development, the PCE of single-junction perovskite solar cells has been elevated to over 26%, and perovskite-silicon tandem solar cells have surpassed 33%.[48] This remarkable progress exceeds that of other commercial solar cell materials. While perovskite solar cells still face stability challenges, ongoing research positions metal halide perovskites as promising materials for highly efficient solar cells.

Metal Halide Perovskite LEDs

The tunable emission colors and high PLQYs of metal halide perovskite materials have attracted researchers to incorporate them into LEDs. Perovskite LEDs typically follow a sandwich structure similar to that of solar cells, including electrodes, an electron injection layer (EIL), a hole injection layer (HIL), and a metal halide perovskite emitting layer. The working principle involves injecting electrons and holes into the metal halide perovskite layer, leading to radiative recombination and light emission. While attempts to use metal halide perovskites in LEDs date back to the early 1990s, achieving room-temperature luminescence in metal halide perovskite LEDs has been a recent accomplishment.[49] Recently, external quantum efficiencies (EQE) of near-infrared (NIR), red, and green metal halide perovskite LEDs have significantly improved.[50-52]

Perovskite Lasers

Due to their high PLQY, large absorption coefficients, and low defect density, metal halide perovskites exhibit potential in laser applications. After successful demonstrations of low-threshold amplified spontaneous emission (ASE) in solution-processed $CsPbX_3$ (X = Cl, Br, and I) NCs,[53] research on metal halide perovskite lasers has extended to various geometries and MA、FA based perovskites.[44-46] As excitation intensity increases, the emission spectrum transitions from broad spontaneous emission (SE) to a narrow red-shifted peak, characteristic of ASE. By controlling the halide composition, laser wavelengths in these materials can be tuned across the entire visible to near-infrared range, further expanding the potential applications of metal halide perovskite materials in optical devices.

Perovskite Photodetectors

Photodetectors play a crucial role in converting light signals into electrical signals, essential for various applications such as sensors and optical communication devices. Due to their high absorption and excellent carrier transport properties, metal halide perovskites have emerged as promising materials for high-quality photodetectors.[47] Studies indicate

that the performance of perovskite photodetectors is as good as or even better than commercially available crystalline silicon (Si) and III-V photodetectors, presenting new opportunities for the development of perovskite materials in optoelectronic applications.[54]

1.2 Synthesis and Enhancement of Optical Properties of Metal Halide Perovskite NCs

1.2.1 Metal Halide Perovskite NCs

Metal halide perovskite NCs have emerged as a class of semiconductor nanomaterials with significant advantages. Compared to bulk materials, NCs often exhibit superior optoelectronic properties. Reducing the crystal size to the nanoscale often results in size-dependent optical and electronic characteristics.[55, 56] For instance, when the size of metal halide perovskite NCs approaches their Bohr radius, they exhibit distinct quantum confinement effects that can be utilized to tune the optical bandgap, similar to other semiconductor nanomaterials (Figure 1.7a). Polavarapu et al. achieved $CsPbBr_3$ NCs with sizes/thicknesses ranging from 20 nm to 2 nm by lowering the synthesis temperature, leading to a blue shift in the PL peak from 520 nm to 455 nm. It is noteworthy that the exciton Bohr radius of $CsPbBr_3$ is approximately 7 nm, and when the size approaches or falls below 7 nm,[30] the optical bandgap undergoes more pronounced changes with size (Figure 1.7b, c).[57] Moreover, metal halide perovskite NCs often demonstrate exceptionally high PLQY. To date, reported PLQY values for red, green, and blue metal halide perovskite NCs have approached 100%, exhibiting excellent narrow emission spectra.[58, 59]

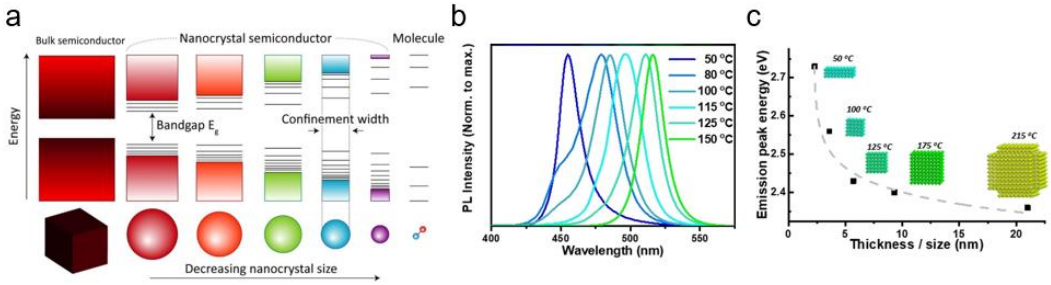

Figure 1.7 (a) Schematic representation of quantum confinement effect. Comparison of bulk, NCs and

molecules, indicating the size dependent bandgap of NCs and the formation of discrete states near the band edge.[55] (b) Normalized photoluminescent spectra of the $CsPbBr_3$ colloidal solutions synthesized at different reaction temperatures.[57] (c) Emission peak energy versus nanoplatelets thickness and cubic size. Dashed line is added as a guide the eye. Insets are the corresponding schematic representations of the structures obtained and the reaction temperature employed.[57]

Several methods have been utilized in the synthesis of metal halide perovskite NCs,[10, 16] such as hot injection, ligand-assisted reprecipitation (LARP), and solvothermal techniques. These approaches provide facile control over the morphology and optical properties of the NCs through synthetic means. Additionally, the outstanding colloidal dispersibility of metal halide perovskite NCs enhances their potential for optoelectronic applications.

1.2.2 Method of synthesizing Metal Halide Perovskite NCs

Hot Injection

The hot injection method, initially developed over twenty years ago for synthesizing cadmium sulfide NCs,[60] has seen significant advancement in recent years, particularly in the synthesis of metal halide perovskite $CsPbX_3$ (X = Cl, Br, and I) NCs. First introduced by Protesescu et al. in 2015, this method relies on the rapid injection and mixing of different precursors in the presence of oleylamine (OAm), oleic acid (OA), or other ligands, and octadecene (ODE) under specific conditions, resulting in an ionic metathesis reaction followed by the formation of NCs, as illustrated in the diagram (Figure 1.8 a).[30] In this process, ODE serves as a high-boiling-point inert solvent, OAm functions as the primary capping ligand, and OA participates in the ionic metathesis reaction, although it can also adsorb to the NCs surface.[61]

In recent years, the hot injection method has matured and can now be employed for the synthesis of a wide range of metal halide perovskite NCs, including but not limited to $MAPbX_3$, $FAPbX_3$, etc.[62, 63] This method enables the control of NCs morphology, size, and optical properties by adjusting synthesis conditions such as (i) the ratio of ligand to precursor, (ii) the reaction temperature, (iii) reaction time, and (iv) precursor

concentration.

The study of the synthesis mechanism of the hot injection method has also been ongoing. For instance, Lignos et al. conducted a study on the growth kinetics of $CsPbX_3$ NCs using a liquid microfluidic platform.[64] Their findings, based on in-situ absorption and PL studies of $CsPbX_3$ NCs, revealed that the entire nucleation and growth occur within the first 1-5 seconds of the reaction, highlighting the remarkably fast reaction kinetics of these NCs. As a result, due to the rapid and challenging-to-separate nucleation and growth steps, the scientific community still lacks a comprehensive understanding of the nucleation and growth processes of metal halide perovskite NCs.

While the hot injection method has found extensive application, its intricate nature and requirement for high temperatures and inert atmospheres pose limitations on cost-effectiveness for large-scale production. Therefore, researchers still continue to explore alternative synthetic methods for the production of metal halide perovskite NCs.

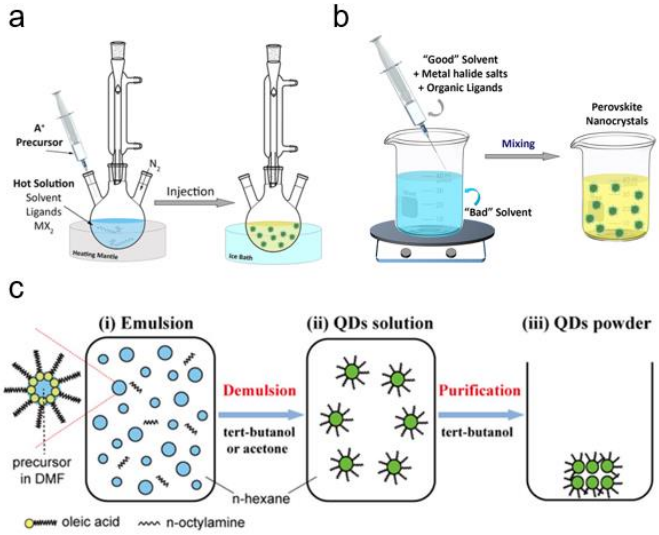

Figure 1.8 Sketch of different methods used for the synthesis of metal halide perovskite NCs.[16] (a) Hot Injection method. (b) LARP method. (c) Emulsion method, include (i) formation of the emulsion, (ii) demulsion by adding a demulsifier with the concomitant formation of perovskite NCs, and (iii) purification of the NCs.

Ligand-Assisted Reprecipitation (LARP) Method

The Ligand-Assisted Reprecipitation (LARP) method involves dissolving the

desired ions in a solvent containing ligands to achieve equilibrium concentration. The solution is then taken to a non-equilibrium supersaturated state, leading to the precipitation of NCs. Methods to induce supersaturation include adding a co-solvent with low ion solubility, altering temperature (typically cooling the solution), or evaporating the solvent. Under these conditions, spontaneous precipitation and crystallization reactions occur until the system returns to equilibrium.[16] In the synthesis of metal halide perovskite NCs using the LARP method, the precursor dissolved in a good solvent is dripped into a poor solvent while rapidly mixing, with the presence of ligands. The mixture of the two solvents creates an instantaneous supersaturation, triggering nucleation and growth of metal halide perovskite NCs (Figure 1.8b).[16] Commonly used good solvents in this method include DMF or DMSO, while poor solvents can be n-hexane or toluene. Unlike the hot injection method, the LARP synthesis method is straightforward and can even be conducted in ambient air, allowing for easy scalability, even to kilogram quantities.

The LARP synthesis method for metal halide perovskite NCs was first reported in 2012. Papavassiliou et al. dissolved metal halide perovskite precursors, such as $MAPbX_3$, in DMF or acetonitrile to form a salt solution.[65] By dripping the corresponding solution into toluene (or a toluene and PMMA mixture), they observed the formation of luminescent NCs, exhibiting significantly higher PL intensity compared to bulk $MAPbX_3$, with sizes ranging from 30-160 nm. This study undoubtedly marked the initiation of research into LARP synthesis for metal halide perovskite NCs. Subsequently, over the course of several years, LARP has been developed for synthesizing various metal halide perovskite ABX_3 NCs.

Despite its advantages, the LARP method has notable drawbacks. Firstly, metal halide perovskite NCs are highly sensitive to polar solvents, commonly used in LARP synthesis. For example, DMF can easily degrade or dissolve $CsPbX_3$ NCs, particularly $CsPbI_3$. Interactions between precursors and polar solvents play a crucial role in the formation of defective perovskite NCs. Additionally, typical polar solvents like DMF and DMSO used in this method have high boiling points and are toxic, making them

unsuitable for large-scale commercial production.

Emulsion Method

The emulsion method relies on the use of immiscible liquids. Precursor salts are dissolved in two different solvents with ligands, forming an emulsion. Subsequently, when a demulsifier (compatible with the two solvents) is added, the reaction takes place. The precursor solution then goes into a supersaturated state, leading to nucleation and growth of metal halide perovskite NCs (Figure 1.8c).[66, 67] In this method, ligands in a polar-nonpolar system can self-assemble into micelles, serving as nanoreactors where precursors can react to form NCs.

In 2015, Huang et al. synthesized $MAPbBr_3$ NCs using the emulsion method.[67] They first prepared a DMF solution of MABr and PbBr2, which was then emulsified with OA, octylamine, and n-hexane. The addition of tert-butanol or acetone, acting as a demulsifier, initiated the crystallization process, resulting in the formation of NCs.

Solvothermal Method

The solvothermal method is one of the most commonly used techniques for synthesizing nanomaterials under high pressure and suitable temperatures. In this approach, the precursor solution is added to a polytetrafluoroethylene-lined stainless-steel autoclave. The sealed vessel is then placed in an oven and heated to a specific temperature for the reaction, ultimately yielding NCs.[68] Compared to hot injection and LARP, the reaction in solvothermal synthesis is relatively slow. However, this method offers advantages such as high crystallinity, good uniformity, controllable size and shape, simplicity in synthesis, and scalability.

In 2017, Chen et al. pioneered the solvothermal synthesis of high-quality $CsPbX_3$ nanocubes and nanowires, achieving a PLQY exceeding 80%.[69] The morphology displayed excellent uniformity. They observed that the solubility of precursors significantly influences the NCs morphology. Completely dissolved precursor solutions during the reaction led to the formation of numerous small nuclei, ultimately growing into nanowires. On the other hand, undissolved precursors resulted in larger nuclei and the

growth of nanocubes. Subsequently, Zhai et al. successfully synthesized $CsPbBr_3$ nanoplatelets using the solvothermal method.[70] They discovered that increasing the Cs^+ content in the precursor led to the production of presynthesized Cs_4PbBr_6 NCs. Therefore, the condition as well as the ratio of the precursors in the solvothermal method also has a very drastic effect on the properties of the synthesized NCs.

Ion Exchange Method

Given the distinctive ion crystal characteristics and the low formation energy associated with metal halide perovskites, ion exchange reactions present a convenient and versatile methodology for synthesizing metal halide perovskite NCs.

The most straightforward ion exchange is anion exchange reactions.[71] For example, metal halide perovskite NCs emitting different colors can be easily synthesized by reacting $CsPbX_3$ with various halogen precursors in the liquid phase. In 2015, Kovalenko et al. conducted experiments on anion exchange using PbX_2 or oleylammonium halide as halide precursors with $CsPbX_3$ NCs in 1-Octadecene (ODE) as the solvent.[71] This experimental approach yielded highly luminescent metal halide perovskite NCs covering the entire visible spectrum (Figure 1.9a, b). Typically, Cl-to-Br and Br-to-Cl exchanges can be efficiently achieved under mild conditions. Conversely, Br-to-I and I-to-Br anion exchanges generally result in the formation of homogeneous mixed-halide perovskite NCs solid solutions. It is noteworthy that, owing to the substantial difference in ion radius between Cl- and I-, Cl/I mixed-halide perovskite NCs are generally deemed unstable. Consequently, in the reaction system involving $CsPbI_3 + Cl^-$ and $CsPbCl_3 + I^-$, stable mixed-halide perovskite NCs cannot be obtained.

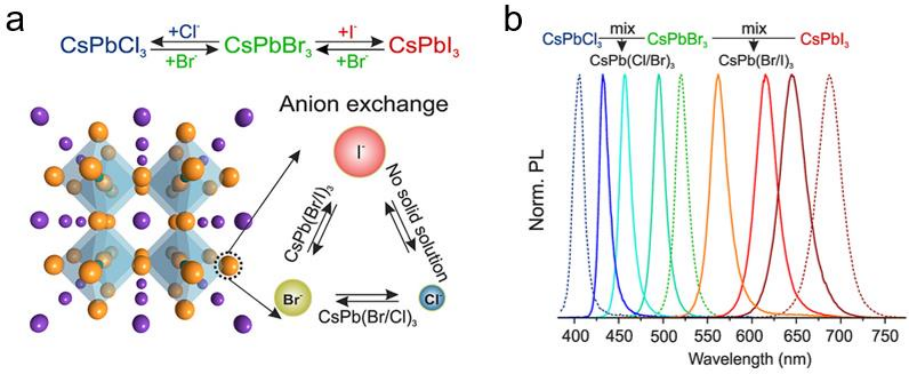

Figure 1.9 (a) Schematic of the anion-exchange within the cubic perovskite crystal structure of $CsPbX_3$ (Ionic radii: Cs^+, 1.88 Å; Pb^{2+}, 1.16 Å; Cl^-, 1.81 Å; Br^-, 1.96 Å; and I^-, 2.2 Å).[71] (b) PL of $CsPbX_3$ NCs resulting from inter- NCs anion exchange reactions.[71]

Cation exchange reactions in metal halide perovskite NCs typically exhibit slower kinetics compared to anion exchange, often necessitating longer reaction times or higher temperture. The ABX_3 structure encompasses two cationic sites, A and B-site. Consequently, cationic exchange reactions are categorized into A-site cation exchange and B-site cation exchange.

In 2017, Chen et al. reported A-site cation exchange. They replaced FA with MA cations to synthesize $FAPbX_3$ from the initial $MAPbX_3$.[72] Specifically, FA(ac) precursors were introduced into the colloidal solution of $MAPbBr_3$ NCs. Following a gradual cation exchange reaction lasting 150 minutes, the $FAPbBr_3$ NCs underwent a complete phase transformation. In instances where the exchange is incomplete or multiple A-site cations are used, it can result in the formation of double or triple cation metal halide perovskite NCs (Figure 1.10a, b).[73] B-site cation exchange is commonly employed to achieve mixed B-site metal halide perovskite NCs. For instance, the introduction of cations such as Sn^{2+}, Zn^{2+}, and Cd^{2+} into a $CsPbBr_3$ NCs solution can induce lattice contraction, resulting in a blue shift in PL,[74] while maintaining the original NCs morphology. Similarly, introducing Mn^{4+} into a $CsPbCl_3$ NCs solution can bring Mn^{2+}-doped $CsPbCl_3$ NCs exhibiting bright red-light emission (Figure 1.10c, d, and e).[75]

Furthermore, in 2018, Manna et al. reported the conversion of non-perovskite CsX NCs into $CsPbX_3$ NCs through cation exchange.[76] When CsX NCs react with Pb-oleate, it appears that one Pb^{2+} can replace two Cs ions in CsX, leading to the synthesis of $CsPbX_3$ NCs. CsX is easily synthesizable, and its size is readily adjustable. Therefore, size-tunable $CsPbX_3$ perovskite NCs can be easily obtained through cation exchange reactions with CsX. In summary, owing to the material characteristics of metal halide perovskites, ion exchange methods provide convenient pathways for synthesizing metal halide perovskite NCs.

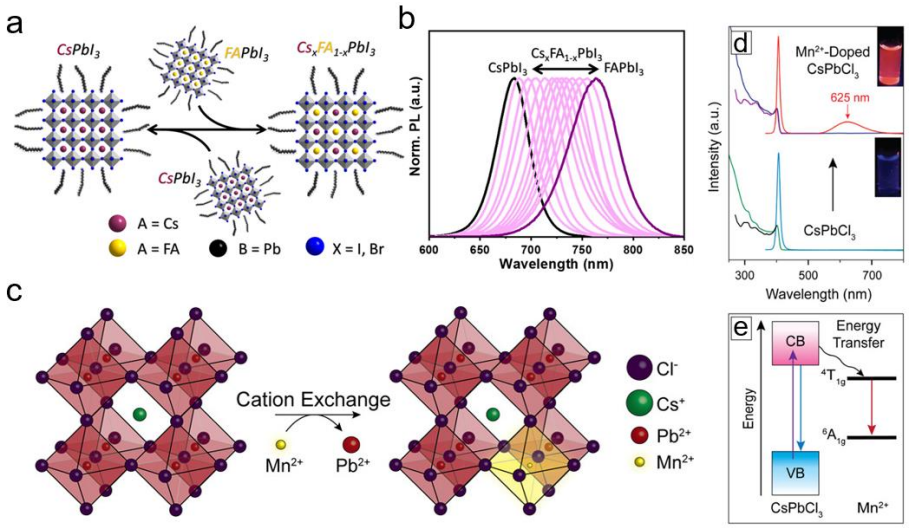

Figure 1.10 (a) Schematic illustration of the formation of double-cation perovskite ($Cs_xFA_{1-x}PbI_3$) NCs through reversible cation exchange by mixing $CsPbI_3$ and $FAPbI_3$ perovskite NCs. (b) Normalized PL spectra of $CsPbI_3$, $FAPbI_3$ and $Cs_xFA_{1-x}PbI_3$ NCs obtained by cation exchange. The emission wavelength of the mixed-cation NCs is tunable between those of the individual pure A-cation compositions.[73] (c) Schematic of the Mn^{2+} Cation Exchange within the Cubic Perovskite Crystal Structure, from $CsPbCl_3$ NCs to Mn^{2+}-Doped $CsPbCl_3$ NCs. (d) Absorption, PL excitation (monitored at 415 nm), and PL emission before (green, black, and aqua, respectively) and after (excitation monitored at 625 nm) (blue, purple, and red, respectively) Mn^{2+} doping. Photographs of starting $CsPbCl_3$ and Mn^{2+}-doped $CsPbCl_3$ NCs show the emergence of red emission upon doping (insets). (e) Energy level diagram of the NCs following Mn^{2+} doping.[75]

Other Methods

In addition to the previously mentioned synthesis methods, the soft ionic crystal structure of halide perovskite NCs renders them highly adaptable to various convenient synthetic approaches. These include microwave-assisted synthesis, ultrasound-assisted reactions, and chemical vapor deposition (CVD), among others.[16] In summary, the diverse synthesis methods not only enhance the ease of research and applications of perovskite materials but also provide convenience and a myriad of possibilities.

1.2.3 Morphology Control of Metal Halide Perovskite NCs

The manipulation of NCs shape and size is pivotal in influencing their optical and

physical characteristics. For example, spherical NCs exhibit isotropic PL, whereas nanorods or nanowires display polarized emission. Diverse synthetic approaches have been investigated to govern the morphology of ABX_3 metal halide perovskite NCs, enabling the easy acquisition of various shapes like nanocubes, nanospheres, nanorods, nanowires, nanoplates, and beyond. As mentioned earlier, surface-active agents such as alkane amines and acids are commonly employed in different synthesis methods of metal halide perovskite NCs. Alkane amines and acids bond with different atoms, anions, and cations, respectively, to maintain charge balance. In other words, the orientation and shapes of NCs can be influenced by altering the activity of surface-active agents (e.g., temperature) or by changing the types, ratios, or amounts of amines and acids.

In 2016, Pan et al. investigated the morphology control of $CsPbBr_3$ NCs synthesized via the hot injection method.[77] They conducted extensive experiments studying the types of acids and amines, as well as the injection temperature. The results indicated that at low temperatures, the use of OA and OAm led to anisotropic growth, resulting in nanosheets. The thickness of these nanosheets seemed to have little correlation with the chain length of amines and acids. However, at high temperatures, the use of long-chain amines and acids resulted in smaller nanocubes, while short-chain amines led to nanosheet formation. In contrast, Imran et al. found that using OAm and octylamine without the acids in the hot injection method easily produced $CsPbBr_3$ nanowires, exhibiting bright green emission.[78]

The LARP method also provides effective control over the morphology of metal halide perovskite NCs. Studies have found that using combinations of amines and acids with different chain lengths during LARP synthesis can produce $CsPbX_3$ NCs with various morphologies. For example, OAm and hexanoic acid can shape NCs into spherical quantum dots, dodecylamine and OA can transform NCs into nanocubes, while dodecylamine and acetic acid result in nanocubes, and OAm and OA produce nanosheets (Figure 1.11a).

In addition to the direct synthesis of NCs with different morphologies,

morphological transformations are also observed after the synthesis of NCs. For instance, Sun et al. discovered that $CsPbI_3$ nanocubes could transform into nanowires when treated with polar solvents. This transformation was attributed to lattice distortion induced by polar solvents, followed by dipole moment-triggered self-assembly into single-crystal nanowires. Dang et al. observed the evolution of $CsPbBr_3$ nanoplates into nanoribbons and nanosheets over time in both solution and thin films. Interestingly, post-synthesis transformations or self-assemblies can result in NCs with a rich variety of polyhedral morphologies, as extensively studied by Pradhan et al (Figure 1.11b, c).[79-81]

In addition to the methods mentioned above, other direct or indirect synthesis methods of metal halide perovskite NCs can also achieve size and morphology control. For example, Sun et al. synthesized $MAPbBr_3$ nanospheres, nanocubes, and nanoplates using the emulsion synthesis method.[82] In summary, such straightforward morphology control of metal halide perovskite NCs provides a myriad of possibilities for advancing research on perovskite materials and exploring new intriguing optical properties.

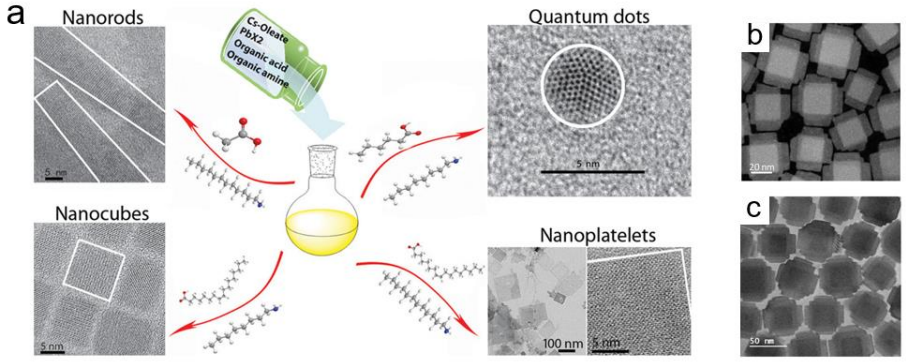

Figure 1.11 (a) Schematic illustrating the formation process for different $CsPbX_3$ (X = Cl, Br, I) NCs mediated by organic acid and amine ligands at room temperature. Hexanoic acid and octylamine for spherical quantum dots; oleic acid and dodecylamine for nanocubes; acetate acid and dodecylamine for nanorods; oleic acid and octylamine for few-unit-cell-thick nanoplatelets.[82] (b) TEM image of ~50 nm $CsPbBr_3$ armed hexapod nanostructures. (c) TEM image of ~60 nm step-armed $CsPbBr_3$ nanostructures.[81]

1.2.4 Enhancement of Optical Performance in Metal Halide Perovskite NCs

Compared to other semiconductor nanomaterials, despite the excellent defect

tolerance characteristics of metal halide perovskite NCs, which enable outstanding optical performance even without any surface modification, they have not yet reached their limits in terms of luminescent efficiency. This is especially true for lead-based perovskite NCs rich in chlorine and tin-based $ASnX_3$ perovskite NCs. In recent years, various approaches to enhance the optical performance of metal halide perovskite NCs have been actively reported. These approaches include, but are not limited to, precursor engineering, surface ligand engineering, doping, and alloying.

Precursor Engineering

The synthesis process of metal halide perovskite NCs typically involves various precursors, and the optical performance, morphology, and trap density are largely influenced by the types and properties of these precursors. Recent research has increasingly highlighted the significance of subtle variations in the composition or types of precursors, which can result in changes in the performance of perovskite materials.[83]

In the case of $CsPbX_3$, the synthesis commonly involves Cs precursors and PbX_2 precursors or reactions with individual Pb and X precursors. Cs precursors are often limited in variety, with Cs_2CO_3 or cesium acetate commonly used. In 2017, Liu et al. achieved a near 100% PLQY for $CsPbI_3$ NCs by combining PbI_2 and Cs_2CO_3.[84] They improved the precursor preparation by using trioctylphosphine-PbI_2, prepared using a special method, resulting in significantly enhanced stability and luminescent efficiency of $CsPbI_3$ NCs. To precisely control the amounts of Pb and X at the Pb and X positions, scholars have developed methods using PbO, lead acetate, and alkylammonium halide salts,[85] benzoyl halides,[86] or other halides as Pb and X sources.[87, 88] Dutta et al. used a combination of alkylammonium halide salts, PbO, and Cs_2CO_3 to obtain $CsPbCl_3$, $CsPbBr_3$, and $CsPbI_3$ NCs with PLQYs close to 100%. They also observed that even a 5% change in the ratio of Cs to Pb precursors led to a drastic decrease in PLQY, particularly noticeable during $CsPbCl_3$ synthesis, emphasizing the crucial importance of accurately controlling precursor ratios.[85]

It is noteworthy that the impact of raw materials ratios on the optical performance

of $CsSnX_3$ NCs appears to be more pronounced. Liu et al. found that only under conditions of excess Sn, excess halogens, and Cs deficiency could high PLQY NCs be obtained during $CsSnX_3$ synthesis.[89] Theoretical calculations reveal that tin vacancies (V_{Sn}) have a low formation energy and introduce deep trap states in the bandgap, leading to a significant reduction in PLQY. Therefore, a tin-rich environment can effectively reduce V_{Sn}. Thus, through precursor engineering, the rational control of precursor types and ratios becomes crucial for suppressing defects in metal halide perovskite NCs and improving their optical performance.

Ligand Engineering

Due to the larger surface area of nanomaterials, their optical and other physical properties are highly susceptible to the significant influence of surface ligands. Therefore, surface ligands play a crucial role in shaping the optical properties and potential applications of semiconductor NCs. The most commonly used surface ligands for metal halide perovskite NCs are alkyl-chain-containing ligands such as OA and OAm. These ligands are vital for maintaining the optical performance and stabilizing the morphology of the NCs. Therefore, appropriate ligand selection can passivate surface defects in NCs, resulting in highly luminescent metal halide perovskite nanoparticles and significantly enhanced structural stability. Furthermore, when applying these NCs in optoelectronic devices such as solar cells or LEDs, the selection of ligands must also consider their impact on the charge carrier transport performance. In this context, short alkyl chain ligands with good conductivity and inorganic ligands are gradually being applied to metal halide perovskite NCs through surface ligand engineering. According to the Covalent Bond Classification method, all these ligands can be structurally classified into L-type, X-type, or Z-type.[10] L-type ligands are Lewis bases, providing two electrons when coordinated with NCs, such as OAm and tri-n-octylphosphine. Z-type ligands are Lewis acids, providing an empty orbital, including carboxylate, phosphate, sulfonate, or thiol/thiolate. X-type ligands provide one electron, such as K^+ , Na^+ cations (Figure 1.12a).

As discussed in the previous sections, changes in ligands during the synthesis

process can significantly impact the morphology and optical performance of NCs. In addition to using ligands during synthesis, post-treatment of ligand is commonly employed to purposefully improve the optical performance of NCs. For instance, in 2018, Pan et al. utilized the using ligand 2,2'-iminodiacetic acid (IDA) to passivate the surface defects of $CsPbI_3$ NCs through a post-treatment method.[90] This not only enhanced stability but also increased the PLQY from 80% to 95%, resulting in a red-emitting $CsPbI_3$ NCs LED with an EQE of 5.02%. Krieg et al. significantly improved the chemical stability of $CsPbX_3$ NCs by employing zwitterionic ligand.[91] Similarly, zwitterionic ligands are often applied to enhance NCs luminescence and improve device performance.

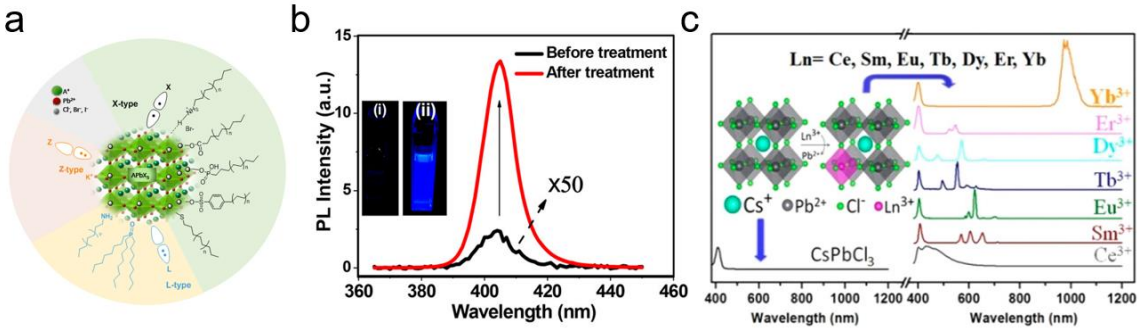

Figure 1.12 (a) Binding ligands (X, L, and Z-Type, according to the Covalent Bond Classification) Used as capping agents of ABX_3 perovskite NCs.[10] (b) PL spectra of $CsPbCl_3$ showing dramatic enhancement of PL upon $CdCl_2$ treatment.[92] (c) PL spectra and crystal structure of lanthanide ions (Ln^{3+}) doped $CsPbCl_3$ NCs.[93]

Doping and alloying structure

Doping and alloying are commonly used strategies to enhance the optical properties and improve the stability of semiconductor nanomaterials. In 2019, Yao et al. doped $CsPbI_3$ NCs with alkaline earth metal Sr^{2+}, resulting in both enhanced stability and improved luminescent intensity of the NCs.[94] The introduction of Sr^{2+} significantly increased the formation energy of $CsPbI_3$ NCs, reducing structural distortions and leading to a more stable cubic perovskite structure. When 60% of Sr^{2+} were introduced during the synthesis of $CsPbI_3$, the PLQY of the NCs increased from 78% to 95%. Subsequently, these NCs were employed in LEDs, yielding bright and stable red perovskite LEDs.

Apart from alkaline earth metals, numerous results of transition metal ion doping in metal halide perovskite NCs have been reported. Yong et al. utilized Ni^{2+} during the synthesis of $CsPbCl_3$ NCs, eliminating structural defects in $CsPbCl_3$, improving short-range lattice order, and increasing the PLQY from 2.4% to 96.5% after doping.[95] Additionally, doping $CsPb(Cl/Br)_3$ with Ni^{2+} raised the PLQY to above 90%. Cation exchange has also been used for metal cation doping in metal halide perovskite NCs. For instance, treating $CsPbCl_3$ NCs with $CdCl_2$ at room temperature increased the PLQY from 3% to nearly 100% (Figure 1.12b),[92] with ICP and EDX spectra confirming the successful incorporation of Cd^{2+} into the $CsPbCl_3$ lattice. Transition metal doping not only enhances the optical properties of materials but can also introduce new luminescent centers. For example, doping $CsPbCl_3$ NCs with Mn^{4+} introduce a new emission peak around 625 nm, distinct from the intrinsic emission of $CsPbCl_3$ near 410 nm. Co-doping $CsPbCl_3$ with Mn^{4+} and post-transition metal Bi^{3+} may enable white light emission, as Bi^{3+} introduces an additional blue emission peak at 463 nm.[96]

Rare earth cations are a crucial class of semiconductor dopants. Doping of rare earth cation in metal halide perovskite NCs not only introduces bright and rich emissions due to the energy levels of rare earth ions but also significantly enhances the PLQY. Pan et al. conducted a study on $CsPbCl_3$ NCs doped with various lanthanide metal cations, including Ce^{3+}, Sm^{3+}, Eu^{3+}, Tb^{3+}, Dy^{3+}, Er^{3+}, and Yb^{3+}(Figure 1.12c).[93] They observed a substantial overall increase in the PLQY of $CsPbCl_3$ NCs doped with different lanthanide ions, primarily attributed to the intrinsic emissions of rare earth ions. Additionally, doping $CsPbCl_3$ NCs with different lanthanide ions allowed for tunable emissions from visible to near-infrared ranges, with a maximum emission wavelength reaching around 1000 nm with Yb^{3+} doping. By utilizing stable red light-emitting Eu^{3+}-doped $CsPbCl_3$ NCs and blue-green light-emitting Ce^{3+}-doped $CsPbCl_3$ NCs, they successfully fabricated bright white LEDs, providing new possibilities for the application of metal halide perovskite nanomaterials in lighting and display technologies. It is noteworthy that Yb^{3+} doping can achieve the fascinating optical phenomenon of Quantum Cutting,[97] leading to a PLQY of

Yb^{3+}-doped $CsPbCl_3$ NCs far exceeding 100%, even reaching 200%. This is due to the transfer of energy from Yb^{3+} to two photons emitted from $^2F_{5/2} \rightarrow {}^2F_{7/2}$ far from the $CsPbCl_3$ absorption edge, resulting in a PLQY exceeding 100%. In summary, cation doping in metal halide perovskites holds great promise for eliminating defects, enhancing luminescence and stability, and enabling various optoelectronic applications of these materials.

1.3 Lead-Free Metal Halide Perovskite NCs

1.3.1 Background of Lead-Free Metal Halide Perovskites

In recent years, the research on lead-based halide perovskites has witnessed rapid development due to their outstanding properties, including high PLQY, tunable emission wavelengths, and straightforward solution preparation. Despite exhibiting numerous excellent characteristics, the presence of the toxic element lead hinders further commercial development of lead-based metal halide perovskite materials. Studies have revealed that degradation products of lead halide perovskites include water-soluble lead salts that can persist in the natural environment. Extensive medical research has reported the severe toxicity of lead, causing disruptions to the nervous, cardiovascular, and hematopoietic systems even with low levels of lead exposure.[98] The U.S. Centers for Disease Control and Prevention (CDC) recommends a safe blood lead level of <10 μg/dL. The European Union has issued directives restricting the use of certain lead-containing hazardous substances in electrical and electronic equipment, emphasizing lead-free alternatives. Therefore, the development of environmentally friendly lead-free metal halide perovskite materials with comparable optical and optoelectronic performance has become imperative.

With the collective efforts of numerous researchers, an increasing number of lead-free metal halide perovskite products have been discovered.[98] Figure 1.13a presents possible lead-free elements in perovskite or perovskite-derived structures. The standard ABX_3 perovskite structure has been introduced in previous sections. When the Pb^{2+} at the

B site is replaced by similar other B^{2+} ions, it remains a standard $AB^{2+}X_3$ perovskite. However, when Pb^{2+} is simultaneously replaced by B^{+} and B^{3+}, it forms a halide double perovskite structure of $A_2B^{1+}B^{3+}X_6$. When Pb^{2+} is replaced only by B^{3+}, it results in a perovskite derivative structure of $A_3B^{3+}{}_2X_9$, where one in three octahedral B^{3+} sites is vacant to maintain charge neutrality. Finally, when Pb^{2+} is replaced by B^{4+}, it leads to a perovskite derivative structure of $A_2B^{4+}X_6$, equivalent to half of the B sites being occupied by vacancies in the $A_2B_2X_6$ perovskite, thus termed a vacancy-ordered perovskite (Figure 1.13b).[99]

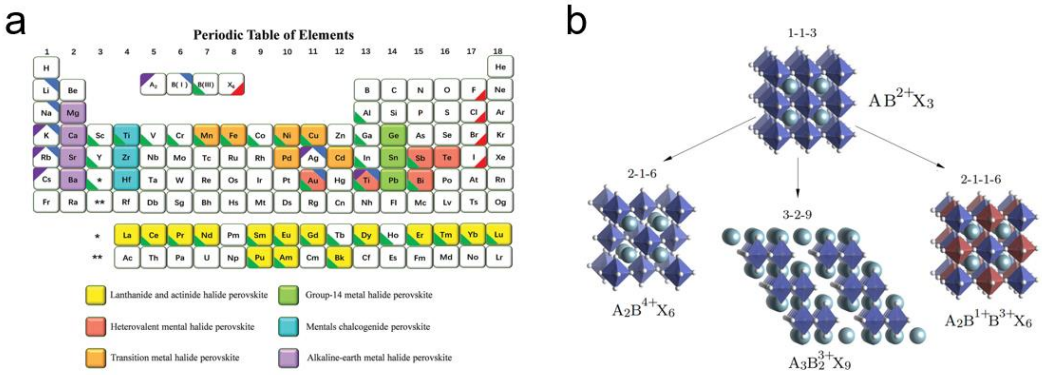

Figure 1.13 (a) Lead replacement candidates in halide perovskites in the periodic table of elements.[98] (b) Schematic relation between the crystal structures of lead halide perovskites and lead-free halide perovskite derivatives.[99]

1.3.2 Classification of Lead-Free Perovskites

$AB^{2+}X_3$ Type Perovskites

Elements Sn^{2+} and Ge^{2+}, belonging to the same main-group as Pb^{2+}, are considered promising substitutes for Pb^{2+}, given their similar radii and coordination types to Pb^{2+}. This similarity suggests the potential for these elements to exhibit equally excellent optoelectronic performance. Consequently, $ASnX_3$ and $AGeX_3$ are among the few reported ABX_3-type lead-free metal halide perovskites. $ASnX_3$ and $AGeX_3$ have demonstrated considerable potential in various optoelectronic applications. Particularly noteworthy is $ASnI_3$, which has shown outstanding performance not only in solar cells but also in LED displays and lighting applications.[100, 101]

$ASnX_3$ shares a remarkably similar structure and phase transition behavior with $APbX_3$.[102] For instance, $CsSnI_3$, like $CsPbI_3$, exhibits two distinct crystal phases at room temperature—the black phase with excellent optoelectronic properties and the yellow phase with inferior performance. These two phases can undergo a phase transition between cubic (α-$CsSnI_3$, Fm-3m) and tetragonal (β-$CsSnI_3$, P4/mbm) structures, which is temperature-dependent, similar to Pb-based perovskites.

The crystal structure of $AGeX_3$ perovskite has also been extensively studied. Unlike $ASnX_3$, its lattice parameters are smaller in the cubic phase. These structural differences result in somewhat distinct optical behaviors among the three ABX_3-type perovskites. For instance, Roknuzzaman et al. using the generalized gradient approximation (GGA) of the Perdew-Berke-Ernzerhof (PBE) approach showed that, under the same halogen conditions, $CsSnX_3$ and $CsGeX_3$ exhibit similar band gaps, both smaller than $CsPbX_3$.[103] Additionally, all three are direct bandgap semiconductors, suggesting the potential for superior optical performance.

$A_2B^+B^{3+}X_6$ Type Halide Double Perovskites

Halide double perovskites, with two different B-site cations, provide ample opportunities in chemical synthesis. Zhang et al. employed first-principles calculations to identify over a dozen halide double perovskites exhibiting intrinsic thermodynamic stability, suitable bandgaps, small carrier effective masses, and low exciton binding energies.[104] Compared to lead-based metal halide perovskites, halide double perovskites exhibit excellent stability towards heat, light, and moisture, ensuring vast development potential in the field of optoelectronics. Due to significant compositional differences, different halide double perovskites often show substantial variations in optoelectronic performance. For example, $Cs_2AgBiBr_6$, a reported halide double perovskite, displays an indirect bandgap, while $Cs_2AgInCl_6$ is found to be a direct bandgap semiconductor. Meng et al. conducted theoretical calculations and summarized possible gap types for various halide double perovskites.[105] Karunadasa et al. were the first to synthesize $Cs_2AgBiBr_6$, revealing a cubic structure at room temperature (RT) with a highly symmetric perovskite

structure.[106] The $[AgBr_6]^{5-}$ and $[BiBr_6]^{3-}$ octahedra alternate in a corner-sharing arrangement, constituting the cubic perovskite structure. Other Cs_2AgBiX_6 halide double perovskites with different halogen compositions share a similar structure.

In terms of optical performance, $Cs_2AgBiBr_6$ exhibits a large bandgap of approximately 1.95 eV, leading to strong non-radiative recombination due to its indirect bandgap, which is unfavorable for applications. To address this issue, metal cation doping has become an important strategy to enhance the optical performance of halide double perovskites. Yb^{3+} doping in $Cs_2AgBiBr_6$ has achieved a remarkable 95% PLQY.[107] Moreover, Cs_2AgBiX_6 halide double perovskites demonstrate excellent stability against moisture, light, and heat, with no decomposition observed even after 240 days of exposure to ambient conditions.[108] For halide double perovskites with indirect bandgaps, doping is also an effective strategy to improve their optical performance. For instance, Na^+ ion doping in $Cs_2AgInCl_6$ increased PLQY from 1.1% to 46.4%, and co-doping with Na^+ and Bi^{3+} ions further raised PLQY to 87.2%.[109]

Most halide double perovskites also exhibit interesting self-trapped exciton (STE) luminescence phenomena.[110] $Cs_2AgInCl_6$, for instance, shows a broad emission in the range of 400-800 nm due to STE emission. The STEs in $Cs_2AgInCl_6$ arise from the strong Jahn-Teller distortion of $[AgCl_6]^{5-}$ octahedra. Specifically, the Ag–Cl linkages experience a lengthening of 0.08 Å along the axial direction, while undergoing a compression of 0.2 Å within the equatorial plane. The entrapment of holes at Ag atoms, leading to a modification in the electronic configuration of Ag to 4d9, promotes a Jahn–Teller distortion. Jin et al. proposed the photophysical mechanism of self-trapped exciton (STE) emission in $Cs_2AgInCl_6$ halide double perovskite.[111] After the excitation of free excitons, they transition to the STE energy level, followed by radiative recombination. It is noteworthy that the broad emission from STE in $Cs_2AgInCl_6$ in the range of 400-800 nm positions it as a promising warm white light-emitting material. In conclusion, the unique optical properties and outstanding stability of halide double perovskite materials have made them a recent research hotspot.

$A_3B^{3+}{}_2X_9$ Type Perovskite Derivatives

Replacing B^{2+} with trivalent B^{3+} disrupts the charge balance of $AB^{2+}X3$ perovskites, leading to lattice reconstruction into a lower energy structure, $A_3B^{3+}{}_2X_9$. Commonly utilized B^{3+} cations in this context are typically Bi^{3+} and Sb^{3+}, primarily due to the similarity of their ns^2 electronic configuration to that of Pb^{2+}. This similarity is crucial for achieving high light absorption and an extended carrier lifetime.[112] $Cs_3Sb_2I_9$ is characterized by two distinct structures: the 0D dimer configuration (space group P63/mmc, no. 194,) and the 2D corrugated layers of polyanions configuration (P-3m1, no. 164).[113] The 0D dimer $Cs_3Sb_2I_9$ film can be synthesized directly through a solution process, specifically spin-coating. In contrast, the production of a high-quality 2D $Cs_3Sb_2I_9$ thin film necessitates annealing the 0D $Cs_3Sb_2I_9$ film in SbI_3 vapor. The resulting 2D $Cs_3Sb_2I_9$ film manifests a bandgap of 2.05 eV and exhibits heightened stability in ambient air, emerges as a promising material for a variety of optoelectronic applications.

If substitution of the A-site in $Cs_3Sb_2I_9$ leads to the formation of a novel 2D $A_3B^{3+}{}_2X_9$-type perovskite derivative, namely $(NH_4)_3Sb_2I_9$.[114] The crystal structure of $(NH_4)_3Sb_2I_9$ is characterized by a monoclinic space group P121/m1, featuring a 2D layered arrangement similar to $Cs_3Sb_2I_9$, wherein the Cs^+ ions are replaced by homovalent NH^{4+} ions. Notably, the $(NH_4)_3Sb_2I_9$ single crystal exhibits a low optical bandgap of 1.92 eV. Remarkably, the $(NH_4)_3Sb_2I_9$ single crystal demonstrates high carrier mobilities, with a hole mobility of 4.8 $cm^2\ V^{-1}s^{-1}$ and an electron mobility of 12.3 $cm^2\ V^{-1}\ s^{-1}$, comparable to widely studied lead-based perovskites. Additionally, organic cations can also substitute the A-site, as exemplified by MA, leading to the formation of $MA_3Sb_2X_9$. The study shows that Cl-incorporated $MA_3Sb_2Cl_xI_{9-x}$ (x = 0-9, 2D) exhibits enhanced absorption, higher carrier mobilities, and increased efficiency in solar cells compared to the 0D $MA_3Sb_2I_9$, further underscoring the potential of A-site substitution for tailoring perovskite properties in optoelectronic applications.[115] These outstanding physical properties position $A_3B^{3+}{}_2X_9$ as a promising candidate for optoelectronic applications.

$A_2B^{4+}X_6$ Type Perovskite Derivatives

Due to the lack of interconnectivity among the [BX_6] octahedra, the A_2BX_6 perovskite variants are regarded as perovskite derivative with a zero-dimension structure. Extensive investigations have been undertaken on various $A_2B^{4+}X_6$ compounds, including A_2SnI_6 (A = Cs, MA), Cs_2PdBr_6, and Cs_2TiBr_6, with a focus on their potential applications in photovoltaics.[112] Distinguishing themselves from the 3D ABX_3 (B = Pb, Sn, and Ge) halide perovskites, A_2BX_6 compounds feature isolated [BX_6] octahedra, resulting in significant distinctions in their optoelectronic properties. The valence band maxima (VBMs) in these A_2BX_6 compounds are constituted by nonbonding X p orbitals, deviating from the cation lone-pair s–X p antibonding states observed in ABX_3 (B = Pb, Sn, and Ge) halide perovskites. Remarkably, inherent n-type conductivity is observed in these A_2BX_6 compounds. Despite their overall similarities, variations exist in their optoelectronic characteristics.

In the case of Cs_2SnI_6, the bandgap is direct, whereas Cs_2PdBr_6 and Cs_2TiBr_6 exhibit indirect bandgaps.[112] Moreover, in Cs_2TiBr_6, the isolated conduction band demonstrates greater localization compared to Cs_2PdBr_6, attributed to the more localized orbital character of Ti 3d orbitals relative to Pd 4d orbitals.

Beyond optoelectronic properties, defect characteristics in A_2BX_6 compounds diverge from those observed in ABX_3 (B = Pb, Sn, and Ge) halide perovskites. Taking Cs_2SnI_6 as an example, the calculated charge-state transition levels of intrinsic defects, including the prevalent I vacancy and Sn interstitial, indicate deep levels within the bandgap due to the strong covalency in the $[SnI_6]^{4-}$ octahedra.[116] This contrasts with the defect tolerance observed in its 3D counterpart, $CsSnI_3$. Similar defect intolerance has also been reported for Cs_2TiBr_6.

1.4 Lead-Free $CsSnX_3$ Perovskite NCs

1.4.1 Research Progress on $CsSnX_3$ NCs

Cesium tin halide ($CsSnX_3$) perovskite NCs have gained recognition as a prominent example of lead-free halide perovskite systems, primarily due to their appealing photophysical properties. These properties encompass substantial absorption coefficients and direct band gaps that are adjustable within the range of 1.3 to 2.8 eV (Figure 1.14a).[117]

Although $CsSnX_3$ perovskite NCs have captured the attention of numerous researchers, the performance of lead-free $CsSnX_3$ NCs obtained thus far significantly lags behind that of lead-based perovskite $CsPbX_3$ NCs. As illustrated in Figure 1.14b,[85, 90, 95, 118, 119] the reported $CsSnX_3$ NCs exhibit a maximum PLQY still below 20%, while the PLQY of $CsPbX_3$ NCs with different halide compositions approaches 100%.

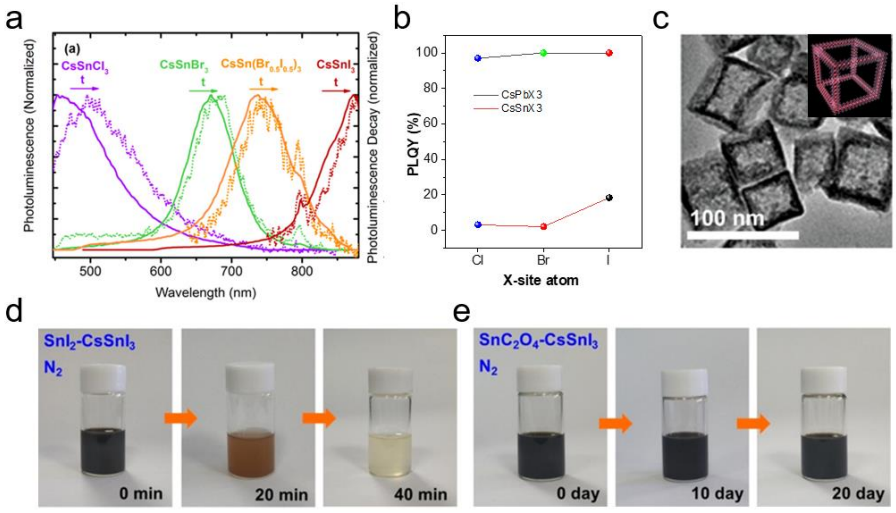

Figure 1.14 (a) PL of $CsSnX_3$ (X = Cl, Br, $Br_{0.5}I_{0.5}$, I) perovskite NCs.[117] (b) Highest reported PLQY for $CsSnX_3$ and $CsPbX_3$ NCs. (c) TEM images of $CsSnBr_3$ cubic nanocages. The inset is a schematic of nanocage structure.[118] (d) Photographs of SnI_2-$CsSnI_3$ NC dispersions stored in N_2. (e) Photographs of SnC_2O_4-$CsSnI_3$ NCs stored in N_2.[119]

Jellicoe et al. pioneered the synthesis of $CsSnX_3$ NCs through a comparable air-free hot-injection technique.[117] In their innovative approach, a weakly reducing solvent, tri-n-octylphosphine (TOP), effectively dissolved the SnX_2 powder. The resulting Sn-X-TOP

precursor solution was then injected into the Cs-oleate precursor solution containing OA and OAm ligands at a temperature of 170 °C. The reaction concluded within 1 minute, followed by prompt termination using an ice–water bath. Subsequently, colloidal $CsSnX_3$ NCs with various halide components were successfully prepared, exhibiting emission spectra ranging from the visible to the near-infrared region. The morphology of the as-prepared NCs, particularly in the case of $CsSnI_3$ NCs, is cubic with a size of less than 20 nm and uniform distribution. However, the stability of the as-prepared $CsSnX_3$ NCs is extremely poor; they degrade within several minutes under ambient conditions. The PLQY of the obtained $CsSnI_3$ NCs is less than 1%, suggesting the presence of a high density of structural defects contributing to nonradiative recombination. Further investigation reveals that the judicious mixing of long-chain OAm, short-chain octylamine, and octanoic acid can modulate the morphology of $CsSnI_3$, transforming it from nanocubes to nanoplates.

In addition to nanocubes, a broader range of $CsSnX_3$ NCs shapes can be obtained through precursor engineering. Wang et al., by judiciously controlling temperature and precursor selection using a hot-injection method, successfully synthesized $CsSnBr_3$ nanocages (Figure 1.14c).[118] Significantly, they were able to achieve this synthesis through precise control. Notably, $CsSnBr_3$ nanocages exhibited superior stability compared to nanocubes, providing a novel avenue for tuning the optical and physical properties of $CsSnX_3$ NCs. However, it is regrettable that the PLQY of these $CsSnBr_3$ nanocages is only around 2%, falling significantly short of the requirements for practical applications in optoelectronic devices.

$CsSnX_3$ NCs are notorious for their poor stability, primarily attributed to the air sensitivity of Sn^{2+}, which are prone to oxidation into Sn^{4+}. Consequently, enhancing the stability of $CsSnX_3$ perovskite materials has been a prominent focus in academic research. In a recent study, Kang et al. employed the antioxidant oxalate ligand to improve the stability of $CsSnX_3$ NCs (Figure 1.14d, e).[119] They selected stannous oxalate (SnC_2O_4), Cs_2CO_3, and NH_4I as precursors for Sn^{2+}, Cs^+, and I^-, respectively, and utilized a hot-

injection method to fabricate $CsSnI_3$ NCs. These NCs retained their original perovskite structure for nearly 15 days in a nitrogen environment without undergoing phase transitions, and they could endure for 12 hours in ambient air. The robust stability was attributed to the strong antioxidant capability of the SnC_2O_4 precursor, which likely inhibits in-situ oxidation processes during synthesis. Additionally, the oxalate ligands formed stable chelates through strong coordination with Sn^{2+}, preventing the decomposition of NCs. Unfortunately, the $CsSnX_3$ NCs obtained through this method exhibited an extremely low PLQY, indicating the presence of a high-density of defects leading to pronounced nonradiative recombination.

The synthesis of $CsSnX_3$ NCs has not witnessed a significant breakthrough until the noteworthy results reported by Liu et al. in 2020. In their work, they employed trimethylsilyl iodide (TMSI) as the iodine source and Tin 2-ethylhexanoate as the tin source, utilizing a hot-injection method.[120] By precisely controlling the ratio of raw materials, they achieved $CsSnI_3$ NCs with a remarkable PLQY of 18.4%. Subsequently, employing the same synthetic approach but substituting a portion of TMSI with trimethylsilyl bromide (TMSBr), they successfully synthesized $CsSnI_{2.5}Br_{0.5}$ and $CsSnI_{2.25}Br_{0.75}$ NCs. These NCs exhibited near-infrared emission at 925nm and 896 nm, respectively, with PLQY values of 7.7% and 7.1%. It is noteworthy that the introduction of Br^- led to a noticeable decrease in PLQYs. Nevertheless, their research provides hope for further exploration in the synthesis of $CsSnX_3$ NCs.

The application of $CsSnX_3$ perovskites in optoelectronic devices shows promise. However, in the current report on $CsSnX_3$ solar cells or LEDs, the focus has predominantly been on bulk or thin-film studies.[101] There is a paucity of research on the application of $CsSnX_3$ NCs. The primary reason lies in the difficulty of synthesizing $CsSnX_3$ NCs with low defect density and high luminescence efficiency. Therefore, there is an urgent need to develop synthetic approaches for high-quality $CsSnX_3$ NCs characterized by low defect density and high luminescence efficiency.

1.4.2 Challenges in $CsSnX_3$ Perovskite NCs Synthesis

Currently, synthesizing highly luminescent $CsSnX_3$ perovskite NCs remains a significant challenge. Specifically, challenges can be summarized in several key aspects: $CsSnX_3$ exhibits inherent instability in natural environments, and effective methods to enhance stability are currently lacking, leading to the generation of deep defect levels that capture charge carriers during degradation. There is still a lack of fundamental understanding of how to rationally suppress the formation of structural defects detrimental to radiative carrier recombination and narrow emission in $CsSnX_3$ NCs. Due to the extremely rapid nucleation and growth processes of $CsSnX_3$ NCs, there is a severe lack of understanding of their synthetic processes. With the deepening research on $CsSnX_3$ NCs, the aforementioned challenges are gradually being resolved.

Compared to Pb, Sn has a lower electronegativity, higher atomic energy level, and smaller s and p splitting energy. These factors result in a significant decrease in the ionization energy of Sn, indicating that Sn^{2+} loses electrons more easily than Pb^{2+}, leading to its oxidation to Sn^{4+}.[121] Lanzetta et al. conducted a study in 2021 on the degradation mechanism of $ASnX_3$ perovskites under environmental conditions.[122] They identified SnI_4 as the primary factor contributing to the degradation of $ASnX_3$ perovskites. SnI_4 is formed when $ASnX_3$ perovskites react with oxygen in the environment. Subsequently, SnI_4 evolves into I_2 in the air, causing erosive effects on the perovskite structure, leading to rapid oxidation and the formation of additional SnI_4, thereby accelerating the degradation of $ASnX_3$ perovskites.

Notably, the production of SnI_4 is not exclusively attributed to oxygen; certain intermediate materials and preparation processes may induce an undesirable transformation from Sn^{2+} to Sn^{4+}. For instance, research indicates that DMSO can undergo irreversible redox reactions with Sn^{2+}, generating Sn^{4+}.[123] Furthermore, the pH of the solvent significantly influences the oxidation process of Sn^{2+}, as Sn^{2+} is thermodynamically more stable in acidic environments compared to alkaline ones.[124]

Importantly, the transformation from Sn^{2+} to Sn^{4+} introduces numerous Sn vacancies (V_{Sn}) defects in the perovskite crystal structure. V_{Sn} is the most common and has the lowest formation energy among defects in $ASnX_3$ perovskites. V_{Sn} can significantly reduce the PLQY through non-radiative recombination after capturing photogenerated holes in $CsSnI_3$ NCs. Therefore, controlling the formation of SnI_4 is crucial for enhancing the stability and optical performance of $ASnX_3$ perovskite materials.

The formation of V_{Sn} is also influenced by the synthesis conditions. Liu et al. conducted in-depth theoretical calculations to investigate the impact of various point defects on the optoelectronic properties of $CsSnI_3$ NCs.[120] The computed formation energies for three vacancies (V_{Cs}, V_{Sn}, and V_I), two antisites (Cs_{Sn} and Sn_I), and one interstitial (I_i) indicate that V_{Sn} exhibits the lowest formation energy, establishing it as the dominant defect in conditions of Sn scarcity. An evident trend is observed wherein an increase in the chemical potential of Sn elevates the formation energies of V_{Sn}, V_{Cs}, Cs_{Sn}, and I_i while diminishing the formation energies of V_I and Sn_I. When compared to the pristine $CsSnI_3$, the presence of V_{Sn} induces a more pronounced alteration in the bandgap, suggesting that the distortion caused by V_{Sn} modifies the crystal geometry, resulting in the broadening of the $CsSnI_3$ emission. These computational results suggest that inhibiting the formation of V_{Sn} can not only augment the PLQY but also yield a $CsSnI_3$ emission with a narrower band.

It is evident that the precise control of the types and ratios of precursors during the growth process has a significant impact on defect formation in $CsSnX_3$ NCs. Despite numerous studies investigating the nucleation and growth mechanisms of metal halide perovskites, a clear understanding has yet to be achieved. Moreover, the precursor solutions used in the synthesis of metal halide perovskites also present a complex chemical environment. For instance, research has revealed that precursor solutions behave as colloidal dispersions rather than true solutions, adding to the challenges of studying the nucleation and growth processes of metal halide perovskite NCs.[125] The field is still filled with unknowns, but as research progresses, I are gradually making

advancements in overcoming these challenges.

1.5 Thesis motivations and organization

$ASnX_3$ perovskites emerge as promising candidates for lead-free alternatives, showcasing remarkable potential in optoelectronic devices. Their appeal lies not only in low toxicity but also in possessing an ideal bandgap and high charge carrier mobility. Currently, solar cells certified with $ASnX_3$ have surpassed 10% efficiency, while LEDs fashioned from $ASnX_3$ exhibit high-brightness near-infrared electroluminescence. These achievements underscore the considerable promise of $ASnX_3$ perovskites in the realm of optoelectronic devices. However, the performance of these $ASnX_3$ perovskite devices is still far from commercialization. The primary hurdle is the difficulty in obtaining $ASnX_3$ perovskite materials with low defect density and high quality. Despite notable advancements, representative structures like $CsSnX_3$ NCs have yet to be synthesized with both low defect density and efficient luminescence. This limitation stems from an incomplete understanding of the reaction mechanisms and precursor chemistry involved in the synthesis process of $CsSnX_3$ NCs. Moreover, methods tailored for synthesizing $CsSnX_3$ NCs with optimal characteristics remain to be developed.

The primary objective of this thesis is to enhance researcher comprehension of the precursor chemistry integral to the synthesis process of $CsSnX_3$ NCs. Through a comprehensive exploration of the precursor chemistry involved in the synthesis of $CsSnX_3$ NCs, my aim is to devise innovative methods for their synthesis. The ultimate goal is to achieve $CsSnX_3$ NCs characterized by a uniform morphology and efficient luminescence.

In Chapter 2, I investigated the precursor chemistry involved in the hot-injection synthesis of $CsSnI_3$ NCs. Specifically, I observed that batch variations of $Sn(Oct)_2$ significantly influence the size and PLQY of the resulting $CsSnI_3$ NCs when preparing the TOP-Sn-I precursor through the mixing of $Sn(Oct)_2$ with TMSI and trioctylphosphine (TOP). My studies revealed that $Sn(Oct)_2$ impacts the reactivity of the TOP-Sn-I

precursor by forming intermediate products known as alkanoate iodides ($Sn_xI_y(Oct)_{2x-y}$) with TMSI. This process results in the synthesis of $CsSnI_3$ NCs with varying performance characteristics. Hence, meticulous precursor selection and control are crucial in the synthesis process of $CsSnI_3$ NCs to achieve high-quality outcomes. This research contributes to the development of more systematic synthetic approaches, with the aim of improving NCs size uniformity and optimizing optical properties.

In chapter 3, a novel method utilizing cation exchange for phase transition synthesis is introduced, demonstrating its efficacy in producing high-quality $CsSnX_3$ NCs with superior PLQY and adjustable size. Notably, $CsSnI_3$ NCs with an outstanding PLQY of 34.4% were achieved, surpassing the previous maximum value of 18.4%. This approach's-controlled reaction kinetics enable the synthesis of NCs with excellent size uniformity, crucial for optoelectronic applications.

In chapter 4, a deeper investigation into controlled ion exchange processes, introduce $Sn(Oct)_2$ during the synthesis of $CsSnI_3$ NCs, reveals a pathway to improve crystal quality. This effort led to a notable enhancement of the PLQY of $CsSnI_3$ NCs to 49.7%, alongside uniform size distribution. Detailed analysis, including in-situ PL and high-resolution transmission electron microscopy (HRTEM), X-ray photoelectron spectroscopy (XPS), elucidates the role of $Sn(Oct)_2$ in accelerating the reaction rate while minimizing uncoordinated Sn and I atoms, thereby maximizing PLQY. Furthermore, the versatility of controlled ion exchange methods is showcased through the synthesis of tin halide perovskite NCs with varied halide compositions via anion exchange.

In chapter 5, conclusions as well as outlook for further investigations on the topic of the thesis are presented.

Reference

(1) Akkerman, Q. A.; Rainò, G.; Kovalenko, M. V.; Manna, L. Genesis, challenges and opportunities for colloidal lead halide perovskite nanocrystals. *Nature Materials* **2018**, *17* (5), 394-405.

(2) Peña, M. A.; Fierro, J. Chemical structures and performance of perovskite oxides. *Chemical reviews* **2001**, *101* (7), 1981-2018.

(3) Akkerman, Q. A.; Manna, L. What Defines a Halide Perovskite? *ACS Energy Letters* **2020**, *5* (2), 604-610.

(4) Barman, A.; Kar-Narayan, S.; Mukherjee, D. Caloric effects in perovskite oxides. *Advanced Materials Interfaces* **2019**, *6* (15), 1900291.

(5) Lou, B.; Shakoor, N.; Adeel, M.; Zhang, P.; Huang, L.; Zhao, Y.; Zhao, W.; Jiang, Y.; Rui, Y. Catalytic oxidation of volatile organic compounds by non-noble metal catalyst: Current advancement and future prospectives. *Journal of Cleaner Production* **2022**, *363*, 132523.

(6) Weber, D. $CH_3NH_3PbX_3$, ein Pb(II)-System mit kubischer Perowskitstruktur / $CH_3NH_3PbX_3$, a Pb(II)-System with Cubic Perovskite Structure. *Zeitschrift für Naturforschung B* **1978**, *33* (12), 1443-1445.

(7) Kovalenko, M. V.; Protesescu, L.; Bodnarchuk, M. I. Properties and potential optoelectronic applications of lead halide perovskite nanocrystals. *Science* **2017**, *358* (6364), 745-750.

(8) Chen, R.; Liu, C.; Chen, Y.; Ye, C.; Chen, S.; Cheng, J.; Cao, S.; Wang, S.; Cui, A.; Hu, Z.; et al. Ferroelectric $CsGeI_3$ Single Crystals with a Perovskite Structure Grown from Aqueous Solution. *The Journal of Physical Chemistry C* **2023**, *127* (1), 635-641.

(9) Ming, W.; Shi, H.; Du, M.-H. Large dielectric constant, high acceptor density, and deep electron traps in perovskite solar cell material $CsGeI_3$. *Journal of Materials Chemistry A* **2016**, *4* (36), 13852-13858.

(10) Dey, A.; Ye, J.; De, A.; Debroye, E.; Ha, S. K.; Bladt, E.; Kshirsagar, A. S.; Wang, Z.; Yin, J.; Wang, Y.; et al. State of the Art and Prospects for Halide Perovskite

Nanocrystals. *ACS Nano* **2021**, *15* (7), 10775-10981.

(11) Schaak, R. E.; Mallouk, T. E. Perovskites by design: a toolbox of solid-state reactions. *Chemistry of Materials* **2002**, *14* (4), 1455-1471.

(12) Weber, D. Das Perowskitsystem CH_3NH_3 [$Pb,Sn_{1-n}X_3$] (X = Cl, Br, I) / The Perovskite System CH_3NH_3[$Pb_nSn_{1-n}X_3$] (X = C1, Br, I). *Zeitschrift für Naturforschung B* **1979**, *34* (7), 939-941.

(13) Weber, D. $CH_3NH_3SnBr_xI_{3-x}$ (x = 0-3), ein Sn(II)-System mit kubischer Perowskitstruktur / $CH_3NH_3SnBr_xI_{3-x}$(x = 0-3), a Sn(II)-System with Cubic Perovskite Structure. *Zeitschrift für Naturforschung B* **1978**, *33* (8), 862-865.

(14) Jin, S.; Tiefel, T. H.; McCormack, M.; Fastnacht, R.; Ramesh, R.; Chen, L. Thousandfold change in resistivity in magnetoresistive La-Ca-Mn-O films. *Science* **1994**, *264* (5157), 413-415.

(15) Manser, J. S.; Christians, J. A.; Kamat, P. V. Intriguing Optoelectronic Properties of Metal Halide Perovskites. *Chemical Reviews* **2016**, *116* (21), 12956-13008.

(16) Shamsi, J.; Urban, A. S.; Imran, M.; De Trizio, L.; Manna, L. Metal Halide Perovskite Nanocrystals: Synthesis, Post-Synthesis Modifications, and Their Optical Properties. *Chemical Reviews* **2019**, *119* (5), 3296-3348.

(17) Stoumpos, C. C.; Kanatzidis, M. G. The Renaissance of Halide Perovskites and Their Evolution as Emerging Semiconductors. *Accounts of Chemical Research* **2015**, *48* (10), 2791-2802.

(18) Goldschmidt, V. M. Die Gesetze der Krystallochemie. *Naturwissenschaften* **1926**, *14* (21), 477-485.

(19) Travis, W.; Glover, E.; Bronstein, H.; Scanlon, D.; Palgrave, R. On the application of the tolerance factor to inorganic and hybrid halide perovskites: a revised system. *Chemical science* **2016**, *7* (7), 4548-4556.

(20) Yi, Z.; Ladi, N. H.; Shai, X.; Li, H.; Shen, Y.; Wang, M. Will organic–inorganic hybrid halide lead perovskites be eliminated from optoelectronic applications? *Nanoscale Advances* **2019**, *1* (4), 1276-1289.

(21) Mitzi, D. B.; Chondroudis, K.; Kagan, C. R. Organic-inorganic electronics. *IBM journal of research and development* **2001**, *45* (1), 29-45.

(22) Mitzi, D. B.; Feild, C. A.; Harrison, W. T. A.; Guloy, A. M. Conducting tin halides with a layered organic-based perovskite structure. *Nature* **1994**, *369* (6480), 467-469.

(23) Kojima, A.; Teshima, K.; Shirai, Y.; Miyasaka, T. Organometal Halide Perovskites as Visible-Light Sensitizers for Photovoltaic Cells. *Journal of the American Chemical Society* **2009**, *131* (17), 6050-6051.

(24) Buin, A.; Comin, R.; Xu, J.; Ip, A. H.; Sargent, E. H. Halide-Dependent Electronic Structure of Organolead Perovskite Materials. *Chemistry of Materials* **2015**, *27* (12), 4405-4412.

(25) Zhou, Y.; Zhao, Y. Chemical stability and instability of inorganic halide perovskites. *Energy & environmental science* **2019**, *12* (5), 1495-1511.

(26) Umebayashi, T.; Asai, K.; Kondo, T.; Nakao, A. Electronic structures of lead iodide based low-dimensional crystals. *Physical Review B* **2003**, *67* (15), 155405.

(27) Butler, K. T.; Frost, J. M.; Walsh, A. Band alignment of the hybrid halide perovskites $CH_3NH_3PbCl_3$, $CH_3NH_3PbBr_3$ and $CH_3NH_3PbI_3$. *Materials Horizons* **2015**, *2* (2), 228-231.

(28) Knutson, J. L.; Martin, J. D.; Mitzi, D. B. Tuning the Band Gap in Hybrid Tin Iodide Perovskite Semiconductors Using Structural Templating. *Inorganic Chemistry* **2005**, *44* (13), 4699-4705.

(29) Tao, S.; Schmidt, I.; Brocks, G.; Jiang, J.; Tranca, I.; Meerholz, K.; Olthof, S. Absolute energy level positions in tin- and lead-based halide perovskites. *Nature Communications* **2019**, *10* (1), 2560.

(30) Protesescu, L.; Yakunin, S.; Bodnarchuk, M. I.; Krieg, F.; Caputo, R.; Hendon, C. H.; Yang, R. X.; Walsh, A.; Kovalenko, M. V. Nanocrystals of Cesium Lead Halide Perovskites ($CsPbX_3$, X = Cl, Br, and I): Novel Optoelectronic Materials Showing Bright Emission with Wide Color Gamut. *Nano Letters* **2015**, *15* (6), 3692-3696.

(31) Zhao, B.; Abdi-Jalebi, M.; Tabachnyk, M.; Glass, H.; Kamboj, V. S.; Nie, W.; Pearson, A. J.; Puttisong, Y.; Gödel, K. C.; Beere, H. E. High open-circuit voltages in tin-rich low-bandgap perovskite-based planar heterojunction photovoltaics. *Advanced materials* **2017**, *29* (2), 1604744.

(32) Gholipour, S.; Saliba, M. Bandgap tuning and compositional exchange for lead halide perovskite materials. In *Characterization Techniques for Perovskite Solar Cell Materials*, Elsevier, 2020; pp 1-22.

(33) Saliba, M.; Correa-Baena, J. P.; Grätzel, M.; Hagfeldt, A.; Abate, A. Perovskite solar cells: from the atomic level to film quality and device performance. *Angewandte Chemie International Edition* **2018**, *57* (10), 2554-2569.

(34) Yin, W.-J.; Yang, J.-H.; Kang, J.; Yan, Y.; Wei, S.-H. Halide perovskite materials for solar cells: a theoretical review. *Journal of Materials Chemistry A* **2015**, *3* (17), 8926-8942.

(35) Queisser, H. J.; Haller, E. E. Defects in Semiconductors: Some Fatal, Some Vital. *Science* **1998**, *281* (5379), 945-950.

(36) Huang, H.; Bodnarchuk, M. I.; Kershaw, S. V.; Kovalenko, M. V.; Rogach, A. L. Lead Halide Perovskite Nanocrystals in the Research Spotlight: Stability and Defect Tolerance. *ACS Energy Letters* **2017**, *2* (9), 2071-2083.

(37) Miyata, K.; Meggiolaro, D.; Trinh, M. T.; Joshi, P. P.; Mosconi, E.; Jones, S. C.; De Angelis, F.; Zhu, X.-Y. Large polarons in lead halide perovskites. *Science Advances* **2017**, *3* (8), e1701217.

(38) Brandt, R. E.; Poindexter, J. R.; Gorai, P.; Kurchin, R. C.; Hoye, R. L. Z.; Nienhaus, L.; Wilson, M. W. B.; Polizzotti, J. A.; Sereika, R.; Žaltauskas, R.; et al. Searching for "Defect-Tolerant" Photovoltaic Materials: Combined Theoretical and Experimental Screening. *Chemistry of Materials* **2017**, *29* (11), 4667-4674.

(39) Lee, M. M.; Teuscher, J.; Miyasaka, T.; Murakami, T. N.; Snaith, H. J. Efficient Hybrid Solar Cells Based on Meso-Superstructured Organometal Halide Perovskites. *Science* **2012**, *338* (6107), 643-647.

(40) Heo, J. H.; Im, S. H.; Noh, J. H.; Mandal, T. N.; Lim, C.-S.; Chang, J. A.; Lee, Y. H.; Kim, H.-j.; Sarkar, A.; Nazeeruddin, M. K.; et al. Efficient inorganic–organic hybrid heterojunction solar cells containing perovskite compound and polymeric hole conductors. *Nature Photonics* **2013**, *7* (6), 486-491.

(41) Tan, Z.-K.; Moghaddam, R. S.; Lai, M. L.; Docampo, P.; Higler, R.; Deschler, F.; Price, M.; Sadhanala, A.; Pazos, L. M.; Credgington, D.; et al. Bright light-emitting diodes based on organometal halide perovskite. *Nature Nanotechnology* **2014**, *9* (9), 687-692.

(42) Yuan, M.; Quan, L. N.; Comin, R.; Walters, G.; Sabatini, R.; Voznyy, O.; Hoogland, S.; Zhao, Y.; Beauregard, E. M.; Kanjanaboos, P.; et al. Perovskite energy funnels for efficient light-emitting diodes. *Nature Nanotechnology* **2016**, *11* (10), 872-877.

(43) Wang, N.; Cheng, L.; Ge, R.; Zhang, S.; Miao, Y.; Zou, W.; Yi, C.; Sun, Y.; Cao, Y.; Yang, R.; et al. Perovskite light-emitting diodes based on solution-processed self-organized multiple quantum wells. *Nature Photonics* **2016**, *10* (11), 699-704.

(44) Elkhouly, K.; Goldberg, I.; Zhang, X.; Annavarapu, N.; Hamdad, S.; Croes, G.; Rolin, C.; Genoe, J.; Qiu, W.; Gehlhaar, R.; et al. Electrically assisted amplified spontaneous emission in perovskite light-emitting diodes. *Nature Photonics* **2024**, 1-7.

(45) Huang, C.-Y.; Zou, C.; Mao, C.; Corp, K. L.; Yao, Y.-C.; Lee, Y.-J.; Schlenker, C. W.; Jen, A. K.; Lin, L. Y. $CsPbBr_3$ perovskite quantum dot vertical cavity lasers with low threshold and high stability. *Acs Photonics* **2017**, *4* (9), 2281-2289.

(46) Kim, H.; Roh, K.; Murphy, J. P.; Zhao, L.; Gunnarsson, W. B.; Longhi, E.; Barlow, S.; Marder, S. R.; Rand, B. P.; Giebink, N. C. Optically pumped lasing from hybrid perovskite light-emitting diodes. *Advanced Optical Materials* **2020**, *8* (1), 1901297.

(47) Saidaminov, M. I.; Adinolfi, V.; Comin, R.; Abdelhady, A. L.; Peng, W.; Dursun, I.; Yuan, M.; Hoogland, S.; Sargent, E. H.; Bakr, O. M. Planar-integrated single-crystalline perovskite photodetectors. *Nature Communications* **2015**, *6* (1), 8724.

(48) National Renewable Energy Laboratory (NREL), Champion photovoltaic module efficiency chart (2024). https://www.nrel.gov/pv/interactive-cell-efficiency.html. Accessed 4 Feb. 2024.

(49) Chondroudis, K.; Mitzi, D. B. Electroluminescence from an Organic−Inorganic Perovskite Incorporating a Quaterthiophene Dye within Lead Halide Perovskite Layers. *Chemistry of Materials* **1999**, *11* (11), 3028-3030.

(50) Zhao, B.; Bai, S.; Kim, V.; Lamboll, R.; Shivanna, R.; Auras, F.; Richter, J. M.; Yang, L.; Dai, L.; Alsari, M.; et al. High-efficiency perovskite–polymer bulk heterostructure light-emitting diodes. *Nature Photonics* **2018**, *12* (12), 783-789.

(51) Cao, Y.; Wang, N.; Tian, H.; Guo, J.; Wei, Y.; Chen, H.; Miao, Y.; Zou, W.; Pan, K.; He, Y.; et al. Perovskite light-emitting diodes based on spontaneously formed submicrometre-scale structures. *Nature* **2018**, *562* (7726), 249-253.

(52) Chiba, T.; Hayashi, Y.; Ebe, H.; Hoshi, K.; Sato, J.; Sato, S.; Pu, Y.-J.; Ohisa, S.; Kido, J. Anion-exchange red perovskite quantum dots with ammonium iodine salts for highly efficient light-emitting devices. *Nature Photonics* **2018**, *12* (11), 681-687.

(53) Yakunin, S.; Protesescu, L.; Krieg, F.; Bodnarchuk, M. I.; Nedelcu, G.; Humer, M.; De Luca, G.; Fiebig, M.; Heiss, W.; Kovalenko, M. V. Low-threshold amplified spontaneous emission and lasing from colloidal nanocrystals of caesium lead halide perovskites. *Nature Communications* **2015**, *6* (1), 8056.

(54) Wu, D.; Zhang, Y.; Liu, C.; Sun, Z.; Wang, Z.; Lin, Z.; Qiu, M.; Fu, D.; Wang, K. Recent Progress of Narrowband Perovskite Photodetectors: Fundamental Physics and Strategies. *Advanced Devices & Instrumentation* **2023**, *4*, 0006.

(55) Garoz-Ruiz, J.; Perales-Rondon, J. V.; Heras, A.; Colina, A. Spectroelectrochemistry of quantum dots. *Israel Journal of Chemistry* **2019**, *59* (8), 679-694.

(56) Busatto, S.; de Mello Donega, C. Magic-Size Semiconductor Nanostructures: Where Does the Magic Come from? *ACS Materials Au* **2022**, *2* (3), 237-249.

(57) Otero-Martínez, C.; García-Lojo, D.; Pastoriza-Santos, I.; Pérez-Juste, J.; Polavarapu, L. Dimensionality control of inorganic and hybrid perovskite nanocrystals by reaction temperature: from no-confinement to 3D and 1D quantum confinement. *Angewandte Chemie International Edition* **2021**, *60* (51), 26677-26684.

(58) Mondal, N.; De, A.; Samanta, A. Achieving Near-Unity Photoluminescence Efficiency for Blue-Violet-Emitting Perovskite Nanocrystals. *ACS Energy Letters* **2019**, *4* (1), 32-39.

(59) Gualdrón-Reyes, A. F.; Masi, S.; Mora-Seró, I. Progress in halide-perovskite nanocrystals with near-unity photoluminescence quantum yield. *Trends in Chemistry* **2021**, *3* (6), 499-511.

(60) Murray, C. B.; Norris, D. J.; Bawendi, M. G. Synthesis and characterization of nearly monodisperse CdE (E = sulfur, selenium, tellurium) semiconductor nanocrystallites. *Journal of the American Chemical Society* **1993**, *115* (19), 8706-8715.

(61) Zhang, Y.; Siegler, T. D.; Thomas, C. J.; Abney, M. K.; Shah, T.; De Gorostiza, A.; Greene, R. M.; Korgel, B. A. A "Tips and Tricks" Practical Guide to the Synthesis of Metal Halide Perovskite Nanocrystals. *Chemistry of Materials* **2020**, *32* (13), 5410-5423.

(62) Vybornyi, O.; Yakunin, S.; Kovalenko, M. V. Polar-solvent-free colloidal synthesis of highly luminescent alkylammonium lead halide perovskite nanocrystals. *Nanoscale* **2016**, *8* (12), 6278-6283.

(63) Papagiorgis, P.; Manoli, A.; Michael, S.; Bernasconi, C.; Bodnarchuk, M. I.; Kovalenko, M. V.; Othonos, A.; Itskos, G. Unraveling the Radiative Pathways of Hot Carriers upon Intense Photoexcitation of Lead Halide Perovskite Nanocrystals. *ACS Nano* **2019**, *13* (5), 5799-5809.

(64) Lignos, I.; Stavrakis, S.; Nedelcu, G.; Protesescu, L.; deMello, A. J.; Kovalenko, M. V. Synthesis of Cesium Lead Halide Perovskite Nanocrystals in a Droplet-Based Microfluidic Platform: Fast Parametric Space Mapping. *Nano Letters* **2016**, *16* (3), 1869-1877.

(65) Papavassiliou, G. C.; Pagona, G.; Karousis, N.; Mousdis, G. A.; Koutselas, I.;

Vassilakopoulou, A. Nanocrystalline/microcrystalline materials based on lead-halide units. *Journal of Materials Chemistry* **2012**, *22* (17), 8271-8280.

(66) Malik, M. A.; Wani, M. Y.; Hashim, M. A. Microemulsion method: A novel route to synthesize organic and inorganic nanomaterials: 1st Nano Update. *Arabian journal of Chemistry* **2012**, *5* (4), 397-417.

(67) Huang, H.; Zhao, F.; Liu, L.; Zhang, F.; Wu, X.-g.; Shi, L.; Zou, B.; Pei, Q.; Zhong, H. Emulsion Synthesis of Size-Tunable $CH_3NH_3PbBr_3$ Quantum Dots: An Alternative Route toward Efficient Light-Emitting Diodes. *ACS Applied Materials & Interfaces* **2015**, *7* (51), 28128-28133.

(68) Clinckemalie, L.; Valli, D.; Roeffaers, M. B. J.; Hofkens, J.; Pradhan, B.; Debroye, E. Challenges and Opportunities for $CsPbBr_3$ Perovskites in Low- and High-Energy Radiation Detection. *ACS Energy Letters* **2021**, *6* (4), 1290-1314.

(69) Chen, M.; Zou, Y.; Wu, L.; Pan, Q.; Yang, D.; Hu, H.; Tan, Y.; Zhong, Q.; Xu, Y.; Liu, H. Solvothermal synthesis of high-quality all-inorganic cesium lead halide perovskite nanocrystals: from nanocube to ultrathin nanowire. *Advanced Functional Materials* **2017**, *27* (23), 1701121.

(70) Zhai, W.; Lin, J.; Li, Q.; Zheng, K.; Huang, Y.; Yao, Y.; He, X.; Li, L.; Yu, C.; Liu, C. Solvothermal synthesis of ultrathin cesium lead halide perovskite nanoplatelets with tunable lateral sizes and their reversible transformation into Cs_4PbBr_6 nanocrystals. *Chemistry of Materials* **2018**, *30* (11), 3714-3721.

(71) Nedelcu, G.; Protesescu, L.; Yakunin, S.; Bodnarchuk, M. I.; Grotevent, M. J.; Kovalenko, M. V. Fast Anion-Exchange in Highly Luminescent Nanocrystals of Cesium Lead Halide Perovskites ($CsPbX_3$, X = Cl, Br, I). *Nano Letters* **2015**, *15* (8), 5635-5640.

(72) Hills-Kimball, K.; Nagaoka, Y.; Cao, C.; Chaykovsky, E.; Chen, O. Synthesis of formamidinium lead halide perovskite nanocrystals through solid–liquid–solid cation exchange. *Journal of Materials Chemistry C* **2017**, *5* (23), 5680-5684.

(73) Otero-Martínez, C.; Imran, M.; Schrenker, N. J.; Ye, J.; Ji, K.; Rao, A.; Stranks, S. D.; Hoye, R. L.; Bals, S.; Manna, L. Fast A-site cation cross-exchange at room

temperature: single-to double-and triple-cation halide perovskite nanocrystals. *Angewandte Chemie* **2022**, *134* (34), e202205617.

(74) van der Stam, W.; Geuchies, J. J.; Altantzis, T.; van den Bos, K. H. W.; Meeldijk, J. D.; Van Aert, S.; Bals, S.; Vanmaekelbergh, D.; de Mello Donega, C. Highly Emissive Divalent-Ion-Doped Colloidal $CsPb_{1-x}M_xBr_3$ Perovskite Nanocrystals through Cation Exchange. *Journal of the American Chemical Society* **2017**, *139* (11), 4087-4097.

(75) Hills-Kimball, K.; Pérez, M. J.; Nagaoka, Y.; Cai, T.; Yang, H.; Davis, A. H.; Zheng, W.; Chen, O. Ligand Engineering for Mn^{2+} Doping Control in $CsPbCl_3$ Perovskite Nanocrystals via a Quasi-Solid–Solid Cation Exchange Reaction. *Chemistry of Materials* **2020**, *32* (6), 2489-2500.

(76) Shamsi, J.; Dang, Z.; Ijaz, P.; Abdelhady, A. L.; Bertoni, G.; Moreels, I.; Manna, L. Colloidal CsX (X = Cl, Br, I) Nanocrystals and Their Transformation to $CsPbX_3$ Nanocrystals by Cation Exchange. *Chemistry of Materials* **2018**, *30* (1), 79-83.

(77) Pan, A.; He, B.; Fan, X.; Liu, Z.; Urban, J. J.; Alivisatos, A. P.; He, L.; Liu, Y. Insight into the Ligand-Mediated Synthesis of Colloidal $CsPbBr_3$ Perovskite Nanocrystals: The Role of Organic Acid, Base, and Cesium Precursors. *ACS Nano* **2016**, *10* (8), 7943-7954.

(78) Imran, M.; Di Stasio, F.; Dang, Z.; Canale, C.; Khan, A. H.; Shamsi, J.; Brescia, R.; Prato, M.; Manna, L. Colloidal Synthesis of Strongly Fluorescent $CsPbBr_3$ Nanowires with Width Tunable down to the Quantum Confinement Regime. *Chemistry of Materials* **2016**, *28* (18), 6450-6454.

(79) Pradhan, N. Alkylammonium Halides for Facet Reconstruction and Shape Modulation in Lead Halide Perovskite Nanocrystals. *Accounts of Chemical Research* **2021**, *54* (5), 1200-1208.

(80) Peng, L.; Dutta, S. K.; Mondal, D.; Hudait, B.; Shyamal, S.; Xie, R.; Mahadevan, P.; Pradhan, N. Arm Growth and Facet Modulation in Perovskite Nanocrystals. *Journal of the American Chemical Society* **2019**, *141* (40), 16160-16168.

(81) Pradhan, N. Why Do Perovskite Nanocrystals Form Nanocubes and How Can

Their Facets Be Tuned? A Perspective from Synthetic Prospects. *ACS Energy Letters* **2021**, *6* (1), 92-99.

(82) Sun, S.; Yuan, D.; Xu, Y.; Wang, A.; Deng, Z. Ligand-Mediated Synthesis of Shape-Controlled Cesium Lead Halide Perovskite Nanocrystals via Reprecipitation Process at Room Temperature. *ACS Nano* **2016**, *10* (3), 3648-3657.

(83) Fassl, P.; Lami, V.; Bausch, A.; Wang, Z.; Klug, M. T.; Snaith, H. J.; Vaynzof, Y. Fractional deviations in precursor stoichiometry dictate the properties, performance and stability of perovskite photovoltaic devices. *Energy & environmental science* **2018**, *11* (12), 3380-3391.

(84) Liu, F.; Zhang, Y.; Ding, C.; Kobayashi, S.; Izuishi, T.; Nakazawa, N.; Toyoda, T.; Ohta, T.; Hayase, S.; Minemoto, T.; et al. Highly Luminescent Phase-Stable $CsPbI_3$ Perovskite Quantum Dots Achieving Near 100% Absolute Photoluminescence Quantum Yield. *ACS Nano* **2017**, *11* (10), 10373-10383.

(85) Dutta, A.; Behera, R. K.; Pal, P.; Baitalik, S.; Pradhan, N. Near-unity photoluminescence quantum efficiency for all $CsPbX_3$ (X= Cl, Br, and I) perovskite nanocrystals: a generic synthesis approach. *Angewandte Chemie International Edition* **2019**, *58* (17), 5552-5556.

(86) Imran, M.; Caligiuri, V.; Wang, M.; Goldoni, L.; Prato, M.; Krahne, R.; De Trizio, L.; Manna, L. Benzoyl Halides as Alternative Precursors for the Colloidal Synthesis of Lead-Based Halide Perovskite Nanocrystals. *Journal of the American Chemical Society* **2018**, *140* (7), 2656-2664.

(87) Paul, S.; Samanta, A. N-Bromosuccinimide as Bromide Precursor for Direct Synthesis of Stable and Highly Luminescent Green-Emitting Perovskite Nanocrystals. *ACS Energy Letters* **2020**, *5* (1), 64-69.

(88) Dutta, S. K.; Peng, L.; Hudait, B.; Xie, R.; Pradhan, N. Halide Perovskite Cluster Precursors: A Paradigm for Obtaining Structure- and Color-Tunable Light-Emitting Nanocrystals. *ACS Energy Letters* **2022**, *7* (9), 3177-3186.

(89) Liu, Q.; Yin, J.; Zhang, B.-B.; Chen, J.-K.; Zhou, Y.; Zhang, L.-M.; Wang, L.-

M.; Zhao, Q.; Hou, J.; Shu, J. Theory-guided synthesis of highly luminescent colloidal cesium tin halide perovskite nanocrystals. *Journal of the American Chemical Society* **2021**, *143* (14), 5470-5480.

(90) Pan, J.; Shang, Y.; Yin, J.; De Bastiani, M.; Peng, W.; Dursun, I.; Sinatra, L.; El-Zohry, A. M.; Hedhili, M. N.; Emwas, A.-H.; et al. Bidentate Ligand-Passivated $CsPbI_3$ Perovskite Nanocrystals for Stable Near-Unity Photoluminescence Quantum Yield and Efficient Red Light-Emitting Diodes. *Journal of the American Chemical Society* **2018**, *140* (2), 562-565.

(91) Krieg, F.; Ochsenbein, S. T.; Yakunin, S.; ten Brinck, S.; Aellen, P.; Süess, A.; Clerc, B.; Guggisberg, D.; Nazarenko, O.; Shynkarenko, Y.; et al. Colloidal $CsPbX_3$ (X = Cl, Br, I) Nanocrystals 2.0: Zwitterionic Capping Ligands for Improved Durability and Stability. *ACS Energy Letters* **2018**, *3* (3), 641-646.

(92) Mondal, N.; De, A.; Samanta, A. Achieving near-unity photoluminescence efficiency for blue-violet-emitting perovskite nanocrystals. *ACS Energy Letters* **2018**, *4* (1), 32-39.

(93) Pan, G.; Bai, X.; Yang, D.; Chen, X.; Jing, P.; Qu, S.; Zhang, L.; Zhou, D.; Zhu, J.; Xu, W. Doping lanthanide into perovskite nanocrystals: highly improved and expanded optical properties. *Nano letters* **2017**, *17* (12), 8005-8011.

(94) Yao, J.-S.; Ge, J.; Wang, K.-H.; Zhang, G.; Zhu, B.-S.; Chen, C.; Zhang, Q.; Luo, Y.; Yu, S.-H.; Yao, H.-B. Few-Nanometer-Sized α-$CsPbI_3$ Quantum Dots Enabled by Strontium Substitution and Iodide Passivation for Efficient Red-Light Emitting Diodes. *Journal of the American Chemical Society* **2019**, *141* (5), 2069-2079.

(95) Yong, Z.-J.; Guo, S.-Q.; Ma, J.-P.; Zhang, J.-Y.; Li, Z.-Y.; Chen, Y.-M.; Zhang, B.-B.; Zhou, Y.; Shu, J.; Gu, J.-L. Doping-enhanced short-range order of perovskite nanocrystals for near-unity violet luminescence quantum yield. *Journal of the American Chemical Society* **2018**, *140* (31), 9942-9951.

(96) Shao, H.; Bai, X.; Cui, H.; Pan, G.; Jing, P.; Qu, S.; Zhu, J.; Zhai, Y.; Dong, B.; Song, H. White light emission in Bi^{3+}/Mn^{2+} ion co-doped $CsPbCl_3$ perovskite

nanocrystals. *Nanoscale* **2018**, *10* (3), 1023-1029.

(97) Milstein, T. J.; Kroupa, D. M.; Gamelin, D. R. Picosecond Quantum Cutting Generates Photoluminescence Quantum Yields Over 100% in Ytterbium-Doped $CsPbCl_3$ Nanocrystals. *Nano Letters* **2018**, *18* (6), 3792-3799.

(98) Li, X.; Gao, X.; Zhang, X.; Shen, X.; Lu, M.; Wu, J.; Shi, Z.; Colvin, V. L.; Hu, J.; Bai, X. Lead-free halide perovskites for light emission: recent advances and perspectives. *Advanced science* **2021**, *8* (4), 2003334.

(99) Giustino, F.; Snaith, H. J. Toward Lead-Free Perovskite Solar Cells. *ACS Energy Letters* **2016**, *1* (6), 1233-1240.

(100) Ke, W.; Stoumpos, C. C.; Kanatzidis, M. G. "Unleaded" perovskites: status quo and future prospects of tin-based perovskite solar cells. *Advanced Materials* **2019**, *31* (47), 1803230.

(101) Yuan, F.; Folpini, G.; Liu, T.; Singh, U.; Treglia, A.; Lim, J. W. M.; Klarbring, J.; Simak, S. I.; Abrikosov, I. A.; Sum, T. C.; et al. Bright and stable near-infrared lead-free perovskite light-emitting diodes. *Nature Photonics* **2024**, 1-7.

(102) Ning, W.; Gao, F. Structural and functional diversity in lead-free halide perovskite materials. *Advanced Materials* **2019**, *31* (22), 1900326.

(103) Roknuzzaman, M.; Ostrikov, K.; Wang, H.; Du, A.; Tesfamichael, T. Towards lead-free perovskite photovoltaics and optoelectronics by ab-initio simulations. *Scientific Reports* **2017**, *7* (1), 14025.

(104) Zhao, X.-G.; Yang, J.-H.; Fu, Y.; Yang, D.; Xu, Q.; Yu, L.; Wei, S.-H.; Zhang, L. Design of Lead-Free Inorganic Halide Perovskites for Solar Cells via Cation-Transmutation. *Journal of the American Chemical Society* **2017**, *139* (7), 2630-2638.

(105) Meng, W.; Wang, X.; Xiao, Z.; Wang, J.; Mitzi, D. B.; Yan, Y. Parity-Forbidden Transitions and Their Impact on the Optical Absorption Properties of Lead-Free Metal Halide Perovskites and Double Perovskites. *The Journal of Physical Chemistry Letters* **2017**, *8* (13), 2999-3007.

(106) Slavney, A. H.; Hu, T.; Lindenberg, A. M.; Karunadasa, H. I. A Bismuth-

Halide Double Perovskite with Long Carrier Recombination Lifetime for Photovoltaic Applications. *Journal of the American Chemical Society* **2016**, *138* (7), 2138-2141.

(107) Tran, M. N.; Cleveland, I. J.; Aydil, E. S. Reactive Physical Vapor Deposition of Yb-Doped Lead-Free Double Perovskite $Cs_2AgBiBr_6$ with 95% Photoluminescence Quantum Yield. *ACS Applied Electronic Materials* **2022**, *4* (9), 4588-4594.

(108) Ji, F.; Klarbring, J.; Wang, F.; Ning, W.; Wang, L.; Yin, C.; Figueroa, J. S. M.; Christensen, C. K.; Etter, M.; Ederth, T.; et al. Lead-Free Halide Double Perovskite $Cs_2AgBiBr_6$ with Decreased Band Gap. *Angewandte Chemie International Edition* **2020**, *59* (35), 15191-15194.

(109) Li, S.; Shi, Z.; Zhang, F.; Wang, L.; Ma, Z.; Wu, D.; Yang, D.; Chen, X.; Tian, Y.; Zhang, Y.; et al. Ultrastable Lead-Free Double Perovskite Warm-White Light-Emitting Devices with a Lifetime above 1000 Hours. *ACS Applied Materials & Interfaces* **2020**, *12* (41), 46330-46339.

(110) Luo, J.; Wang, X.; Li, S.; Liu, J.; Guo, Y.; Niu, G.; Yao, L.; Fu, Y.; Gao, L.; Dong, Q.; et al. Efficient and stable emission of warm-white light from lead-free halide double perovskites. *Nature* **2018**, *563* (7732), 541-545.

(111) Jin, S.; Yuan, H.; Pang, T.; Zhang, M.; He, Y.; Zhuang, B.; Wu, T.; Zheng, Y.; Chen, D. Boosting STE and Nd^{3+} NIR Luminescence in $Cs_2AgInCl_6$ Double Perovskite via Na^+/Bi^{3+}-Induced Local Structure Engineering. *Advanced Functional Materials* **2023**, *33* (50), 2304577.

(112) Xiao, Z.; Song, Z.; Yan, Y. From lead halide perovskites to lead-free metal halide perovskites and perovskite derivatives. *Advanced Materials* **2019**, *31* (47), 1803792.

(113) Saparov, B.; Hong, F.; Sun, J.-P.; Duan, H.-S.; Meng, W.; Cameron, S.; Hill, I. G.; Yan, Y.; Mitzi, D. B. Thin-Film Preparation and Characterization of $Cs_3Sb_2I_9$: A Lead-Free Layered Perovskite Semiconductor. *Chemistry of Materials* **2015**, *27* (16), 5622-5632.

(114) Zuo, C.; Ding, L. Lead-free Perovskite Materials $(NH_4)_3Sb_2I_xBr_{9-x}$.

Angewandte Chemie International Edition **2017**, *56* (23), 6528-6532.

(115) Jiang, F.; Yang, D.; Jiang, Y.; Liu, T.; Zhao, X.; Ming, Y.; Luo, B.; Qin, F.; Fan, J.; Han, H.; et al. Chlorine-Incorporation-Induced Formation of the Layered Phase for Antimony-Based Lead-Free Perovskite Solar Cells. *Journal of the American Chemical Society* **2018**, *140* (3), 1019-1027.

(116) Xiao, Z.; Zhou, Y.; Hosono, H.; Kamiya, T. Intrinsic defects in a photovoltaic perovskite variant Cs_2SnI_6. *Physical Chemistry Chemical Physics* **2015**, *17* (29), 18900-18903.

(117) Jellicoe, T. C.; Richter, J. M.; Glass, H. F. J.; Tabachnyk, M.; Brady, R.; Dutton, S. E.; Rao, A.; Friend, R. H.; Credgington, D.; Greenham, N. C.; et al. Synthesis and Optical Properties of Lead-Free Cesium Tin Halide Perovskite Nanocrystals. *Journal of the American Chemical Society* **2016**, *138* (9), 2941-2944.

(118) Wang, A.; Guo, Y.; Muhammad, F.; Deng, Z. Controlled Synthesis of Lead-Free Cesium Tin Halide Perovskite Cubic Nanocages with High Stability. *Chemistry of Materials* **2017**, *29* (15), 6493-6501.

(119) Kang, C.; Rao, H.; Fang, Y.; Zeng, J.; Pan, Z.; Zhong, X. Antioxidative Stannous Oxalate Derived Lead-Free Stable $CsSnX_3$ (X=Cl, Br, and I) Perovskite Nanocrystals. *Angewandte Chemie International Edition* **2021**, *60* (2), 660-665.

(120) Liu, Q.; Yin, J.; Zhang, B.-B.; Chen, J.-K.; Zhou, Y.; Zhang, L.-M.; Wang, L.-M.; Zhao, Q.; Hou, J.; Shu, J.; et al. Theory-Guided Synthesis of Highly Luminescent Colloidal Cesium Tin Halide Perovskite Nanocrystals. *Journal of the American Chemical Society* **2021**, *143* (14), 5470-5480.

(121) Liu, J.; Yao, H.; Wang, S.; Wu, C.; Ding, L.; Hao, F. Origins and Suppression of Sn(II)/Sn(IV) Oxidation in Tin Halide Perovskite Solar Cells. *Advanced Energy Materials* **2023**, *13* (23), 2300696.

(122) Lanzetta, L.; Webb, T.; Zibouche, N.; Liang, X.; Ding, D.; Min, G.; Westbrook, R. J. E.; Gaggio, B.; Macdonald, T. J.; Islam, M. S.; et al. Degradation mechanism of hybrid tin-based perovskite solar cells and the critical role of tin (IV) iodide. *Nature*

Communications **2021**, *12* (1), 2853.

(123) Saidaminov, M. I.; Spanopoulos, I.; Abed, J.; Ke, W.; Wicks, J.; Kanatzidis, M. G.; Sargent, E. H. Conventional Solvent Oxidizes Sn(II) in Perovskite Inks. *ACS Energy Letters* **2020**, *5* (4), 1153-1155.

(124) Abdel-Shakour, M.; Chowdhury, T. H.; Matsuishi, K.; Bedja, I.; Moritomo, Y.; Islam, A. High-Efficiency Tin Halide Perovskite Solar Cells: The Chemistry of Tin (II) Compounds and Their Interaction with Lewis Base Additives during Perovskite Film Formation. *Solar RRL* **2021**, *5* (1), 2000606.

(125) Wang, J.; Gao, Z.; Yang, J.; Lv, M.; Chen, H.; Xue, D.-J.; Meng, X.; Yang, S. Controlling the Crystallization Kinetics of Lead-Free Tin Halide Perovskites for High Performance Green Photovoltaics. *Advanced Energy Materials* **2021**, *11* (39), 2102131.

Chapter 2 Mechanistic Insight into the Precursor Chemistry of Cesium Tin Iodide Perovskite Nanocrystals

2.1 Introduction

Colloidal halide perovskite nanocrystals (NCs) have emerged as promising light-emissive building blocks for widespread applications in lasers, displays, light-emitting diodes (LEDs), scintillators, photovoltaics, and more over the past decade.[1-11] This rapid expansion of research into multiple fields has been driven by their low-cost synthesis and excellent photophysical properties, including tunable optical band gaps, large absorption cross sections, near-unity photoluminescence (PL) quantum yields (PLQYs), narrow PL full width at half-maximum, and fast radiative rate at low temperatures.[12-21] However, to date the most studied halide perovskite NCs, with the advantageous properties aforementioned, are Pb-containing compounds.[22,23] Although some halide perovskite NC-based optoelectronic devices, such as LEDs, have reached performance level in terms of external quantum efficiencies that are comparable to their commercial cousins, the presence of the heavily toxic Pb element severely shadows their commercial prospects due to the regulation on the use of Pb in consumer electronics as required by the EU's "Restriction of Hazardous Substances" (RoHS) directives.[24-28] Developing Pb-free, RoHS-compliant halide perovskite NCs, with comparable properties to their Pb-based counterparts, is therefore urgently needed.[29,30] Among possible alternatives, colloidal tin halide perovskite NCs with a general formula $ASnX_3$, where A is a monovalent cation such as cesium, methylammonium, or formamidinium and X is a halide anion or mixture thereof, have attracted much attention.[31] Nevertheless, the synthesis of colloidal $ASnX_3$ NCs is still in a primitive state compared to their $APbX_3$ cousins in terms of the rational control over the reactivity of reactants used for the synthesis, the understanding of reaction mechanisms, as well as the reproducibility of the synthesis.[31]

Akin to $APbX_3$ perovskites, $ASnX_3$ features high lattice ionicity and low lattice formation energies.[30,32] Thus, $ASnX_3$ perovskite NCs form too quickly during the ionic

coprecipitation, and bulk and surface defects can readily form.[33-40] Using SnX_2 as the tin and halide sources, in 2016 Jellicoe et al. first synthesized colloidal $CsSnX_3$ NCs by the hot-injection approach.[33] Subsequently, Wong et al. reported on the synthesis of strongly quantum confined colloidal cesium tin iodide perovskite nanoplates using SnI_2 as the tin and iodide sources.[34] To readily tune the feeding ratio of tin and halide, Kang et al. proposed the use of SnC_2O_4 and NH_4X as the tin and halide sources, respectively, which leads to the attainment of more stable $CsSnX_3$ NCs.[35] However, all of these approaches cannot effectively suppress the formation of PL-detrimental defects, and thus, all obtained $CsSnX_3$ NCs show a PLQY less than 1%. Recent theoretical results from us and co-workers suggested that it is impossible to suppress the formation of all defects by merely tuning chemical potentials of constituents of $CsSnX_3$ NCs.[36] Correspondingly, I proposed a colloidal synthesis approach that allows for fine-tuning of the ratio of the precursors over a wide range, in which cesium carbonate (Cs_2CO_3), tin(II) 2-ethylhexanoate ($Sn(Oct)_2$), and trimethylsilyl halide were employed as the Cs, Sn, and halide precursors, respectively. This enables us to obtain narrow-band-emissive $CsSnI_3$ NCs with a record PLQY of 18.4% by judiciously adopting a tin-rich reaction condition that can effectively suppress the occurrence of the most PL-deleterious tin vacancy. The aforementioned reports highlight the progress made in refining the synthesis of tin halide perovskite NCs. Yet, the reaction mechanism in the synthesis of these NCs, in particular the precursor chemistry in the case of using a tin(II) carboxylate as a precursor, is still poorly understood.[36] I took the view that an in-depth understanding of the precursor chemistry is of vital importance not only for the reproducible synthesis but also for offering guidelines toward $ASnX_3$ perovskite NCs with comparable optical properties of Pb-based counterparts.

Here, I aimed to obtain deeper insight into the precursor chemistry in the synthesis of $CsSnI_3$ perovskite NCs, and I uncover the key role of the precursors in affecting their morphology, size, size uniformity, and PLQY. The selection of the tin precursor emerges as a pivotal determinant significantly influencing the characteristics of the NCs. Based on

systematic characterizations, including Fourier-transform infrared spectroscopy (FTIR), electrospray ionization mass spectrometry (ESI-MS), and nuclear magnetic resonance (NMR) spectroscopy, I reveal that the chemical nature of the active precursor species, i.e., tin iodide polymeric complexes with varied reactivities, plays a key role in affecting the nuclei and growth of $CsSnI_3$ NCs. These findings have enabled a rational explanation of the formation mechanism underlying $CsSnI_3$ NCs and have provided insights into how to precisely modulate reaction conditions. This understanding not only facilitates the deliberate synthesis of $ASnX_3$ NCs but also holds promise for enhancing the fabrication process of high-quality polycrystalline $ASnX_3$ films.

2.2 Experimental Section

2.2.1 Chemicals and experimental

Chemicals

Cesium carbonate (Cs_2CO_3, Sigma, 99.995%), tin 2-ethylhexanoate ($Sn(Oct)_2$, Sigma, 92.5-100.0%), tin 2-ethylhexanoate ($Sn(Oct)_2$, TCI, >85.0%), trimethylsilyl iodide (TMSI, Sigma, 97%), tin(II) iodide (SnI_2, Alfa, 99.999%), 1-octadecene (ODE, Alfa, 90%), oleylamine (OAm, Acros, 80–90%), oleic acid (OA, Sigma, 90%), tri-n-octylphosphine (TOP, Alfa, 90%), chlorobenzene (Sigma, 99%), n-hexane (Wako, ≥96.0%), sodium 2-ethylhexanoate (TCI, >98.0%), 2-ethylhexanoic acid (TCI, >99.0%), methanol (Wako, ≥99.7%, for LC/MS), chloroform-D (Wako, 99.8%), and tetramethyltin (TCI, > 97%) were used without purification unless otherwise noted.

Thermal treatment of $Sn(Oct)_2$.

5 mL of $Sn(Oct)_2$ as received from Sigma was put into a three-neck round bottom flask, followed by thermal treatment at 130 °C for different durations under a dry N_2 gas flow (0.1 L/min). The treated $Sn(Oct)_2$ was transferred to an Ar-filled glovebox for further use.

Preparation of the Cs precursor.

Cs_2CO_3 (0.0448 g), OA (0.2 mL), OAm (0.2 mL), and ODE (6 mL) were mixed in

a 50 mL three-necked flask and dried for 1 h at 80 °C to remove residual water and oxygen. Subsequently, the mixture was heated at 100 °C for 30 min, and then heated under N_2 atmosphere to 180 °C to obtain a colorless Cs precursor solution. Afterwards, it was used for the synthesis of $CsSnI_3$ NCs or transferred to an Ar-filled glovebox for the study of the reactivity of the precursors.

Preparation of the TOP-Sn-I precursors and synthesis of $CsSnI_3$ NCs.

The TOP-Sn-I precursor solution was prepared by loading $Sn(Oct)_2$ (1.12 mL (3.38 mmol) for Sigma, or S-130-t $Sn(Oct)_2$, 1.2 mL (3.38 mmol) for TCI $Sn(Oct)_2$), 1.63 mL TOP and 0.344 mL (2.82 mmol) TMSI into a 20 mL glass bottle and stirring vigorously for 60 min in an Ar-filled glovebox. All $CsSnI_3$ NCs were synthesized by a hot-injection approach. While the Cs precursor solution was heated to 180 °C, the TOP-Sn-I precursor solution was quickly injected. After 1 min of reaction, the reaction mixture was cooled by an ice–water bath.

Isolation and purification of perovskite NCs.

The crude solution was transferred to an Ar-filled glovebox and then sealed into the centrifugating tubes that were centrifuged for 5 min at 4000 rpm. The precipitates were discarded, and a half volume of chlorobenzene was added into the supernatant and then mixtures were centrifuged again for 5 min at 12000 rpm. Finally, the resultant precipitates were collected as the final product and dispersed in hexane.

Reaction between the tin (II) carboxylate and TMSI.

In an Ar-filled glovebox, $Sn(Oct)_2$ as received from Sigma and TMSI were mixed in a 1:2 molar ratio. The mixture was centrifuged at 12000 rpm for 5 min and the precipitate was collected and analyzed using XRD.

Reaction between the tin (II) carboxylate and SnI_2.

$Sn(Oct)_2$ as received from Sigma was mixed with 5%, 10%, and 15% equivalent of TMSI. The mixture of $Sn(Oct)_2$ with 5% and 10% equivalent of TMSI was stirred at room temperature and gradually turned into a clear solution. On the other hand, the mixture of $Sn(Oct)_2$ with 15% equivalent of TMSI remained a turbid liquid. Control experiment by

mixing $Sn(Oct)_2$ as received from Sigma with 5% of ultra-dry SnI_2 particles (Alfa) was also carried out at the same conditions, and finally a clear solution was obtained.

Dissolution of SnI_2 by TOP.

In an Ar-filled glovebox, $Sn(Oct)_2$ as received from Sigma and TMSI were mixed in a 1:2 molar ratio. The mixture was added into 1.63 mL of TOP, then the yellow precipitate was rapidly dissolved. For the control experiment, 0.577 g of super-dry SnI_2 was mixed with 1.63 mL of TOP. After stirring for 60 min at room temperature, the SnI_2 microspheres were completely dissolved.

Reactivity of the TOP-Sn-I precursors.

In an Ar-filled glovebox, 1 mL of the Cs precursor stock solution is loaded into three types of TOP-Sn-I precursors (prepared with $Sn(Oct)_2$ as received from Sigma, S-130-40 min, and S-130-180 min). The mixtures were firstly stirred at room temperature for 1 min to observe the color change, and then kept stirring at 60°C until all the mixtures turned black.

2.2.2 Characterization

Structure, Morphology, FTIR, NMR, and ESI-MS Characterization.

XRD data were recorded on a MiniFlex 600 diffractometer (Rigaku) with Cu Kα radiation (λ = 1.5418 Å). The NCs were dispersed in hexane to form a concentrated NCs solution, and the solution was dropped on an anaerobic sample holder for the XRD measurements. TEM samples were prepared by dropping a dilute NC-hexane solution onto a TEM copper grid and dried in an Ar-filled glovebox. TEM images were measured by a JEM-2100F (JEOL) microscope operated at 200 kV. FTIR spectra were recorded using a Jasco 4100 FTIR spectrometer. NMR data were acquired on a JEOL ECS-400 spectrometer. For the NMR measurements, the samples were dispersed in chloroform-D, and the concentrations were consistent for the same series of samples (1.5 M for ^{119}Sn NMR, 0.69 M for ^{31}P NMR). The ^{119}Sn NMR spectrum was calibrated using tetramethyltin as an internal standard. ESI-MS spectra were measured by a Q-Exactive

Plus mass spectrometer (ThermoFisher Scientific) with an electrospray ion source.

Luminescence and Absorption Characterization.

The PL spectra were measured by a NanoLog Horiba Jovin Yvon spectrofluorometer with a continuous 450 W xenon lamp. The absolute PLQYs were measured by a C9920-03G system equipped with a 150 W xenon lamp (Hamamatsu Photonics). The PL decays were obtained with a time-correlated single photon counting lifetime spectroscopy system (NanoLog, Horiba Jovin Ybon), equipped with a pulse laser (λ_{em} = 726 nm). The absorption spectra were measured by a UV-vis-NIR spectrophotometer (V-770, JASCO).

Detailed method for the calculation of the average lifetime, radiative, and nonradiative recombination rates.

Using PLQYs and average lifetimes, I evaluated the radiative and nonradiative decay rates based on the following equations:

$$\tau_{ave} = (A_1\tau_1^2 + A_2\tau_2^2 + A_3\tau_3^2 + \cdots)/(A_1\tau_1 + A_2\tau_2 + A_3\tau_3 + \cdots) \quad (1)$$

$$\Gamma_{rad} = \frac{\mathrm{PLQY}}{\tau_{ave}} \quad (2)$$

$$\Gamma_{non-rad} = \frac{1}{\tau_{ave}} - \Gamma_{rad} = \frac{1 - \mathrm{PLQY}}{\tau_{ave}} \quad (3)$$

where A_i (i=1, 2, and 3) and τ_i (i=1, 2, and 3) are the amplitudes and the corresponding fitted lifetimes, respectively, τ_{ave} is the average lifetime of the samples, and Γ_{rad} and $\Gamma_{non\text{-}rad}$ are the radiative and non-radiative recombination rates, respectively.

2.3 Results and discussion

I selected $CsSnI_3$ NCs as a model system to glean an insight into the precursor chemistry in the synthesis mostly due to three reasons: (i) $CsSnI_3$ NCs have been lately at the forefront of tin-based perovskite NCs and show the highest PLQY among $ASnX_3$ NCs reported, and thus understanding their synthetic chemistry is important in order to rationally develop new protocols for NCs with a much higher PLQY as the next step.[36] (ii) Since $CsSnI_3$ NCs, synthesized by my developed approach, demonstrate moderate PLQYs, I can use this parameter as a probe for evaluating the quality of NCs. (iii) $CsSnI_3$ NCs, with a size over the exciton Bohr radius, have a band gap of around 1.3 eV, which

is technologically important because of their potential for use in solar cells.

I started by synthesizing $CsSnI_3$ NCs with an approach developed by us, in which $Sn(Oct)_2$ is employed as the tin precursor.[36] I note that the attainment of high-purity $Sn(Oct)_2$ is challenging and only low-purity $Sn(Oct)_2$ is commercially available; even from the same producer, different batches have different purities. Additionally, the color and viscosity of $Sn(Oct)_2$ as received from different producers (e.g., Sigma and TCI) showed some differences. All of these observations lead us to hypothesize that the initial chemical state of $Sn(Oct)_2$ could be an important synthetic parameter that might affect the reactivity of the precursors and thus the properties of the final NCs.

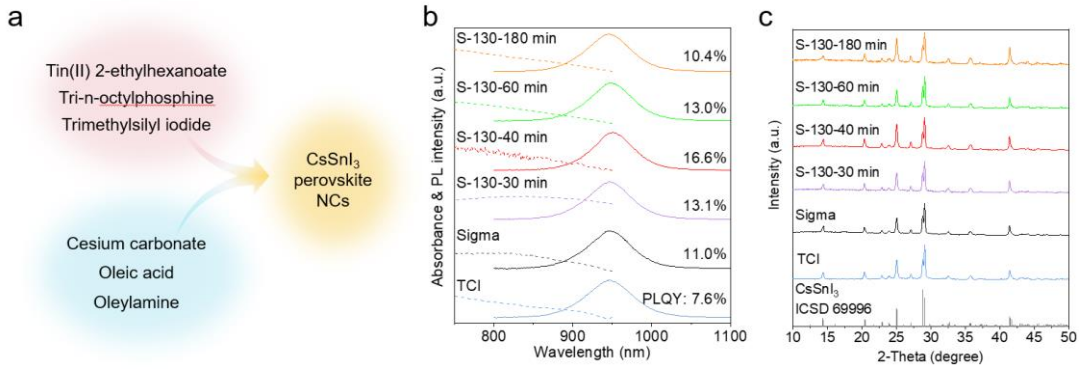

Figure 2.1 (a) Schematic of the synthesis of $CsSnI_3$ NCs via a hot-injection approach. Chemicals in the TOP-Sn-I precursor are $Sn(Oct)_2$, TOP and TMSI, while those in the Cs precursor are Cs_2CO_3, OA and OAm. (b) Normalized PL (solid lines) spectra and optical absorption (dashed lines) and PLQYs of $CsSnI_3$ NCs synthesized using $Sn(Oct)_2$ without and with thermal treatment. Note that the time shown in the figure is the duration of thermal treatment for $Sn(Oct)_2$ rather than the reaction time. The excitation wavelengths for the PL spectrum and PLQY are 730 nm. (c) XRD patterns of $CsSnI_3$ NCs synthesized using $Sn(Oct)_2$ without and with thermal treatment.

To test my hypothesis, I used $Sn(Oct)_2$ as received from Sigma and TCI with different purities for the synthesis of $CsSnI_3$ NCs (Table 2.1). In brief, I first prepared the TOP-Sn-I precursor by mixing $Sn(Oct)_2$ with trimethylsilyl iodide (TMSI) and tri-n-octylphosphine (TOP) at room temperature, and the Cs precursor was prepared by degassing a mixture of Cs_2CO_3, oleic acid (OA), and oleylamine (OAm) with 1-

octadecene at 80 °C that was followed by stirring and heating under nitrogen to 180 °C. After that, the TOP-Sn-I precursor was swiftly injected into the Cs precursor solution, and the reaction was quenched by cooling the reactor with an ice bath after 60 s. The synthesis process is schematically shown in **Figure 2.1a**, and the details are listed in Experimental Section. I point out that although the purities of $Sn(Oct)_2$ from Sigma and TCI are different, equimolar $Sn(Oct)_2$ is introduced in the reaction system based on the Certificate of Analysis provided by the producers (**Table 2.1**). Interestingly, I find that the $CsSnI_3$ NCs synthesized using $Sn(Oct)_2$ as received from Sigma and TCI, denoted Sigma and TCI, respectively, show different PLQYs (**Figure 2.1b and Figure 2.2**). Although both products are phase-pure and belong to the same crystal structure (**Figure 2.1c**), they show different sizes and size uniformities (**Figure 2.3**). All of these results signify that the tin(II) carboxylates used in the synthesis can influence the nucleation and/or growth of $CsSnI_3$ NCs.

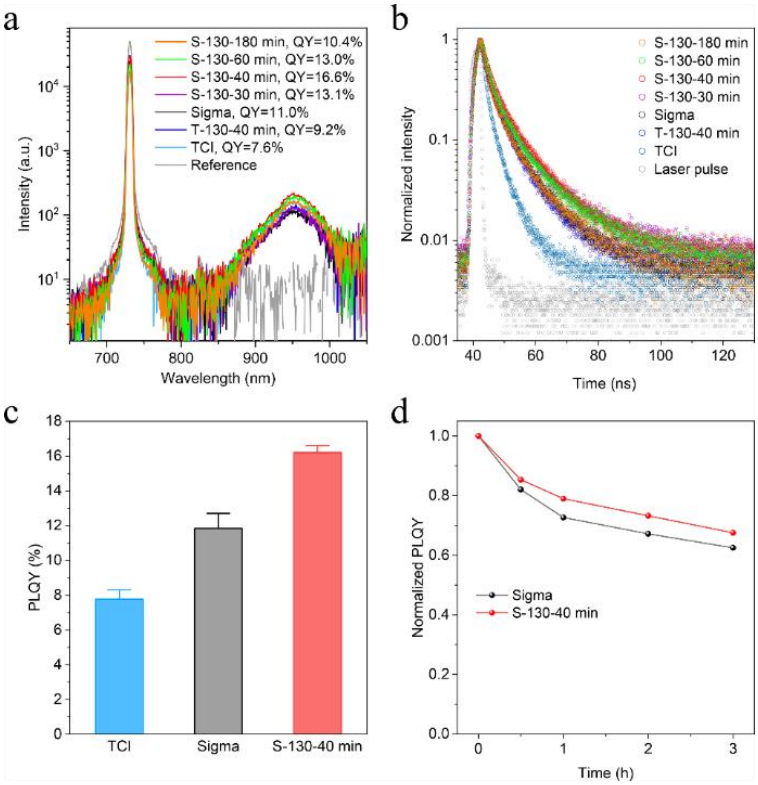

Figure 2.2 (a) PLQYs and (b) PL lifetimes of $CsSnI_3$ NCs synthesized using different $Sn(Oct)_2$. The PL excitation wavelength is 730 nm. (c) PLQYs of $CsSnI_3$ NCs synthesized using $Sn(Oct)_2$ from TCI and Sigma and S-130-40 min. The average PLQY and error bar were obtained by three parallel

experiments. (d) Stability of $CsSnI_3$ NCs synthesized using $Sn(Oct)_2$ from Sigma and S-130-40 min. The NCs were dispersed in hexane and fully exposed in air (22.4 ℃, 51% relative humidity) for different durations.

Table 2.1 Details of $Sn(Oct)_2$ from Sigma and TCI.

Producers	Product No.	Batch No.	Purity (%)		Appearance	Impurity
			Guide	Actual		
Sigma	S3252	SLCK2171	92.5~100.0	97.5	Very light-yellow liquid	Na < 0.2%
TCI	T3149	8LQAA	>85.0	91.2	Yellow clear liquid	Not showing

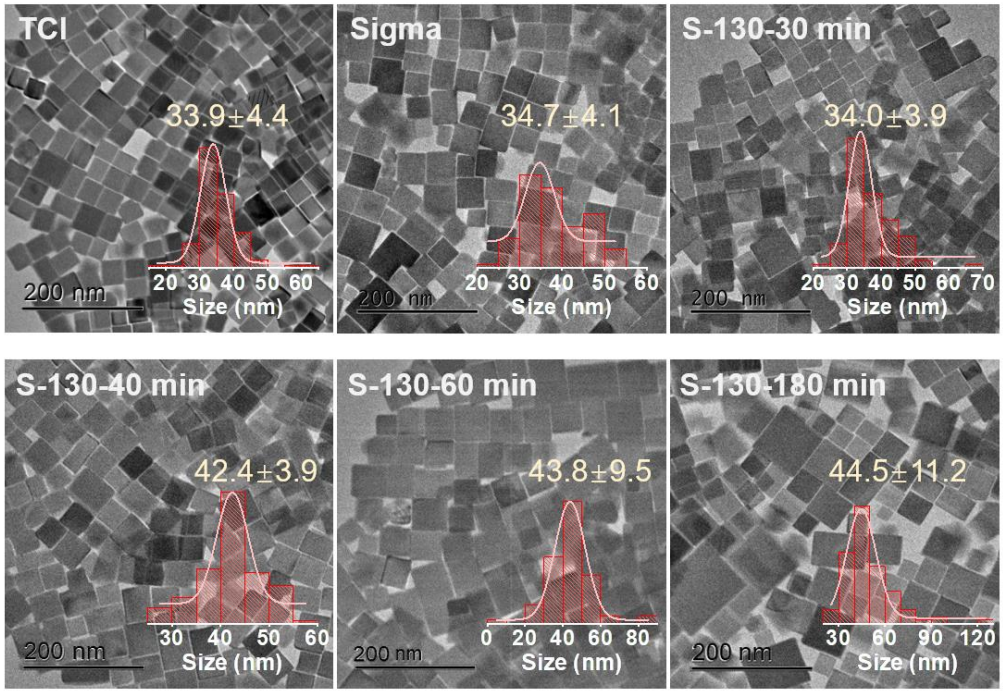

Figure 2.3 TEM images of $CsSnI_3$ NCs synthesized using $Sn(Oct)_2$ without and with thermal treatment. Insets show the histograms of edge lengths of the corresponding $CsSnI_3$ NCs. A Gaussian distribution function was utilized to describe the size distribution of the $CsSnI_3$ NCs.

Toward the goal of understanding the impact of $Sn(Oct)_2$ on the synthesis of $CsSnI_3$

NCs, I then pursued screening out the underlying factors that influence the initial state of $Sn(Oct)_2$. Inspired by the fact that metal 2-ethylhexanoates typically show various types of metal-carboxylate coordination and can exist as a dimeric or even polymeric form,[41-44] I reasoned that $Sn(Oct)_2$ from different producers could possess different molecular states probably as a result of the difference in the synthetic methods adopted. Since the thermal history of metal 2-ethylhexanoate can affect the coordination of metal and carboxylate, I then intentionally thermally treated $Sn(Oct)_2$ from Sigma under N_2 atmosphere; specifically, I set the treatment temperature at 130 °C and varied the treatment duration ranging from 30 to 180 min. I find that the thermally treated $Sn(Oct)_2$ becomes more and more viscous with the increase of the treatment duration; the obtained tin sources after thermal treatment of $Sn(Oct)_2$ from Sigma and TCI are denoted as S-130-t and T-130-t, respectively, where t is the treatment duration. I then used them for the subsequent synthesis of NCs. Astonishingly, I find that the obtained NCs using S-130-t and T-130-t show quite different PLQYs (**Figure 2.1b and Figure 2.2a**); with increasing the treatment duration, the PLQY first increases and reaches the maximum of 16.6% for S-130-40 min, which is over two times that of NCs synthesized by $Sn(Oct)_2$ from TCI. However, the PLQY of $CsSnI_3$ NCs decreases when the treatment time is longer than 40 min. Interestingly, I note that the PLQYs have the same variation trend as the PL decays (i.e., a higher PLQY corresponds to a slower decay), indicating that the change in PLQYs is caused by the difference in the NCs' trap density rather than the size (**Figure 2.2b**). Based on the PLQYs and average lifetimes, I roughly estimated the radiative and nonradiative recombination rates (**Table 2.2**). Obviously, $CsSnI_3$ NCs with high PLQY have a greatly reduced rate of nonradiative recombination, which laterally reflects the decrease trap density in these NCs.

Table 2.2. Fitting results of PL decay curves, τ_{ave}, PLQYs, radiative (Γ_{rad}) and nonradiative ($\Gamma_{non\text{-}rad}$) decay rates of $CsSnI_3$ NCs. Note that the decays were fitted with a triple-exponential function.

Sample	A_1	τ_1 (ns)	A_2	τ_2 (ns)	A_3	τ_3 (ns)	τ_{ave} (ns)	PLQY (%)	Γ_{rad} (μs^{-1})	$\Gamma_{non\text{-}rad}$ (μs^{-1})
TCI	0.38	2.54	0.43	0.85	0.19	6.30	1.46	7.60	52.05	632.88
T-130-40 min	0.40	3.43	0.23	1.13	0.37	9.07	2.78	9.20	33.09	326.62
Sigma	0.42	3.65	0.20	0.87	0.38	10.59	2.61	11.00	42.15	341.00
S-130-30 min	0.43	4.79	0.23	1.15	0.34	1.41	3.15	13.10	41.59	275.87
S-130-40 min	0.42	5.64	0.26	1.76	0.33	13.50	4.11	16.60	40.39	202.92
S-130-60 min	0.43	5.66	0.30	1.71	0.27	15.94	3.73	13.00	34.85	233.24
S-130-180 min	0.41	4.04	0.27	1.00	0.32	11.80	2.52	10.40	41.27	355.56

By strictly controlling the quality of $Sn(Oct)_2$ used, my synthesis shows excellent batch-to-batch reproducibility (**Figure 2.2c**). I point out that the more highly luminescent NCs obtained using treated $Sn(Oct)_2$ do not show a significant difference in stability with respect to those using the untreated one (**Figure 2.2d**). I note that all of these NCs show similar absorption spectra and PL emissions peaking at 944 nm (**Figure 2.1b and Figure 2.4a**), which is consistent with my previous report. All diffraction peaks of NCs synthesized with treated $Sn(Oct)_2$ fit well with the standard diffraction patterns of the orthorhombic $CsSnI_3$ perovskite structure (ICSD code 69996) (**Figure 2.1c and Figure 2.4b**). However, in marked contrast, the average size and size uniformity of NCs are affected significantly by the tin(II) carboxylates used; increasing the treatment time of $Sn(Oct)_2$ leads to NCs with a larger average size and much poorer size uniformity, corresponding to 42.4 ± 3.9 nm for S-130-40 min, 44.5 ± 11.2 nm for S-130-180 min, and 39.3 ± 9.0 nm for T-130-40 min (**Figure 2.3 and Figure 2.4c**). These collected results unambiguously indicate that the exact molecular state of $Sn(Oct)_2$ can affect the nucleation and growth kinetics of $CsSnI_3$ NCs and their defects in the bulk or at the surface.

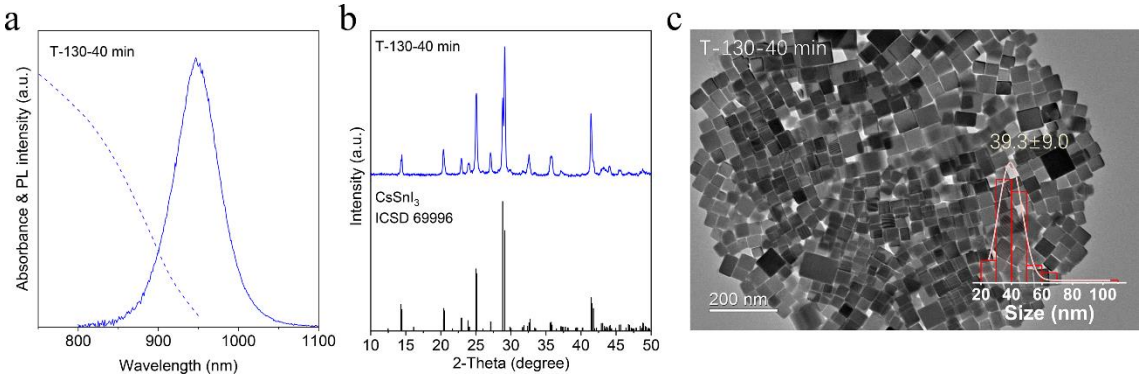

Figure 2.4 (a) Normalized PL (solid line) spectra and optical absorption (dashed line), (b) XRD pattern, and (c) TEM image of $CsSnI_3$ NCs synthesized using T-130-40 min $Sn(Oct)_2$. Insets in (c) show the histograms of edge lengths of corresponding $CsSnI_3$ NCs. A Gaussian distribution function was utilized to describe the size distribution of $CsSnI_3$ NCs.

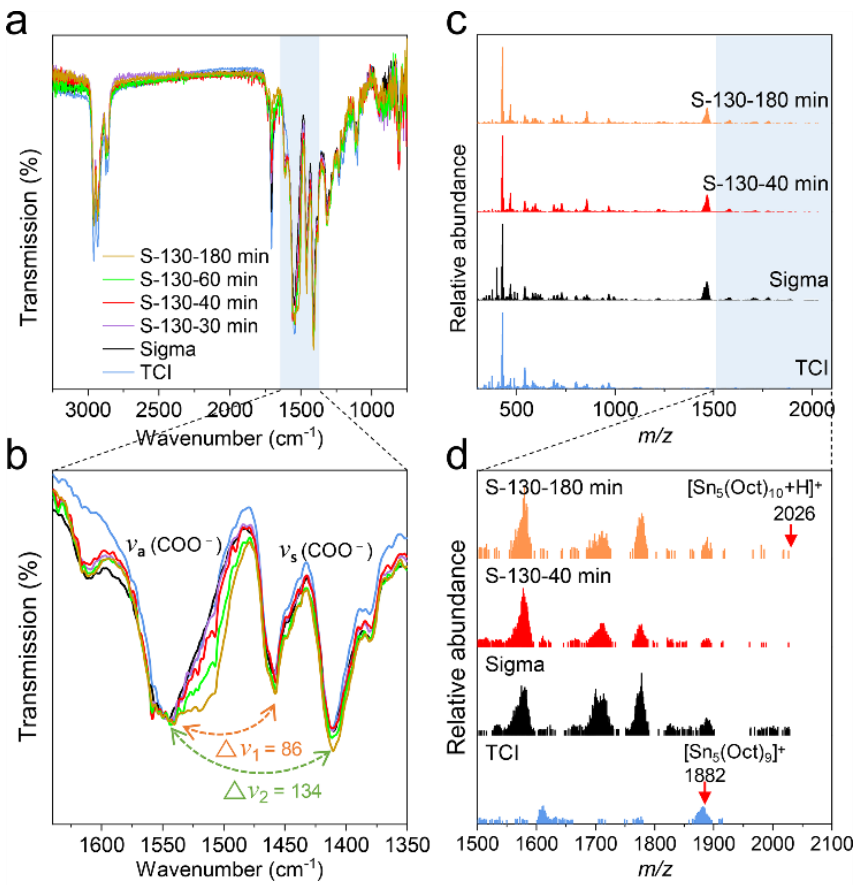

Figure 2.5 (a) FTIR spectra of $Sn(Oct)_2$ as received from Sigma and TCI and thermally treated. (b) Enlarged FTIR spectra corresponding to the COO^- vibrations. (c) ESI-MS spectra of different $Sn(Oct)_2$. (d) Enlarged ESI-MS spectra corresponding to the shadow region of (c).

To gain further insight into the molecular structure of $Sn(Oct)_2$ as received and thermally treated, I took Fourier-transform infrared spectroscopy (FTIR) (**Figure 2.5a**), considering that FTIR has been established as a powerful technique to distinguish the types of bonding of the carboxylate with the metal in metal 2-ethylhexanoates.[42] As shown in **Figure 2.5a**, broad vibrational bands at 2959, 2937, 2878, and 2866 cm^{-1} are observed in $Sn(Oct)_2$ as received, which are attributed to asymmetric and symmetric stretching vibrations of the alkyl $-CH_3$ and $-CH_2-$ groups of $Sn(Oct)_2$.[45,46] Additionally, the vibrational band at 1710 cm–1 originates from the C═O stretching vibration of the free carboxylic acid group of 2-ethylhexanoic acid as an impurity in $Sn(Oct)_2$ (**Figure 2.6**). The weak vibrational bands between 1310 and 1200 cm^{-1} are due to the vibrations of the $-CH_2-$ group.[45] Of particular interest are the strong vibrational band at 1545 cm^{-1} assigned to the asymmetric vibration of the COO^- group and those at 1459 and 1411 cm^{-1} assigned to the symmetric vibrations of the COO^- group; the low-energy symmetric vibrational bands are presumably split as a result of coupling of adjacent carboxylate vibrations. Previous work has revealed that the frequency difference between the asymmetric and symmetric stretching vibrations of the COO^- group in a metallic carboxylate, $\Delta v = v_a(COO^-) - v_s(COO^-)$, is intimately connected with the bonding state of the metal with COO^-; four coordination types between the metal and COO^-, i.e., monodentate, ionic, bridging, and chelating, with Δ_v decreasing in the order above, have been identified (**Table 2.3**).[44] I note that the Δ_v values are about 86 (Δv_1) and 134 (Δv_2) cm^{-1} for $Sn(Oct)_2$ as received and treated, indicating the coexistence of the chelating and bridging coordination geometries. A closer examination of the FTIR results leads us to find that thermally treated $Sn(Oct)_2$ displays broader vibrational bands with respect to those as received and that increasing the treatment time causes broadening of these bands. Given the presence of chelating and bridging coordination between tin and COO^-, I hypothesized that, akin to other types of metal 2-ethylhexanoates,[41-44] $Sn(Oct)_2$ could exist as oligomers and thermal treatment might affect their degree of polymerization.

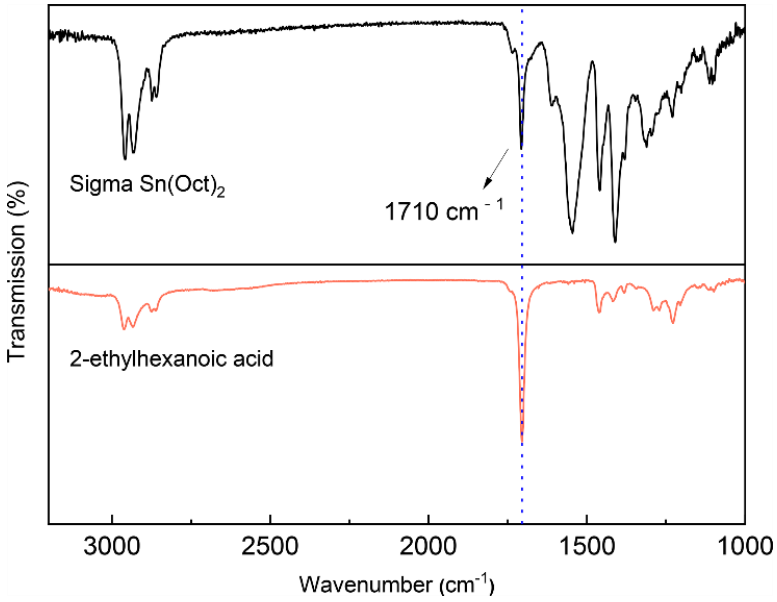

Figure 2.6 FTIR spectra of 2-ethylhexanoic acid and $Sn(Oct)_2$ as received from Sigma. The vibrational band at 1710 cm^{-1} in $Sn(Oct)_2$ FTIR spectrum matches perfectly with the 2-ethylhexanoic acid characteristic peak. The dotted blue line is drawn to guide the eye.

Table 2.3. Frequency difference of the main absorption bands in the FTIR spectra of metallic carboxylates, and the corresponding vibrational assignments.[42, 44]

	Monodentate	Ionic	Bridging	Chelating	Chelating & bridging
$\triangle v$ (cm^{-1})	200~300	164	140~170	40~80	/
Bonding modes	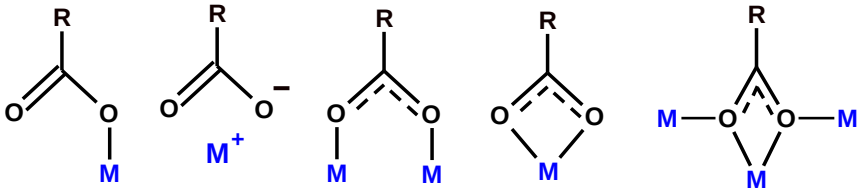				

The symbols in the table are read as follows: $\triangle v$, frequency difference between the asymmetric and symmetric stretching vibrations; M, metal atom; R, alkyl groups;

The reference value of $\triangle v$ is derived from metal acetate complexes.[42]

To test my hypothesis and to explore in more detail the molecular state of $Sn(Oct)_2$,

I conducted an ESI-MS measurement. As shown in **Figure 2.5c** and **d**, the ESI-MS spectrum of $Sn(Oct)_2$ from TCI shows a characteristic ion peak at m/z = 1882, which can be attributed to $[Sn_5(Oct)_9]^+$. Similarly, the ESI-MS spectra of $Sn(Oct)_2$ from Sigma, S-130-40 min, and S-130-180 min have a characteristic molecular ion peak at m/z = 2026, corresponding to $[Sn_5(Oct)_{10} + H]^+$. Additionally, the peaks at m/z = 429, 843, 1216, and 1477 can be assigned to $[Sn(Oct)_2 + Na]^+$, $[Sn_2(Oct)_4 + CH_3OH + H]^+$, $[Sn_3(Oct)_6 + H]^+$, and $[Sn_4(Oct)_7]^+$, respectively. I point out that the occurrence of $[Sn(Oct)_2 + Na]^+$ may be due to the presence of a sodium impurity in $Sn(Oct)_2$ (Table 1.1). I note that the fragment ions between m/z = 429 and 2026 in the ESI-MS spectra of $Sn(Oct)_2$ as received from Sigma and TCI and thermally treated show a significant difference (**Figure 2.5c** and **d**), suggesting that the percentages of each oligomer present in these tin(II) carboxylates are different. Taking the FTIR and ESI-MS results together, I infer that the chemical formula of these $Sn(Oct)_2$ oligomers can be shown as $Sn_x(Oct)_{2x}$ ($1 \leq x \leq 5$).

I next turned to using the NMR spectroscopy of ^{119}Sn to glean more information regarding the difference in the molecular structure of these tin sources. I find that $Sn(Oct)_2$ as received shows a chemical shift at -549.6 ppm, whereas S-130-40 min and S-130-180 min demonstrate shifts at -557.3 and -561.7 ppm, respectively (**Figure 2.7**). Such a notable thermal treatment-induced upfield shift is indicative of the increase of the coordination number of tin. That is, low-molecular-weight $Sn(Oct)_2$ oligomers tend to transform into higher-molecular-weight oligomers after the treatment. In the industrial synthesis of $Sn(Oct)_2$, thermal treatment is utilized as a means of regulating the syntheses and drying the product. My results, as shown above, provide direct experimental evidence of the presence of polymeric tin in $Sn(Oct)_2$ as received and thermally treated and show that their degree of polymerization can be readily tuned by the thermal treatment.

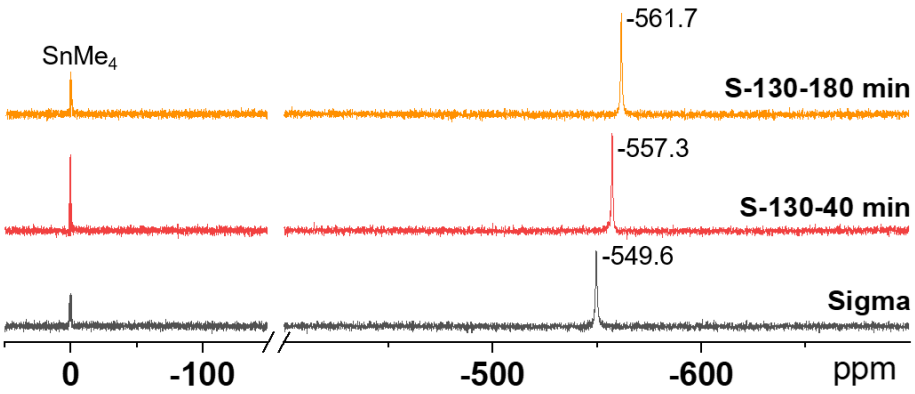

Figure 2.7 ^{119}Sn NMR spectra of $Sn(Oct)_2$ as received from Sigma, S-130-40 min and S-130-180 min. The spectrum was calibrated using tetramethyltin ($SnMe_4$) as the internal standard.

Since the tin(II) carboxylate source was first mixed with TMSI (**Figure 2.1a**), I then investigated what reaction takes place between them. I find that mixing $Sn(Oct)_2$ and TMSI quickly leads to the formation of some yellow precipitates (**Figure 2.8**), which are SnI2 as revealed by XRD (**Figure 2.9**). The molar ratio of $Sn(Oct)_2$ to TMSI is 4.33/3, and thus, TMSI tends to be consumed in the reaction. Subsequent introduction of TOP into the mixture leads to the dissolution of SnI_2 (**Figure 2.10**), as a consequence of the formation of a Lewis acid–base complex between TOP and SnI_2. A control experiment also indicated that TOP is a good coordination solvent for SnI_2 (**Figure 2.11**). These reactions can be described as follows.

$$Sn(Oct)_2+2TMSI \rightarrow SnI_2\downarrow+2TMS\text{-}Oct \quad (1)$$

$$TOP+SnI_2 \rightarrow TOP\cdots SnI_2 \quad (2)$$

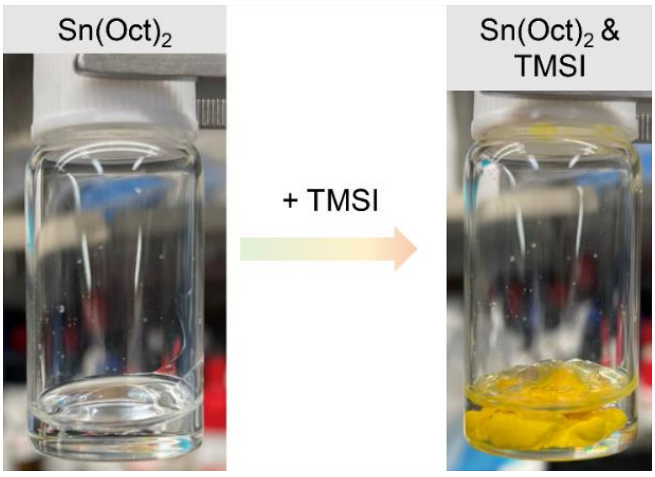

Figure 2.8 Photographs of the $Sn(Oct)_2$ as received from Sigma, and mixture of $Sn(Oct)_2$ with TMSI. Once $Sn(Oct)_2$ and TMSI were mixed, some yellow precipitates were formed quickly.

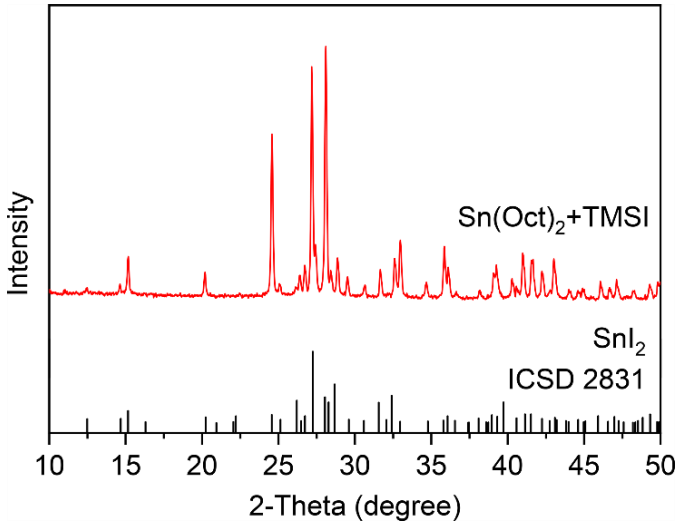

Figure 2.9 XRD pattern of yellow precipitates obtained by purification of the mixture of $Sn(Oct)_2$ with TMSI.

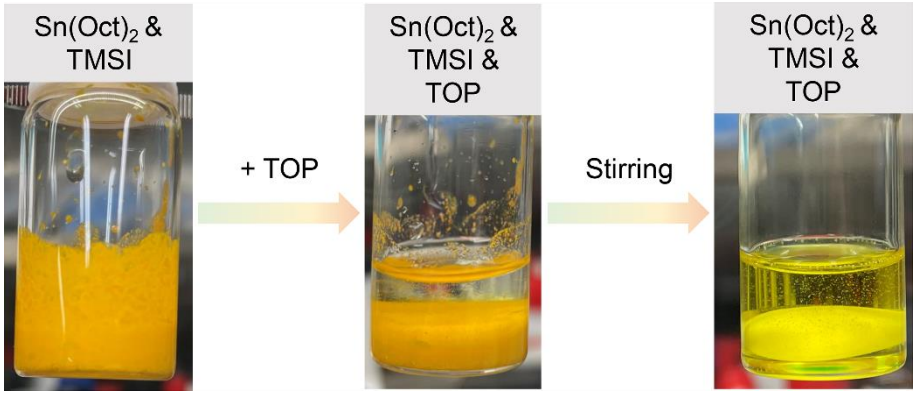

Figure 2.10 Photographs of the mixture of $Sn(Oct)_2$ with TMSI, and $Sn(Oct)_2$ with TMSI and TOP. When TOP was introduced into the mixture of $Sn(Oct)_2$ with TMSI , and the mixture was kept stirring, yellow precipitates were rapidly dissolved.

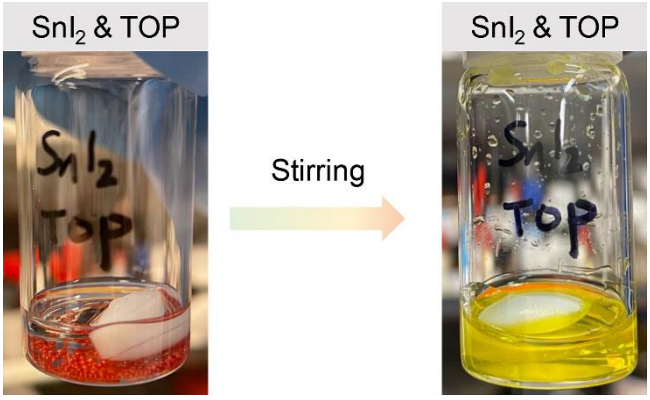

Figure 2.11 Photographs of the mixture of SnI_2 with TOP. After stirring for 60 min at room temperature, the SnI_2 microspheres were completely dissolved.

However, the chemical reactions in the TOP-Sn-I precursor could be not as straightforward as eqs 1 and 2 suggest because I find that $Sn(Oct)_2$ can also solubilize SnI_2 to form a clear yellow solution at room temperature even in the absence of TOP. Specifically, when I added 5%–10% equiv of TMSI into $Sn(Oct)_2$, SnI_2 formed first and then was dissolved over time (**Figure 2.12**); however, adding 15% equiv of TMSI led to a turbid solution due to undissolved SnI_2. These observations suggest that $Sn(Oct)_2$ can solubilize at least 5% of SnI_2, which is further confirmed by the fact that $Sn(Oct)_2$ can readily dissolve 5% of ultradry SnI_2 (**Figure 2.13**). I note that, compared with $Sn(Oct)_2$, the interaction of $Sn(Oct)_2$ with TMSI or SnI_2 results in a redshift of the optical absorption and a downfield shift of the Sn peak in ^{119}Sn NMR (**Figure 2.14a,b**), suggesting that the coordination environment of Sn is changed; in particular, the downfield shift observed in NMR signifies that a stronger electron-withdrawing group relative to COO^- interacts with tin. Interestingly, I further find ionic fragments, such as $[Sn_4I_2(Oct)_5]^+$ and $[Sn_5I(Oct)_8]^+$, to be present in the mixtures of TMSI with $Sn(Oct)_2$ as received, S-130-40 min, or S-130-180 min (**Figure 2.14c**). All of these results suggest that iodide ions replace the carboxylate group to form alkanoate iodides such as $Sn_xI_y(Oct)_{2x-y}$. This can be simply described by the following equation.

$$Sn_x(Oct)_{2x}+ySnI_2 \rightarrow Sn_xI_y(Oct)_{2x-y} \quad (3)$$

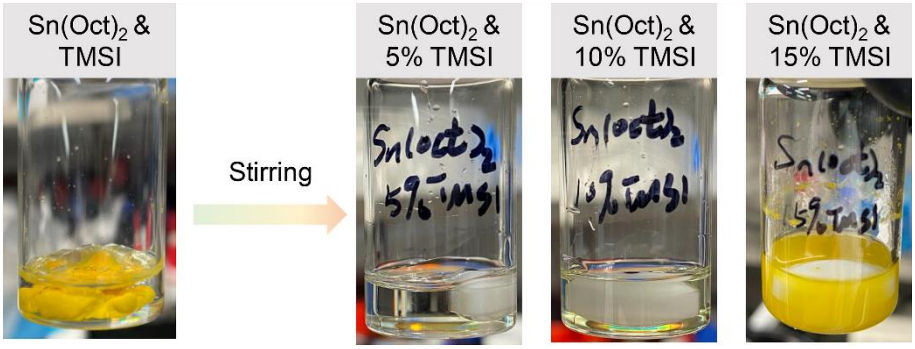

Figure 2.12 Photographs of the mixtures of $Sn(Oct)_2$ with 5%-15% equivalent of TMSI. After stirring for 30 min at room temperature, the yellow precipitates in the mixture containing 5%-10% of TMSI were completely dissolved.

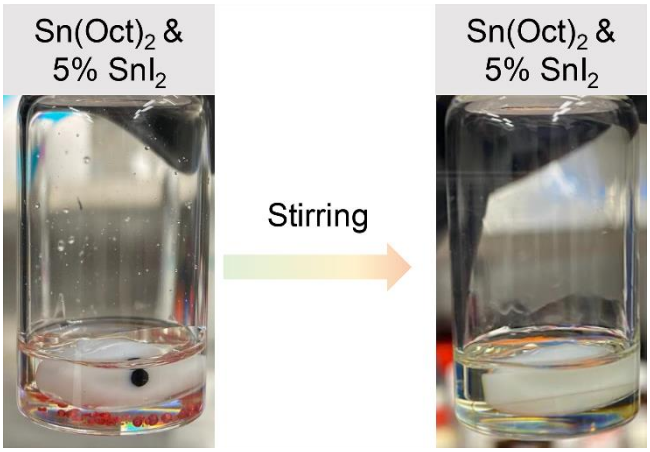

Figure 2.13 Photographs of the mixture of $Sn(Oct)_2$ with 5% equivalent of SnI_2. After stirring for 60 min at room temperature, the SnI_2 microspheres were completely dissolved.

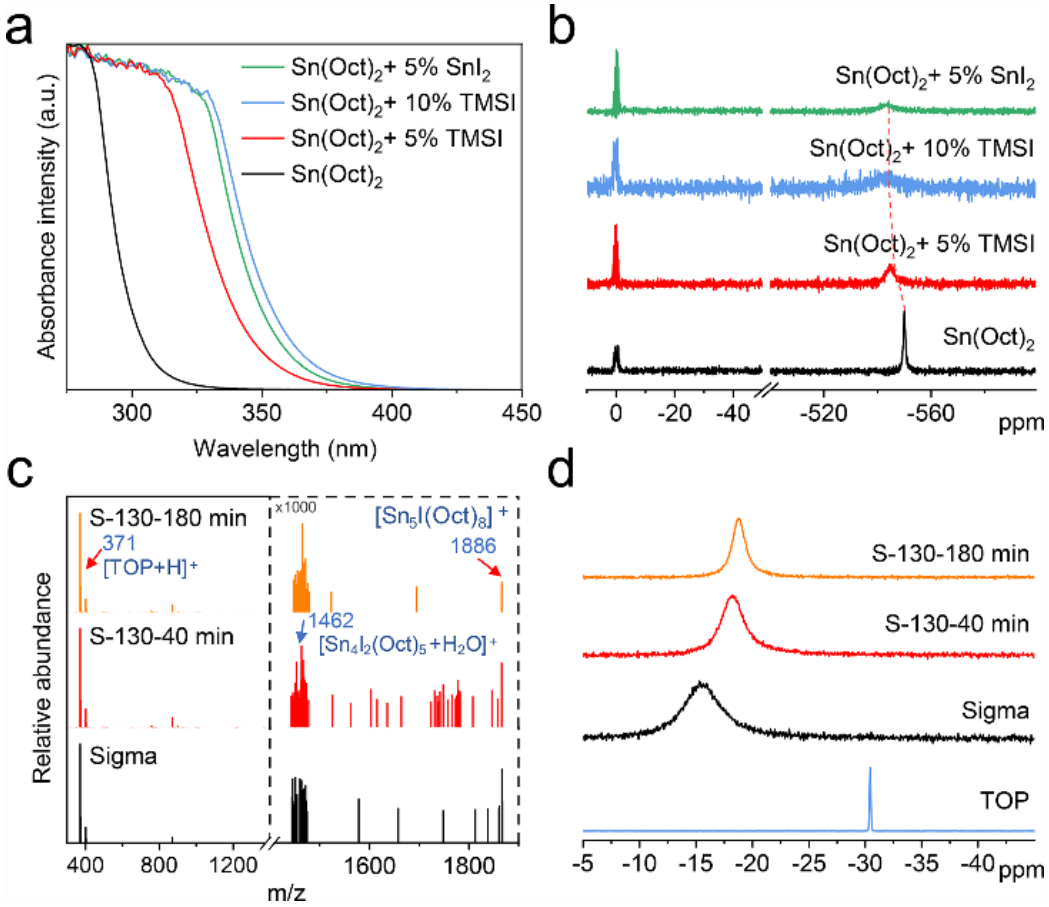

Figure 2.14 (a, b) Optical absorption (a) and ^{119}Sn NMR (b) of $Sn(Oct)_2$, the mixtures of $Sn(Oct)_2$ with TMSI or SnI_2. The dotted red line in (b) is drawn to guide the eye. (c) ESI-MS spectra of the mixtures of TOP and TMSI with $Sn(Oct)_2$ as received from Sigma, S-130-40 min or S-130-180 min. (d) ^{31}P NMR spectra of TOP and the TOP-Sn-I precursors prepared by mixing TOP and TMSI with $Sn(Oct)_2$ from Sigma, S-130-40 min or S-130-180 min.

Therefore, a more accurate description of the interaction of TOP with Sn and I should be TOP$\cdots Sn_xI_y(Oct)_{2x-y}$. To confirm such an interaction, I performed liquid ^{31}P NMR spectroscopy of TOP and the TOP-Sn-I precursors. As shown in **Figure 2.14d**, compared with pure TOP that has a chemical shift of -30.4 ppm, the chemical shift of the TOP-Sn-I precursor using $Sn(Oct)_2$ as received shows a significant downfield shift (-15.4 ppm; **Figure 2.14d**). This is attributed to the interaction between the Sn-I complex and TOP. Furthermore, I find that using thermally treated $Sn(Oct)_2$ as the tin source causes a notable upfield shift with respect to that using $Sn(Oct)_2$ as received, suggesting a weaker

interaction between TOP and the Sn-I complex. This weaker interaction can be explained by the increased degree of polymerization with treated $Sn(Oct)_2$, since more coordinated carboxyl groups could prevent the interaction of TOP with Sn. These results mean that the TOP-Sn-I precursor prepared by treated $Sn(Oct)_2$ should possess a stronger reactivity.

I subsequently designed control experiments to directly examine the difference in the reactivity of the TOP-Sn-I precursors prepared by different tin(II) carboxylates (see the experimental Section). Since the $CsSnI_3$ NCs are synthesized on subsecond time scales when using the hot-injection approach, this renders it extremely hard to discriminate the difference in the reactivity of the precursors owing to the difficulty in monitoring the experimental phenomena. To tackle this issue, I intentionally designed mild reaction conditions by lowering the reaction temperature. In brief, 1 mL of the Cs precursor stock solution is loaded into three types of TOP-Sn-I precursors (i.e., $Sn(Oct)_2$ as received from Sigma, S-130-40 min, and S-130-180 min) (**Figure 2.15**). I note that the mixtures corresponding to Sigma and S-130-40 min show a similar shallow yellow color at room temperature (RT), while that using S-130-180 min displays a dark yellow color, which is attributable to the difference in the degree of polymerization for different tin sources. Interestingly, thermal treatment at 60 °C for 1 min leads to the occurrence of a dark black color for the mixture using S-130-180 min, which is an indication of the start of assembly of Cs, Sn and I ions. A longer treatment at 60 °C can lead to the occurrence of black color for the precursor using S-130-40 min, followed by that using $Sn(Oct)_2$ as received from Sigma. These results clearly corroborate that a higher degree of polymerization of $Sn(Oct)_2$ results in stronger reactivity of the TOP-Sn-I precursor.

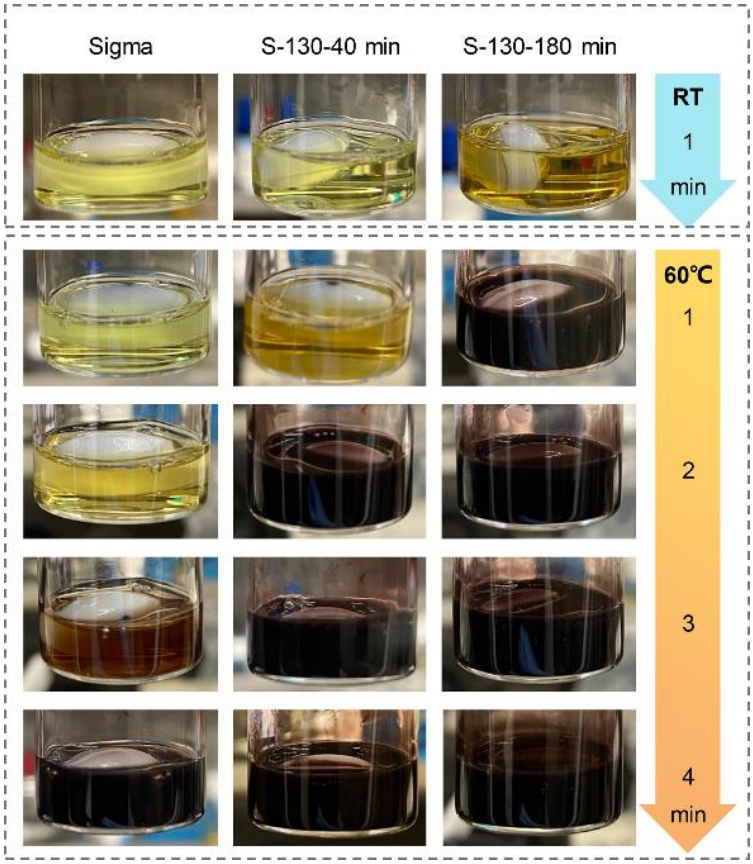

Figure 2.15 Photographs of the mixtures of the Cs precursor and TOP-Sn-I precursors made by mixing TMSI with $Sn(Oct)_2$ as received from Sigma, S-130-40 min, or S-130-180 min. The mixtures were treated at RT and 60 °C for different durations.

All of the aforementioned experimental results indicate that the degree of polymerization of tin(II) carboxylates greatly influences the reactivity of the TOP-Sn-I precursor, which further affects the nucleation and growth kinetics of $CsSnI_3$ NCs. I thus propose the following plausible mechanism to explain the formation of $CsSnI_3$ NCs (**Figure 2.16**). Considering the feeding ratio used for My synthesis (i.e., the Cs/Sn/I ratio is 0.35:4.33:3) and experimental facts as revealed, I establish that highly reactive polymeric $Sn_xI_y(Oct)_{2x-y}$ complexes exist in the TOP-Sn-I precursor, whose reactivity is connected with the tin(II) carboxylate precursor used. When the TOP-Sn-I precursor is injected into the Cs precursor solution, the Cs precursor reacts rapidly with the highly reactive $Sn_xI_y(Oct)_{2x-y}$ complex, leading to burst nucleation. I surmise that one $Sn_xI_y(Oct)_{2x-y}$ oligomer could supply at least one $[SnI_3]^-$ that can be used for the

construction of the SnI6 octahedra (bottom of **Figure 2.16**). As a consequence, the ratio of each $Sn_xI_y(Oct)_{2x-y}$ in the precursor can impact the nucleation and growth of NCs, leading to a change in their size, size uniformity, and photophysical properties. This is different from the case where the TOP···SnI_2 complex acts as the tin and iodide sources because of its poorer capability in supplying the tin iodide species with respect to $Sn_xI_y(Oct)_{2x-y}$ (the upper part of **Figure 2.16**). Since the formation of structural defects is sensitive to the chemical potentials of each constituent element, any subtle variation in the reactivity of the precursor can affect the density of defects and thus the PLQYs of the resultant NCs (**Figure 2.1**). I find that the tin(II) carboxylate with moderate reactivity leads to NCs with the best size uniformity and PLQY, and that a higher reactivity results in larger NCs and poor size uniformity and PLQY. This signifies the importance of the reactivities of the precursors in governing the properties of $CsSnI_3$ NCs.

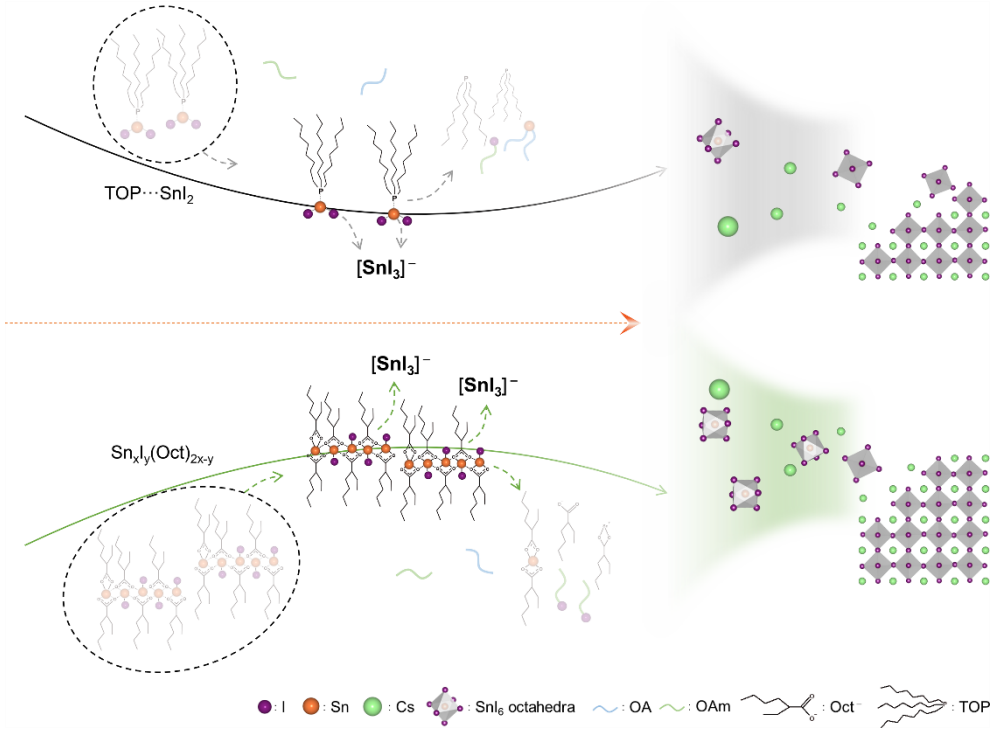

Figure 2.16 Schematic of the proposed formation mechanism of $CsSnI_3$ NCs. The upper part represents the case where the TOP···SnI_2 complex acts as the tin and iodide sources, while the bottom is my case where the $Sn_xI_y(Oct)_{2x-y}$ complex acts as the tin and iodide sources. It is worth noting that the iodine atoms occupy the vertices of regular corner-sharing octahedra, which means that the [SnI_6]

octahedron consists of only one tin atom and three iodine atoms. The $Sn_xI_y(Oct)_{2x-y}$ complex can readily provide more $[SnI_3]^-$ for the assembly of $CsSnI_3$ NCs, compared with the same number of the TOP···SnI_2 complex.

2.4 Conclusion

To conclude, I elucidated the precursor chemistry in the synthesis of colloidal $CsSnI_3$ NCs. I showed how tin(II) carboxylates affect the reactivity of the precursors using a variety of techniques, including FTIR, ESI-MS, and NMR. I identified that the intermediate complexes, alkanoate iodides ($Sn_xI_y(Oct)_{2x-y}$), play a key role in governing the reactivity of the tin iodide precursor, which leads to variations in the size, size uniformity, and PLQY of $CsSnI_3$ NCs. My findings highlight the importance of selecting the precursors and examining their evolution in detail in the synthesis of tin-based NCs, which is not only beneficial for the attainment of high-quality NCs in a controlled manner but also for developing more rational synthetic protocols for NCs with better size uniformity and optical properties. In particular, I believe that judicious design of the tin iodide precursor with a desired reactivity may lead to the attainment of highly luminescent tin halide perovskite NCs. Given similar defect formation mechanisms in tin-based NCs and polycrystalline films,47 I envisage that these insights might also offer guidelines for fabricating high-quality polycrystalline films that can be used for optoelectronic devices such as LEDs and photovoltaics.

Reference

(1) Dey, A.; Ye, J.; De, A.; Debroye, E.; Ha, S. K.; Bladt, E.; Kshirsagar, A. S.; Wang, Z.; Yin, J.; Wang, Y.; et al. State of the Art and Prospects for Halide Perovskite Nanocrystals. *ACS Nano* **2021**, 15, 10775-10981.

(2) Quan, L. N.; Rand, B. P.; Friend, R. H.; Mhaisalkar, S. G.; Lee, T. W.; Sargent, E. H. Perovskites for Next-Generation Optical Sources. *Chem. Rev.* **2019**, 119, 7444-7477.

(3) Akkerman, Q. A.; Raino, G.; Kovalenko, M. V.; Manna, L. Genesis, Challenges and Opportunities for Colloidal Lead Halide Perovskite Nanocrystals. *Nat. Mater.* **2018**, 17, 394-405.

(4) Chen, Q.; Wu, J.; Ou, X.; Huang, B.; Almutlaq, J.; Zhumekenov, A. A.; Guan, X.; Han, S.; Liang, L.; Yi, Z.; et al. All-inorganic Perovskite Nanocrystal Scintillators. *Nature* **2018**, 561, 88-93.

(5) Akkerman, Q. A.; Gandini, M.; Di Stasio, F.; Rastogi, P.; Palazon, F.; Bertoni, G.; Ball, J. M.; Prato, M.; Petrozza, A.; Manna, L. Strongly Emissive Perovskite Nanocrystal Inks for High-Voltage Solar Cells. *Nat. Energy* **2017**, 2, 16194.

(6) Hao, M.; Bai, Y.; Zeiske, S.; Ren, L.; Liu, J.; Yuan, Y.; Zarrabi, N.; Cheng, N.; Ghasemi, M.; Chen, P.; et al. Ligand-Assisted Cation-Exchange Engineering for High-Efficiency Colloidal $Cs_{1-x}FA_xPbI_3$ Quantum Dot Solar Cells with Reduced Phase Segregation. *Nat. Energy* **2020**, 5, 79-88.

(7) Huang, H.; Bodnarchuk, M. I.; Kershaw, S. V.; Kovalenko, M. V.; Rogach, A. L. Lead Halide Perovskite Nanocrystals in the Research Spotlight: Stability and Defect Tolerance. *ACS Energy Lett.* **2017**, 2, 2071-2083.

(8) Protesescu, L.; Yakunin, S.; Bodnarchuk, M. I.; Krieg, F.; Caputo, R.; Hendon, C. H.; Yang, R. X.; Walsh, A.; Kovalenko, M. V. Nanocrystals of Cesium Lead Halide Perovskites ($CsPbX_3$, X= Cl, Br, and I): Novel Optoelectronic Materials Showing Bright Emission with Wide Color Gamut. *Nano lett.* **2015**, 15, 3692-3696.

(9) Wang, Y.; Li, X.; Song, J.; Xiao, L.; Zeng, H.; Sun, H. All-Inorganic Colloidal Perovskite Quantum Dots: A New Class of Lasing Materials with Favorable

Characteristics. *Adv. Mater.* **2015**, 27, 7101-7108.

(10) Zheng, X.; Hou, Y.; Sun, H. T.; Mohammed, O. F.; Sargent, E. H.; Bakr, O. M. Reducing Defects in Halide Perovskite Nanocrystals for Light-Emitting Applications. *J. Phys. Chem. Lett.* **2019**, 10, 2629-2640.

(11) Ding, N.; Wu, Y.; Xu, W.; Lyu, J.; Wang, Y.; Zi, L.; Shao, L.; Sun, R.; Wang, N.; Liu, S.; et al. A Novel Approach for Designing Efficient Broadband Photodetectors Expanding from Deep Ultraviolet to Near Infrared. *Light: Sci. & Appl.* **2022**, 11, 91.

(12) Zhang, F.; Zhong, H.; Chen, C.; Wu, X.-g.; Hu, X.; Huang, H.; Han, J.; Zou, B.; Dong, Y. Brightly Luminescent and Color-Tunable Colloidal $CH_3NH_3PbX_3$ (X = Br, I, Cl) Quantum Dots: Potential Alternatives for Display Technology. *ACS Nano* **2015**, 9, 4533-4542.

(13) Yong, Z. J.; Guo, S. Q.; Ma, J. P.; Zhang, J. Y.; Li, Z. Y.; Chen, Y. M.; Zhang, B. B.; Zhou, Y.; Shu, J.; Gu, J. L.; et al. Doping-Enhanced Short-Range Order of Perovskite Nanocrystals for Near-Unity Violet Luminescence Quantum Yield. *J. Am. Chem. Soc.* **2018**, 140, 9942-9951.

(14) Mondal, N.; De, A.; Samanta, A. Achieving Near-Unity Photoluminescence Efficiency for Blue-Violet-Emitting Perovskite Nanocrystals. *ACS Energy Lett.* **2018**, 4, 32-39.

(15) Dutta, A.; Behera, R. K.; Pal, P.; Baitalik, S.; Pradhan, N. Near-Unity Photoluminescence Quantum Efficiency for All $CsPbX_3$ (X= Cl, Br and I) Perovskite Nanocrystals: A Generic Synthesis Approach. *Angew. Chem., Int. Ed.* **2019**, 58, 5552-5556.

(16) Imran, M.; Caligiuri, V.; Wang, M.; Goldoni, L.; Prato, M.; Krahne, R.; De Trizio, L.; Manna, L. Benzoyl Halides as Alternative Precursors for the Colloidal Synthesis of Lead-Based Halide Perovskite Nanocrystals. *J. Am. Chem. Soc.* **2018**, 140, 2656-2664.

(17) Li, Z.; Kong, L.; Huang, S.; Li, L. Highly Luminescent and Ultrastable $CsPbBr_3$ Perovskite Quantum Dots Incorporated into a Silica/Alumina Monolith. *Angew. Chem.,*

Int. Ed. **2017**, 56, 8134-8138.

(18) Liu, F.; Zhang, Y.; Ding, C.; Kobayashi, S.; Izuishi, T.; Nakazawa, N.; Toyoda, T.; Ohta, T.; Hayase, S.; Minemoto, T.; et al. Highly Luminescent Phase-Stable $CsPbI_3$ Perovskite Quantum Dots Achieving Near 100% Absolute Photoluminescence Quantum Yield. *ACS Nano* **2017**, 11, 10373-10383.

(19) Pradhan, N. Tips and Twists in Making High Photoluminescence Quantum Yield Perovskite Nanocrystals. *ACS Energy Lett.* **2019**, 4, 1634-1638.

(20) Zhang, B. B.; Yuan, S.; Ma, J. P.; Zhou, Y.; Hou, J.; Chen, X.; Zheng, W.; Shen, H.; Wang, X. C.; Sun, B.; et al. General Mild Reaction Creates Highly Luminescent Organic-Ligand-Lacking Halide Perovskite Nanocrystals for Efficient Light-Emitting Diodes. *J. Am. Chem. Soc.* **2019**, 141, 15423-15432.

(21) Tong, Y.; Bladt, E.; Aygüler, M. F.; Manzi, A.; Milowska, K. Z.; Hintermayr, V. A.; Docampo, P.; Bals, S.; Urban, A. S.; Polavarapu, L.; et al. Highly Luminescent Cesium Lead Halide Perovskite Nanocrystals with Tunable Composition and Thickness by Ultrasonication. *Angew. Chem., Int. Ed.* **2016**, 55, 13887-13892.

(22) Zhou, Y.; Chen, J.; Bakr, O. M.; Sun, H.-T. Metal-Doped Lead Halide Perovskites: Synthesis, Properties, and Optoelectronic Applications. *Chem. Mater.* **2018**, 30, 6589-6613.

(23) Chen, Y.; Liu, Y.; Hong, M. Cation-Doping Matters in Caesium Lead Halide Perovskite Nanocrystals: from Physicochemical Fundamentals to Optoelectronic Applications. *Nanoscale* **2020**, 12, 12228-12248.

(24) Cao, Y.; Wang, N.; Tian, H.; Guo, J.; Wei, Y.; Chen, H.; Miao, Y.; Zou, W.; Pan, K.; He, Y.; et al. Perovskite Light-Emitting Diodes Based on Spontaneously Formed Submicrometre-Scale Structures. *Nature* **2018**, 562, 249-253.

(25) Chiba, T.; Hayashi, Y.; Ebe, H.; Hoshi, K.; Sato, J.; Sato, S.; Pu, Y. J.; Ohisa, S.; Kido, J. Anion-Exchange Red Perovskite Quantum Dots with Ammonium Iodine Salts for Highly Efficient Light-Emitting Devices. *Nat. Photonics* **2018**, 12, 681-687..

(26) Dong, Y.; Wang, Y. K.; Yuan, F.; Johnston, A.; Liu, Y.; Ma, D.; Choi, M. J.;

Chen, B.; Chekini, M.; Baek, S. W.; et al. Bipolar-Shell Resurfacing for Blue LEDs Based on Strongly Confined Perovskite Quantum dots. *Nat. Nanotechnol.* **2020**, 15, 668-674.

(27) Hu, T.; Li, D.; Shan, Q.; Dong, Y.; Xiang, H.; Choy, W. C. H.; Zeng, H. Defect Behaviors in Perovskite Light-Emitting Diodes. *ACS Mater. Lett.* **2021**, 3, 1702-1728.

(28) Liu, M.; Wan, Q.; Wang, H.; Carulli, F.; Sun, X.; Zheng, W.; Kong, L.; Zhang, Q.; Zhang, C.; Zhang, Q.; et al. Suppression of Temperature Quenching in Perovskite Nanocrystals for Efficient and Thermally Stable Light-Emitting Diodes. *Nat. Photonics* **2021**, 15, 379-385.

(29) Infante, I.; Manna, L. Are There Good Alternatives to Lead Halide Perovskite Nanocrystals? *Nano Lett.* **2020**, 21, 6-9.

(30) Fan, Q.; Biesold-McGee, G. V.; Ma, J.; Xu, Q.; Pan, S.; Peng, J.; Lin, Z. Lead-Free Halide Perovskite Nanocrystals: Crystal Structures, Synthesis, Stabilities, and Optical Properties. *Angew. Chem., Int. Ed.* **2020**, 59, 1030-1046.

(31) Chen, J.-K.; Zhang, B.-B.; Liu, Q.; Shirahata, N.; Mohammed, O. F.; Bakr, O. M.; Sun, H.-T. Advances and Challenges in Tin Halide Perovskite Nanocrystals. *ACS Mater. Lett.* **2021**, 3, 1541-1557.

(32) Chung, I.; Song, J. H.; Im, J.; Androulakis, J.; Malliakas, C. D.; Li, H.; Freeman, A. J.; Kenney, J. T.; Kanatzidis, M. G. $CsSnI_3$: Semiconductor or Metal? High Electrical Conductivity and Strong Near-Infrared Photoluminescence from a Single Material. High Hole Mobility and Phase-Transitions. *J. Am. Chem. Soc.* **2012**, 134, 8579-8587.

(33) Jellicoe, T. C.; Richter, J. M.; Glass, H. F.; Tabachnyk, M.; Brady, R.; Dutton, S. E.; Rao, A.; Friend, R. H.; Credgington, D.; Greenham, N. C.; et al. Synthesis and Optical Properties of Lead-Free Cesium Tin Halide Perovskite Nanocrystals. *J. Am. Chem. Soc* .**2016**, 138, 2941-2944.

(34) Wong, A. B.; Bekenstein, Y.; Kang, J.; Kley, C. S.; Kim, D.; Gibson, N. A.; Zhang, D.; Yu, Y.; Leone, S. R.; Wang, L. W.; et al. Strongly Quantum Confined Colloidal Cesium Tin Iodide Perovskite Nanoplates: Lessons for Reducing Defect Density and Improving Stability. *Nano Lett.* **2018**, 18, 2060-2066.

(35) Kang, C.; Rao, H.; Fang, Y.; Zeng, J.; Pan, Z.; Zhong, X. Antioxidative Stannous Oxalate Derived Lead-Free Stable $CsSnX_3$ (X=Cl, Br, and I) Perovskite Nanocrystals. *Angew. Chem., Int. Ed.* **2020**, 60, 660-665.

(36) Liu, Q.; Yin, J.; Zhang, B. B.; Chen, J. K.; Zhou, Y.; Zhang, L. M.; Wang, L. M.; Zhao, Q.; Hou, J.; Shu, J.; et al. Theory-Guided Synthesis of Highly Luminescent Colloidal Cesium Tin Halide Perovskite Nanocrystals. *J. Am. Chem. Soc.* **2021**, 143, 5470-5480.

(37) Dai, L.; Deng, Z.; Auras, F.; Goodwin, H.; Zhang, Z.; Walmsley, J. C.; Bristowe, P. D.; Deschler, F.; Greenham, N. C. Slow Carrier Relaxation in Tin-Based Perovskite Nanocrystals. *Nat. Photonics* **2021**, 15, 696-702.

(38) Dirin, D. N.; Vivani, A.; Zacharias, M.; Sekh, T. V.; Cherniukh, I.; Yakunin, S.; Bertolotti, F.; Aebli, M.; Schaller, R. D.; Wieczorek, A.; et al. Intrinsic Formamidinium Tin Iodide Nanocrystals by Suppressing the Sn(IV) Impurities. *Nano Lett.* **2023**, 23, 1914-1923.

(39) Wang, L. M.; Chen, J. K.; Zhang, B. B.; Liu, Q.; Zhou, Y.; Shu, J.; Wang, Z.; Shirahata, N.; Song, B.; Mohammed, O. F.; et al. Phosphatidylcholine-Mediated Regulation of Growth Kinetics for Colloidal Synthesis of Cesium Tin Halide Nanocrystals. *Nanoscale* **2021**, 13, 16726-16733.

(40) Gahlot, K.; de Graaf, S.; Duim, H.; Nedelcu, G.; Koushki, R. M.; Ahmadi, M.; Gavhane, D.; Lasorsa, A.; De Luca, O.; Rudolf, P.; et al. Structural Dynamics and Tunability for Colloidal Tin Halide Perovskite Nanostructures. *Adv. Mater.* **2022**, 34, e2201353.

(41) Deacon, G. B.; Phillips, R. J. Relationships Between the Carbon-Oxygen Stretching Frequencies of Carboxylato Complexes and the Type of Carboxylate Coordination. *Coord. Chem. Rev.* **1980**, 33, 227-250.

(42) Hill, R. H.; Blair, S. L. An Inorganic Approach to Photolithography: The Photolithographic Deposition of Dielectric Metal Oxide Films. *ACS Symp. Ser.* **1998**, 706, 53-66.

(43) Andronic, L. S.; Hill, R. H. The Mechanism of the Photochemical Metal Organic Deposition of Lead Oxide Films from Thin Films of Lead (II) 2-ethylhexanoate. *J. Photochem. Photobiol., A* **2002**, 152, 259-265.

(44) Mishra, S.; Daniele, S.; Hubert-Pfalzgraf, L. G. Metal 2-ethylhexanoates and Related Compounds as Useful Precursors in Materials Science. *Chem. Soc. Rev.* **2007**, 36, 1770-1787.

(45) Park, H.-H.; Law, W. L.; Zhang, X.; Hwang, S.-Y.; Jung, S. H.; Shin, H.-B.; Kang, H. K.; Park, H.-H.; Hill, R. H.; Ko, C. K. Facile Size-Tunable Fabrication of Functional Tin Dioxide Nanostructures by Multiple Size Reduction Lithography. *ACS Appl. Mater. Interfaces* **2012**, 4, 2507-2514.

(46) Li, H.; Pokhrel, S.; Schowalter, M.; Rosenauer, A.; Kiefer, J.; Mädler, L. The Gas-Phase Formation of Tin Dioxide Nanoparticles in Single Droplet Combustion and Flame Spray Pyrolysis. *Combust. flame* **2020**, 215, 389-400.

(47) Jiang, X.; Li, H.; Zhou, Q.; Wei, Q.; Wei, M.; Jiang, L.; Wang, Z.; Peng, Z.; Wang, F.; Zang, Z.; et al. One-Step Synthesis of $SnI_2.(DMSO)_x$ Adducts for High-Performance Tin Perovskite Solar Cells. *J. Am. Chem. Soc.* **2021**, 143, 10970-10976.

Chapter 3 Efficient Luminescence of Size-Tunable $CsSnX_3$ Perovskite Nanocrystals Synthesized via Phase Transition of CsX Nanocrystals

3.1 Introduction

In recent years, metal halide perovskite nanocrystals (NCs), with their outstanding optoelectronic performance, tunability, and stability, have become a focal point in the field of energy conversion and lighting.[1-11] Advances in the synthesis of halide perovskite NCs and crucial methods such as surface defect passivation have led to nearly consistent photoluminescence quantum yields (PLQY) in the visible and near-infrared regions.[1, 8, 12-20] However, environmental and health concerns associated with lead (Pb) have prompted a shift in attention towards lead-free halide PNCs.[21-23]

Tin (Sn) has gained attention as a potential alternative due to its lower toxicity and similar perovskite properties to Pb.[21-24] Nevertheless, the synthesis of colloidal $CsSnX_3$ (X = Cl, Br, I) perovskite NCs with high luminescent performance has been a formidable challenge. Previous studies indicated that $CsSnX_3$ NCs with broad emission spectra (ranging from green ~500 nm to near-infrared ~950 nm) could be synthesized by injecting SnX_2 salts dissolved in trioctylphosphine (TOP) into a mixture of Cs_2CO_3 and oleic acid (OA).[21] However, all obtained $CsSnX_3$ NCs exhibited extremely low PLQY (<0.2%), suggesting a high density of trap states. Another hot injection method utilizing trioctylamine, octylamine, and octanoic acid as capping agents and SnX_2 and Cs_2CO_3 as elemental sources synthesized 2D $CsSnI_3$ nanoplates.[25] Unfortunately, these nanoplates had a high density of tin vacancies (V_{Sn}), resulting in a PLQY of much less than 1%.

In addition to the hot-injection method, Ligand-Assisted Reprecipitation (LARP) and Chemical Vapor Deposition (CVD) have also been employed for the synthesis of tin halide perovskite NCs.[26, 27] For instance, Chen et al. successfully synthesized PEA_2SnBr_4 and PEA_2SnI_4 nanosheets through the LARP process, achieving a high PLQY of up to 6.4%.[27] However, there have been no reports, to date, on obtaining regularly shaped and uniformly structured $CsSnX_3$ nanocubes through this synthesis method. The CVD method

requires higher temperatures, longer reaction times, and precise control over gas flow and vapor pressure. Typically, this process can achieve the epitaxial growth of low-dimensional perovskite NCs, such as nanowires and nanosheets.[28-30] In 2019, Han et al. synthesized $CsSnCl_3$, $CsSnBr_3$, $CsSnI_3$, and $CsSnBrI_2$ nanowires (NWs) through an improved CVD process.[31] The unique morphology of these $CsSnX_3$ NWs makes them attractive for applications in optoelectronic detectors. However, the article did not provide information on the photoluminescence efficiency of these $CsSnX_3$ NWs.

As research progresses, a deeper understanding of the synthesis mechanism of $CsSnX_3$ perovskite NCs has emerged. Some studies emphasize the necessity of excess tin sources to reduce Sn vacancies in $CsSnX_3$ perovskite NCs, achieving a high PLQY of up to 18.4% for $CsSnI_3$ NCs.[32] However, the luminescent efficiency of the obtained NCs needs further improvement. Therefore, there is an urgent need to develop a more suitable method for synthesizing highly luminescent $CsSnX_3$ NCs.

In this study, I successfully synthesized size-tunable, uniformly shaped, and highly luminescent $CsSnI_3$ NCs using the CsX NCs phase transformation method. The synthesis process of CsX NCs is relatively simple, providing a robust foundation for further optimization and application of such NCs. CsX NCs of different sizes can be readily transformed into $CsSnX_3$ NCs, achieving size-tunable and uniformly shaped $CsSnX_3$ NCs. Through high-resolution transmission electron microscopy (HRTEM) and X-ray diffraction (XRD), I observed that the transformation process from CsX NCs to $CsSnX_3$ NCs is gradual, completing within 10 minutes. The discovery of intermediate products in the transformation process confirms the ongoing deformation, which may be similar to the process of CsX transforming into $CsPbX_3$ perovskite,[33] involving cation exchange where Sn ions gradually replace Cs ions in the CsX lattice sites. After the transformation is complete, further prolonged aging reduces the defect density in the $CsSnX_3$ NCs, leading to a gradual increase in PLQY. The obtained $CsSnI_3$ NCs exhibited a PLQY exceeding 30%, which is the highest efficiency reported so far. However, $CsSnBr_3$ NCs exhibited luminescence efficiencies near 0, indicating that the synthesis of $CsSnX_3$ NCs

rich in Br remains a challenge. In conclusion, my research lays a crucial foundation for the development of more efficient and stable all-inorganic perovskite NCs for applications in the field of optoelectronics.

3.2 Experimental Section

3.2.1 Chemicals and experimental

Chemicals

Cesium carbonate (Cs_2CO_3, Sigma, 99.995%), tin(II) iodide (SnI_2, Sigma, 99.999%), tin(II) bromide ($SnBr_2$, Sigma, 99.99 %), Zinc iodide (ZnI_2, Wako, 99.5%), Zinc bromide ($ZnBr_2$, Wako, 99.9 %), Iodine (I_2, Wako, 99%), Oleylammonium Iodide (OAmI, Xi'an Yuri, 98%), 1-octadecene (ODE, Alfa, 90%), oleylamine (OAm, Thermo Fisher, 80–90%), oleic acid (OA, Sigma, 90%), tri-n-octylphosphine (TOP, Thermo Fisher, 90%), Toluene (Wako, 99.5%), n-hexane (Wako, ≥96.0%), were used without purification unless otherwise noted.

Preparation of the Cs precursor.

In an Ar-filled glovebox, Cs_2CO_3 (0.6436 g, 0.988 mmol) and OA (10 mL) were mixed in a 20 mL glass bottle. Subsequently, the mixture was heated at 120 °C and stirred at 400 rpm for 120 minutes (min) to obtain a colorless Cs precursor solution. Afterwards, it was used for the synthesis of CsX NCs.

Preparation of the ZnI_2 precursor.

In an Ar-filled glovebox, ZnI_2 (0.0639 g, 0.2 mmol), OA (1 mL), OAm (1 mL), and OED (2 mL) were mixed in a 20 mL glass bottle. In this case, ODE needs to be vacuum dried at 120°C for 2 hours before use. Subsequently, the mixture was heated at 120 °C and stirred at 400 rpm for 30 min to obtain a colorless ZnI_2 precursor solution. Afterwards, it was used for the synthesis of CsI NCs.

Preparation of the I_2 precursor.

The synthesis of I_2 precursors was similar to that of ZnI_2 precursor, where the ZnI_2 was replaced with I_2 (0.0508 g, 0.2 mmol).

Preparation of the $ZnBr_2$ precursor.

The synthesis of $ZnBr_2$ precursors were similar to that of ZnI_2 precursor, where the ZnI_2 was replaced with $ZnBr_2$ (0.45 g, 0.2 mmol). Subsequently, $ZnBr_2$ precursors was used to synthesize CsBr NCs.

Synthesis of CsI NCs.

In a topical synthesis, ZnI_2 precursor (or other I_2 precursor) was heated at 60 °C (Different sizes of CsI NCs can be obtained by varying the temperature) and stirred at 400 rpm for 20 min on the heating plate, and then 0.55 mL amount of Cs precursor was swiftly injected into the ZnI_2 precursor. After 5 min of reaction, the reaction mixture was cooled to room temperature using a water bath. To collect the CsI NCs, the solution was then centrifuged at 12000 rpm for 5 min. After centrifugation, the supernatant was discarded and the NCs were redispersed in 4 mL toluene.

Synthesis of CsBr NCs.

The synthesis of CsBr NCs was similar to that of CsI NCs, where the ZnI_2 precursor was replaced with $ZnBr_2$ precursor.

Preparation of the SnI_2-TOP precursor.

In an Ar-filled glovebox, SnI_2 (0.1863g, 0.5 mmol) and TOP (0.335 mL) were mixed in a 9 mL glass bottle. Subsequently, the mixture was heated at 120 °C and stirred at 300 rpm for 15 min to obtain a dark yellow clear solution. Subsequently, the obtained solution was cooled to room temperature and then injected with 0.665 mL of toluene and uniformly mixed at room temperature. Afterwards, the SnI_2-TOP precursor (~0.5 mmol/mL) was used for the synthesis of $CsSnI_3$ NCs.

Preparation of the $SnBr_2$-TOP precursor.

The synthesis of $SnBr_2$-TOP precursors was similar to that of SnI_2-TOP precursor, where the SnI_2 was replaced with $SnBr_2$ (0.1395 g, 0.5 mmol).

Synthesis of $CsSnI_3$ NCs

In an Ar-filled glovebox, 1.2 mL of CsI NCs solution was load in a 9 mL glass bottle, and then heated at 95 °C and stirred at 200 rpm on the heating plate. After preheating for

45 s, 0.33 mL amount of SnI_2-TOP precursor was swiftly injected into the CsI NCs solution. After 60 min of reaction, the ensuing crude solution was allocated to a centrifuge tube. After centrifugation at 500 rpm for 1 min, the precipitates were removed, and then the supernatant was centrifugate at 12000 rpm for 5 min, this time the supernatant was removed. After repeating the previous step one more time, the resultant $CsSnI_3$ NCs precipitates were collected and used for the characterization.

Synthesis of $CsSnBr_3$ NCs

The synthesis of $CsSnBr_3$ NCs was similar to that of $CsSnI_3$ NCs. For the synthesis of $CsSnBr_3$ NCs, the reaction involves CsBr NCs and $SnBr_2$ precursors.

Synthesis of $(R\text{-}NH_3^+)_2SnI_4$ and $(R\text{-}NH_3^+)_2Cs_{n-1}Sn_nI_{3n+1}$ ($n > 1$)

First, I prepared a solution of approximately 0.5 mmol/mL of OAmI by dissolving 0.25 mg of OAmI in 1 mL toluene. Next, 100 μL of SnI_2-TOP precursor solution was added to 200 μL of the OAmI solution, and after thorough mixing, 100 μL of the resulting mixture was transferred into 1 mL of n-hexane. Upon immediate observation, the mixture exhibited a red color and emitted bright red light under UV light at 360 nm. After centrifugation at 12000 rpm for 5 min, the supernatant was removed to obtain $(R\text{-}NH_3^+)_2SnI_4$.

To synthesis of $(R\text{-}NH_3^+)_2Cs_{n-1}Sn_nI_{3n+1}$ was similar to that of $(R\text{-}NH_3^+)_2SnI_4$. The only difference is the introduction of a certain amount of Cs-oleate into the mixture of OAmI and SnI_2-TOP precursor. It should be noted that as the amount of Cs-oleate increases, the emission peak of the resulting $(R\text{-}NH_3^+)_2Cs_{n-1}Sn_nI_{3n+1}$ gradually shifts to longer wavelengths (red-shifts).

3.2.2 Characterization

Structure, Morphology, Scanning electron microscopy (SEM) and energy dispersive X-ray spectroscopy (EDS) Characterization.

XRD data were recorded on a MiniFlex 600 diffractometer (Rigaku) with Cu Kα radiation ($\lambda = 1.5418$ Å). The NCs were dispersed in hexane to form a concentrated NCs

solution, and the solution was dropped on an anaerobic sample holder for the XRD measurements. TEM samples were prepared by dropping a dilute NC-hexane solution onto a TEM copper grid and dried in an Ar-filled glovebox. TEM images were measured by a JEM-2100F (JEOL) microscope operated at 200 kV. FTIR spectra were recorded using a Jasco 4100 FTIR spectrometer. For SEM-EDS, the samples were coated onto conductive adhesive and subjected to gold sputter coating prior to SEM-EDS measurement of the samples.

Luminescence and Absorption Characterization.

The PL spectra were measured by a NanoLog Horiba Jovin Yvon spectrofluorometer with a continuous 450 W xenon lamp. The absolute PLQYs were measured by a C9920-03G system equipped with a 150 W xenon lamp (Hamamatsu Photonics). The PL decays were obtained with a time-correlated single photon counting lifetime spectroscopy system (NanoLog, Horiba Jovin Ybon), equipped with a pulse laser (λ_{em} = 726 nm). The absorption spectra were measured by a UV-vis-NIR spectrophotometer (V-770, JASCO).

Detailed method for the calculation of the average lifetime, radiative, and nonradiative recombination rates.

Using PLQYs and average lifetimes, I evaluated the radiative and nonradiative decay rates based on the following equations:

$$\tau_{ave} = (A_1\tau_1^2 + A_2\tau_2^2 + \cdots)/(A_1\tau_1 + A_2\tau_2 + \cdots) \quad (1)$$

$$\Gamma_{rad} = \frac{\mathrm{PLQY}}{\tau_{ave}} \quad (2)$$

$$\Gamma_{non-rad} = \frac{1}{\tau_{ave}} - \Gamma_{rad} = \frac{1 - \mathrm{PLQY}}{\tau_{ave}} \quad (3)$$

where A_i (i=1, 2, and 3) and τ_i (i=1, 2, and 3) are the amplitudes and the corresponding fitted lifetimes, respectively, τ_{ave} is the average lifetime of the samples, and Γ_{rad} and $\Gamma_{non\text{-}rad}$ are the radiative and non-radiative recombination rates, respectively.

3.3 Results and discussion

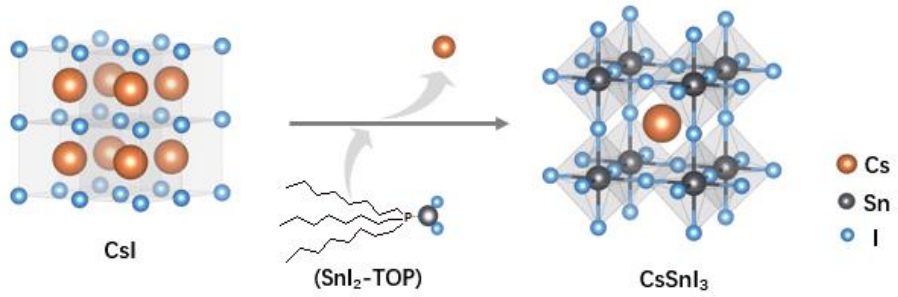

Figure 3.1 The schematic diagram of synthesizing $CsSnI_3$ NCs using the CsI NCs phase transition method. It also presents the structural diagrams of cubic CsI and orthorhombic $CsSnI_3$.

In this work, I achieved the transformation of CsX (X= I or Br) NCs into lead-free perovskite $CsSnX_3$ NCs through a simple liquid-phase reaction. The detailed synthesis is shown in **Figure 3.1**. Taking the synthesis of $CsSnI_3$ NCs as an example, the process involves first preparing CsI NCs. Next, I prepared the SnI_2-TOP precursor by mixing SnI_2 with tri-n-octylphosphine (TOP) at 120 ℃, followed by allowing CsI NCs to undergo a phase transition reaction in the liquid phase with the prepared SnI_2-TOP precursor. After completion of the reaction, $CsSnI_3$ NCs are obtained. CsI NCs were obtained by dissolving ZnI_2 halide precursor with oleic acid (OA) and oleylamine (OAm) in 1-Octadecene (ODE), followed by the injection of cesium oleate and subsequent reaction on a hotplate at a certain temperature for a specific duration, followed by centrifugation and purification. In this case, the reaction temperature was a crucial factor affecting the size of CsI NCs. Initially, CsI NCs of varying sizes were obtained at different temperatures. Morphological observations using transmission electron microscopy (TEM) revealed truncated octahedral shapes for all CsI NCs (**Figure 3.2**). The average size of $CsSnI_3$ NCs is described using Gaussian distribution functions fitted to the data, while the full width at half maximum (FWHM) of the fitted peaks is used to characterize the size distribution. The average size of CsI NCs obtained at 25°C (CsI-25°C) was 14.5±2.4 nm, while those synthesized at 60°C (CsI-60°C) and 100°C (CsI-100°C) exhibited size distributions of 17.8±4.2 nm and 23.6±6.4 nm, respectively. This indicates that increasing

the temperature facilitates the formation of larger CsI NCs effortlessly. High-resolution transmission electron microscopy (HRTEM) images and corresponding Fast Fourier transform (FFT) patterns confirmed the single-crystalline nature of these NCs, with interplanar spacings consistent 3.23 Å with the (110) crystal planes of cubic-phase CsI. Further confirmation of the cubic-phase crystal structure of these CsI NCs was provided by X-ray diffraction (XRD) patterns, which matched perfectly with the peaks of the PDF standard card (ICSD code 60498) without any impurity phases (**Figure 3.3**). The FWHM of the main peak at 27.6° in the XRD patterns exhibited significant size dependence, decreasing from 0.728° to 0.401° as the synthesis temperature increased from 25°C to 100°C, consistent with the size variation observed in TEM.

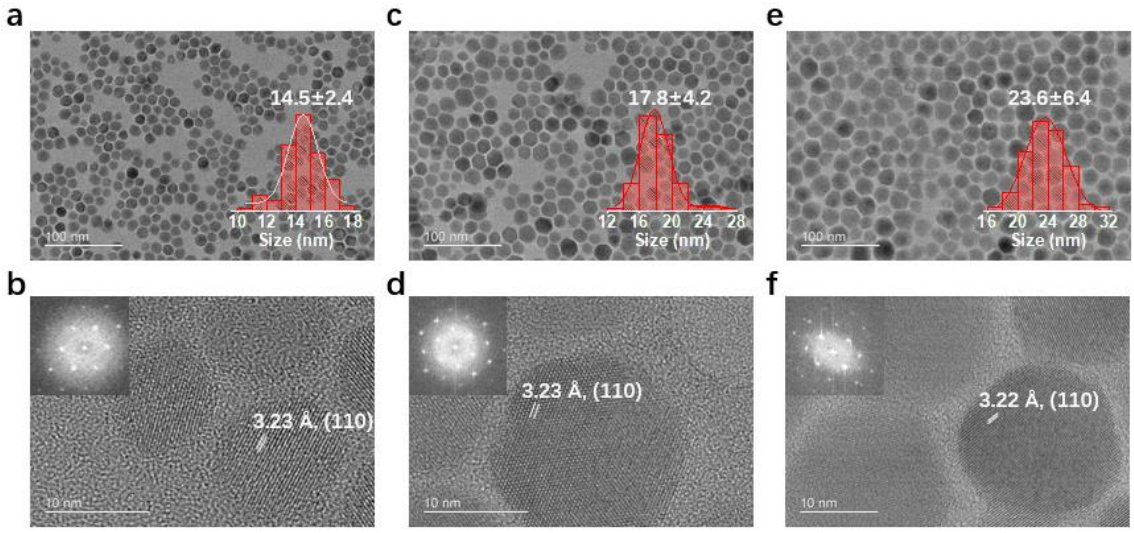

Figure 3.2 TEM images of CsI NCs of three representative sizes and HRTEM images (bottom panels). The insets display the size distribution plot and Fast Fourier Transform pattern of the corresponding CsI NCs. These CsI NCs were synthesized under different temperatures: (a, b) at 25°C, (c, d) at 60°C, and (e, f) at 100°C, respectively.

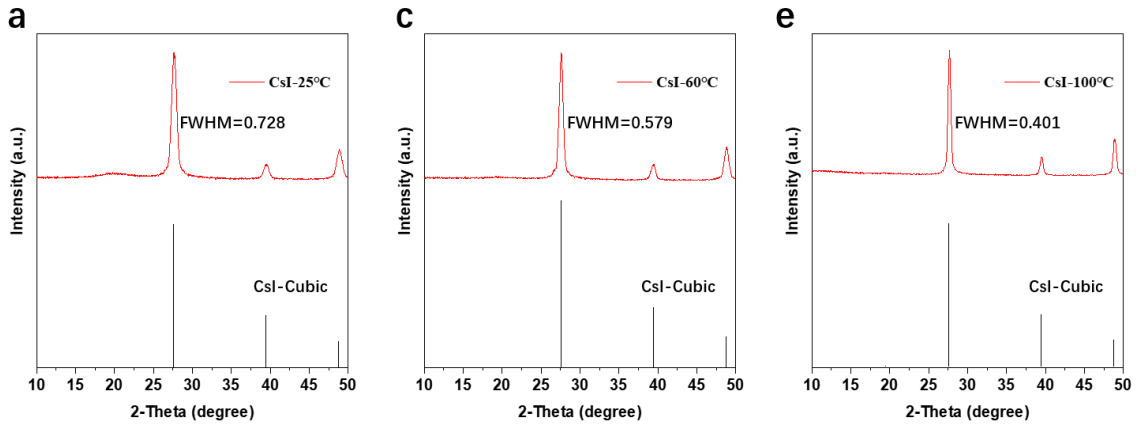

Figure 3.3 XRD patterns of CsI NCs with three representative sizes. These CsI NCs were synthesized under different temperatures: (a) at 25°C, (b) at 60°C, and (c) at 100°C, respectively.

Subsequently, I conducted compositional analysis on the CsI NCs synthesized at 60°C. scanning electron microscopy (SEM) coupled to an energy dispersive X-Ray spectrometer (EDS) revealed a Cs-to-I ratio of 1:1.21, indicating an iodine-rich surface (**Figure 3.4**). Additionally, no signal of Zn was detected (**Figure 3.4a, f**), indicating that ZnI_2 solely serves as a source of iodide and does not introduce Zn into the CsI lattice.

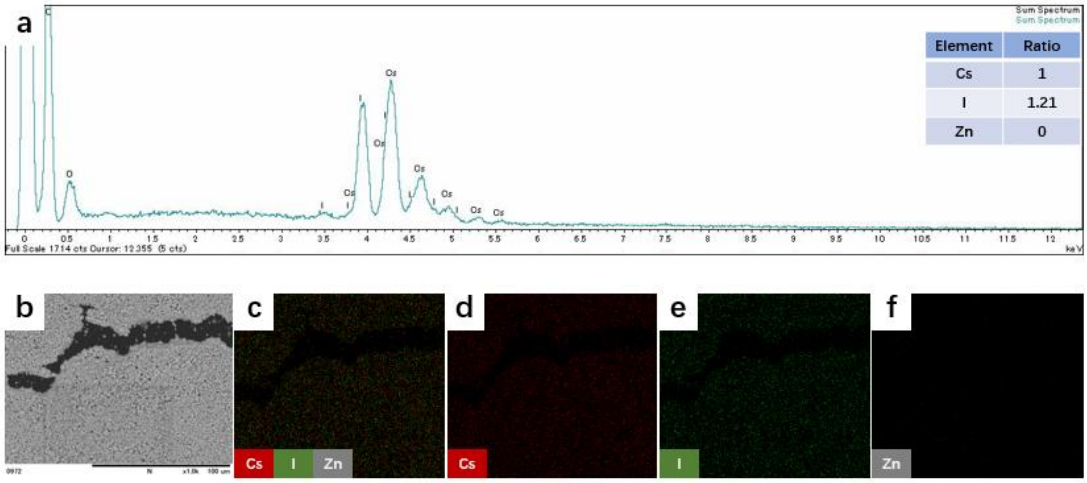

Figure 3.4 (a) SEM-EDS spectrum and elemental quantitative data, (b) SEM image, and (c-f) EDS mapping analysis of CsI NCs synthesized at 60°C

To synthesis of $CsSnI_3$ NCs, I directly injecting the SnI_2-TOP precursor solution, prepared using SnI_2 and TOP, into a toluene solution containing CsI NCs. This method

enabled us to obtain stable colloidal $CsSnI_3$ NCs. Detailed synthesis procedures can be found in the Experimental Section. TEM analysis revealed that the obtained $CsSnI_3$ NCs exhibited highly uniform sizes(**Figure 3.5a, c,** and **e**). With an increase in the size of the CsI NCs used, the size of the resulting $CsSnI_3$ NCs also increased accordingly. For instance, $CsSnI_3$ NCs obtained from CsI-25℃ (CsI-25℃-$CsSnI_3$) had an average size of 14.1±3.9 nm, while those from CsI-60°C and CsI-100°C had sizes of 14.6±4.4 nm and 23.0±8.4 nm, respectively. It is worth noting that $CsSnI_3$ NCs prepared from CsI-25℃ and CsI-60℃ did not exhibit a significant difference in size. This may be attributed to the low formation energy of $CsSnI_3$, which makes it easier for small-sized $CsSnI_3$ NCs with high surface activity to grow, thus hindering the formation of smaller $CsSnI_3$ NCs. Furthermore, compared to small-sized $CsSnI_3$ NCs, large-sized $CsSnI_3$ NCs exhibit a more dispersed size distribution. Nevertheless, this demonstrates the capability of easily achieving size-tunable $CsSnI_3$ NCs using this method, with the potential to obtain even larger sizes. HRTEM analysis of these NCs revealed lattice fringes consistent with the orthorhombic phase structure of $CsSnI_3$. The lattice spacings of 6.13 Å and 3.06 Å correspond to the (110) and (220) crystal planes of the orthorhombic phase $CsSnI_3$, respectively. While the spacing of 3.10 Å corresponds to the (004) crystal plane of the orthorhombic phase $CsSnI_3$ (**Figure 3.5b, d,** and **f**). FFT patterns from HRTEM also confirmed the single-crystalline nature of the orthorhombic phase structure in these NCs. XRD analysis of the obtained $CsSnI_3$ NCs matched well with the orthorhombic perovskite structure (ICSD code 262926), and no secondary crystalline phases were detected, confirming the complete conversion of CsI to $CsSnI_3$ (**Figure 3.6a**).

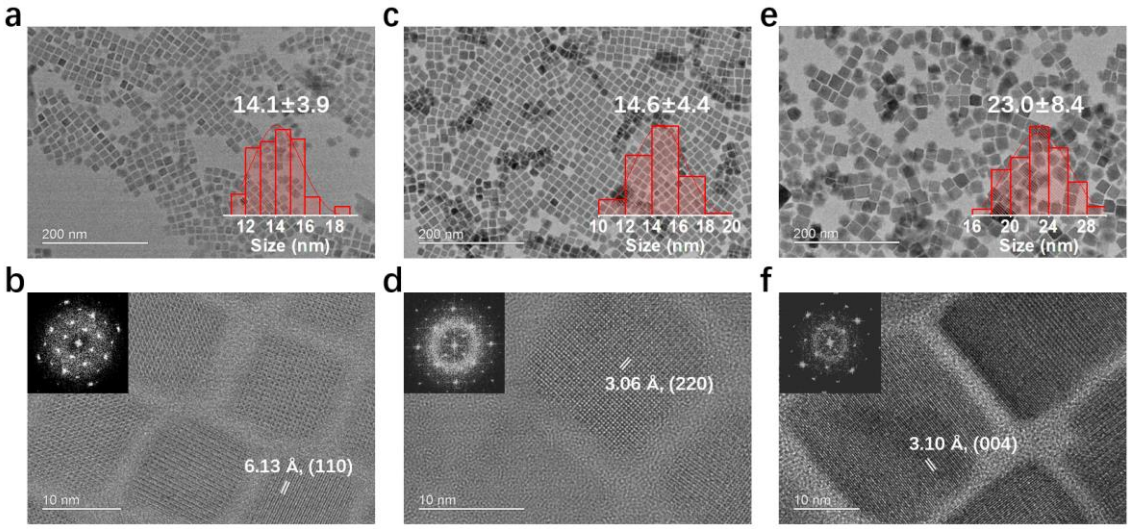

Figure 3.5 TEM images of $CsSnI_3$ NCs of three representative sizes and HRTEM images (bottom panels). The insets display the size distribution plot and Fast Fourier Transform (FFT) pattern of the corresponding CsSnI3 NCs. These $CsSnI_3$ NCs were synthesized using different CsI NCs : (a, b) CsI-25°C, (c, d) CsI-60°C, and (e, f) CsI-100°C, respectively.

Subsequently, I investigated the optical properties of the obtained $CsSnI_3$ NCs with different sizes. The photoluminescence (PL) and optical absorption spectra of these NCs are shown in **Figure 3.6b**. All $CsSnI_3$ NCs exhibited a PL emission peak at 954 nm, with FWHM values of 62.6 nm, 62.3 nm, and 65.0 nm for the three sizes of $CsSnI_3$ NCs, respectively. This narrower PL emission peak compared to previously reported $CsSnI_3$ NCs is primarily attributed to the narrower size distribution of the $CsSnI_3$ NCs obtained in my study.[21, 32] Additionally, I investigated the PLQY of these $CsSnI_3$ NCs. Under excitation at 840 nm, the $CsSnI_3$ NCs exhibited a maximum PLQY of 34.4%, which is noteworthy as it represents a record value, double the previously reported PLQY of $CsSnI_3$ NCs.[34] The PLQY values for the CsI-25℃-$CsSnI_3$ NCs and CsI-100℃-$CsSnI_3$ NCs were 32.8% and 24.9%, respectively. The significantly decrease in PLQY observed for the larger $CsSnI_3$ NCs may be associated with the presence of more bulk defects in larger NCs. Nonetheless, all $CsSnI_3$ NCs of different sizes exhibit higher PLQY compared to previously reported values.[21, 35, 36]

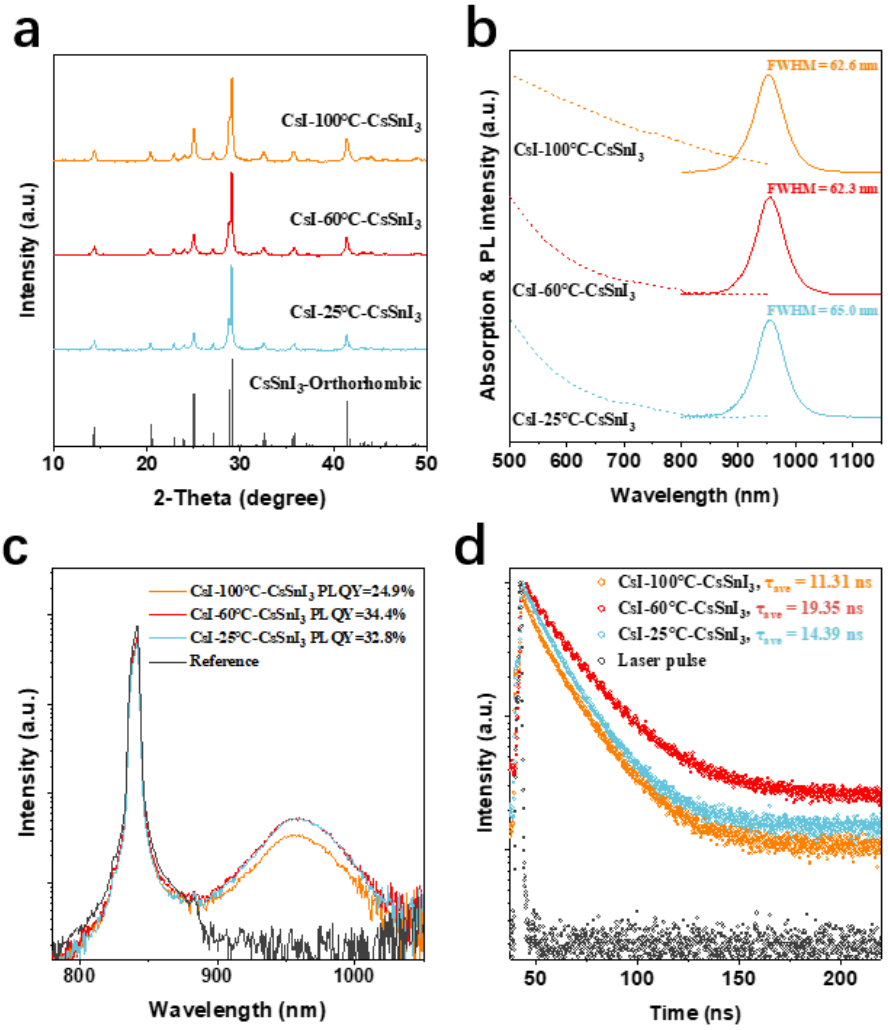

Figure 3.6 (a) XRD patterns, (b) PL and absorption spectra, (c) PLQY at 840 nm excitation, and (d) PL decay and average lifetimes (τ_{ave}) of $CsSnI_3$ NCs synthesized using different CsI NCs.

Table 3.1. Fitting results of PL decay curves, τ_{ave}, PLQYs, radiative (Γ_{rad}) and nonradiative ($\Gamma_{non\text{-}rad}$) decay rates of $CsSnI_3$ NCs. Note that the decays were fitted with a double-exponential function.

Sample	A_1	τ_1 (ns)	A_2	τ_2 (ns)	τ_{ave} (ns)	PLQY (%)	Γ_{rad} (μs^{-1})	$\Gamma_{non\text{-}rad}$ (μs^{-1})
CsI-25°C-$CsSnI_3$	0.28	6.59	0.72	17.38	14.39	24.90	17.30	52.19
CsI-60°C-$CsSnI_3$	0.34	11.50	0.66	23.47	19.35	34.40	17.78	33.90
CsI-100°C-$CsSnI_3$	0.39	2.62	0.61	16.95	11.31	32.80	29.00	59.42

Afterward, I performed time-resolved PL measurements to gather information about

the transient evolution of photo-generated charge carriers. **Figure 3.6d** exhibits the decay curves of these $CsSnI_3$ NCs. I observed that the $CsSnI_3$ NCs with the highest PLQY exhibited slower PL decay. By fitting all decay curves with double-exponential function and subtracting the influence of the pump laser, I obtained the average lifetimes of these $CsSnI_3$ NCs, as detailed in **Figure 3.6d** and **Table 3.1**. The fitting results include fast and slow decay components, whose variation trends are basically consistent with the average lifetime. Based on the average lifetime and PLQY, I also evaluated the radiative and nonradiative recombination rates. Clearly, the CsI-60°C-$CsSnI_3$ NCs with the longest average lifetime showed the lowest nonradiative recombination rate (33.90 μs^{-1}), indicating the lowest defect concentration. However, the smaller-sized CsI-25°C-$CsSnI_3$ NCs and larger-sized CsI-100°C-$CsSnI_3$ NCs exhibit higher nonradiative recombination rates (52.19 and 59.42 μs^{-1}, respectively), indicating higher defect concentration.

It is well known that $CsSnI_3$ NCs typically exhibit poor stability. Previous results have indicated that even when stored in a nitrogen-filled glovebox, the PLQY of $CsSnI_3$ NCs decreases to below 80% of its original intensity within 3 hours.[34] However, I observed significantly enhanced stability in my $CsSnI_3$ NCs; dispersed in hexane, my CsI-60°C-$CsSnI_3$ NCs retained over 80% of their original PLQY after 9 days in glovebox (**Figure 3.7**). This enhanced stability could be attributed to the substantially reduced defect density in my $CsSnI_3$ NCs compared to those prepared using other strategies that result in poorly luminescent $CsSnI_3$ NCs. [21, 35-37]

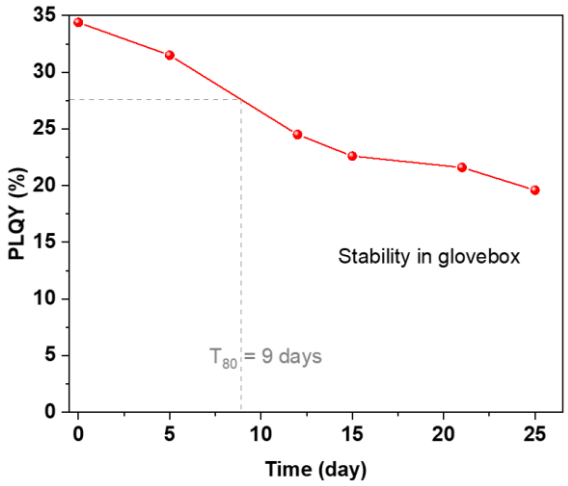

Figure 3.7 PLQY stability in Ar-filled glovebox of $CsSnI_3$ NCs synthesized using CsI obtained at 60℃ NCs. The gray dashed line in the figure indicates the time corresponding to when the PLQY drops to 80% of its original intensity.

I investigated the elemental composition of the CsI-60℃-$CsSnI_3$ NCs with a PLQY of 34.4%. SEM-EDS analysis revealed a higher concentration of I and Sn ions in these NCs, with a Cs/Sn/I ratio of 1/1.16/3.49 (**Figure 3.8**), suggesting that my $CsSnI_3$ NCs may have a more perfect surface protected by Sn and I ions. Previous studies have shown that synthesizing $CsSnI_3$ NCs with excess Sn and I can effectively reduce tin vacancies (V_{Sn}) in the NCs, a condition crucial for improving the PLQY.[34, 37] Subsequently, I adjusted the amount of SnI_2-TOP precursor to control the Sn and I ratio based on the synthesis conditions of CsI-60℃-$CsSnI_3$ NCs. CsI-60℃-$CsSnI_3$ NCs with a PLQY of 34.4% were considered the optimal sample, synthesized using 330 μL (~0.165 mmol) of SnI_2-TOP precursor. Therefore, in comparative experiments, I respectively increased and decreased the amount of SnI_2-TOP precursor. The results showed that the use of 300 μL (~0.15 mmol) and 360 μL (~0.18 mmol) of SnI_2-TOP precursor significantly reduced the PLQY of the $CsSnI_3$ NCs to 25.2% and 23.3%, respectively (**Figure 3.9a**). Additionally, they exhibited a decrease in the average PL lifetime (**Figure 3.9b** and **Table 3.2**).

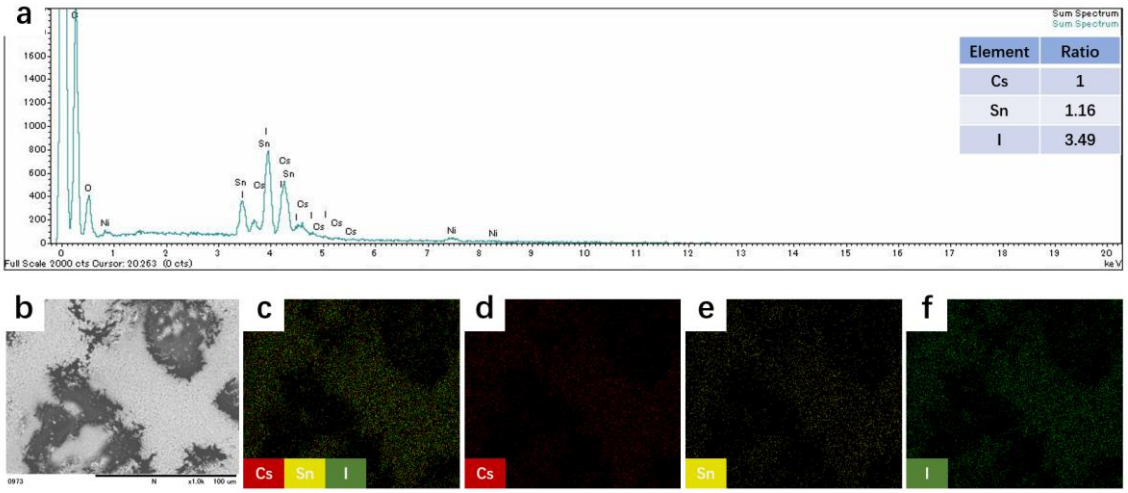

Figure 3.8 (a) SEM-EDS spectrum and elemental quantitative data, (b) SEM image, and (c-f) EDS mapping analysis of $CsSnI_3$ NCs synthesized using CsI obtained at 60℃ NCs.

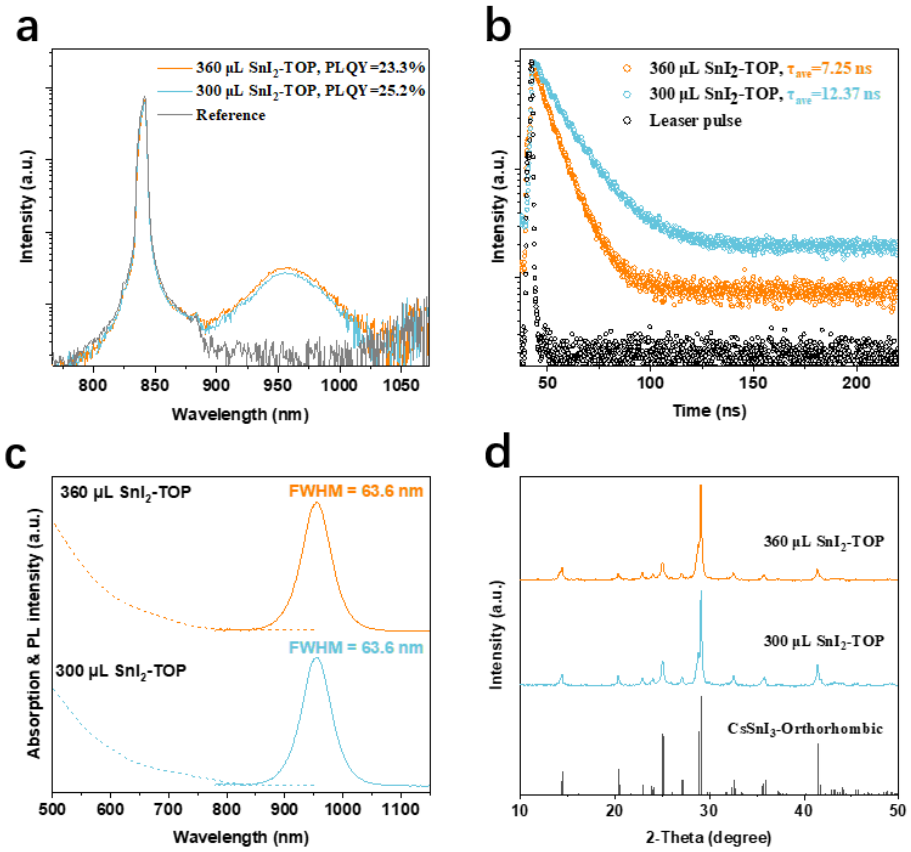

Figure 3.9 PLQY at 840 nm excitation (a), PL decay and average lifetimes (τ_{ave}) (b), and PL & absorption spectra (c) of $CsSnI_3$ NCs. These NCs synthesized using 300 μL and 360 μL SnI_2-TOP precursors, respectively. (d) XRD patterns of $CsSnI_3$ NCs synthesized using 300 μL and 360 μL SnI_2-TOP precursors, respectively.

Table 3.2. Fitting results of PL decay curves, τ_{ave}, PLQYs, radiative (Γ_{rad}) and nonradiative ($\Gamma_{non\text{-}rad}$) decay rates of $CsSnI_3$ NCs. Note that the decays were fitted with a double-exponential function.

Sample	A_1	τ_1 (ns)	A_2	τ_2 (ns)	τ_{ave} (ns)	PLQY (%)	Γ_{rad} (μs^{-1})	$\Gamma_{non\text{-}rad}$ (μs^{-1})
360 μL SnI_2-TOP	0.29	4.10	0.71	8.54	7.25	23.30	32.14	105.79
300 μL SnI_2-TOP	0.47	8.78	0.53	15.61	12.37	25.20	20.37	60.47

I also examined the other structural and optical properties of these $CsSnI_3$ NCs. Their PL and absorption spectra did not exhibit significant differences compared to the optimal sample (**Figure 3.9c**), and XRD analysis suggested that these $CsSnI_3$ NCs possessed a

pure orthorhombic phase structure (**Figure 3.9d**). The only difference observed was a slight variation in NCs size and size distribution when altering the amount of SnI_2-TOP (**Figure 3.10**). This further emphasizes the importance of maintaining adequate and appropriate amounts of Sn and I during the synthesis of $CsSnI_3$ NCs, regardless of the synthetic approach used.

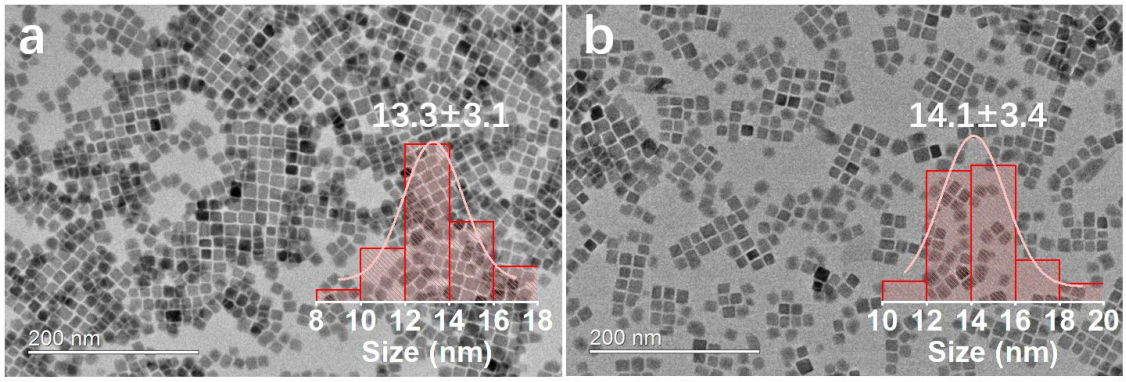

Figure 3.10 TEM image of $CsSnI_3$ NCs synthesized using 300 μL (a) and 360 μL (b) SnI_2-TOP precursors. Insets show the histograms of edge lengths of corresponding $CsSnI_3$ NCs.

I conducted a detailed investigation into the reaction process of CsI transforming into $CsSnI_3$ NCs. Through the investigation of the structure and optical properties of the products obtained at different reaction time, I found that the entire phase transition process is extremely slow. Initially, at 20 seconds (s) into the reaction, the reaction was quenched using an ice bath, and the precipitate was obtained after centrifugation. At this time, the product exhibited strong emission peaks at 720 nm and 781 nm, respectively (**Figure 3.11a**). XRD analysis revealed that the primary component of the product at this stage was CsI, with weak diffraction peaks corresponding to a second phase observed at 11.3° and 13.7° (**Figure 3.11b**). This second phase was attributed to the presence of oleylamine ligands on the surface of CsI NCs, which, along with Cs and SnI_2-TOP precursor, led to the formation of a two-dimensional perovskite structure $(R\text{-}NH_3^+)_2Cs_{n-1}Sn_nI_{3n+1}$ ($n > 1$), and its verification. Oleylamine readily forms $(R\text{-}NH_3^+)_2SnI_4$ two-dimensional perovskite with SnI_2 and exhibits broad fluorescence emission at 676 nm, with a strong exciton absorption peak at 590 nm (**Figure 3.11c**). This indicating that the

emission around 710~720 nm cannot originate from this substance. Subsequently, when $(R\text{-}NH_3^+)_2SnI_4$ was synthesized with the introduction of cesium oleate (Cs-Oleate), the product exhibited a prominent PL peak at 710 nm, along with an exciton absorption peak similar to that of $(R\text{-}NH_3^+)_2SnI_4$, but red-shifted to 684 nm. (**Figure 3.11c**). XRD analysis confirmed only low-angle diffraction peaks, characteristic of a two-dimensional perovskite structure.[38-41] Furthermore, noticeable low-angle (0.15°) shifts in XRD peak positions compared to $(R\text{-}NH_3^+)_2SnI_4$ were observed, attributed to the incorporation of Cs ions into the $(R\text{-}NH_3^+)_2SnI_4$ lattice, forming multilayered $(R\text{-}NH_3^+)_2Cs_{n-1}Sn_nI_{3n+1}$ two-dimensional perovskite structure (**Figure 3.10d**). Furthermore, the formation of the $CsSnI_3$ perovskite structure was not observed in the XRD pattern obtained from the sample $(R\text{-}NH_3^+)_2Cs_{n-1}Sn_nI_{3n+1}$ (**Figure 3.11d**). Elemental analysis conducted via SEM-EDS allowed us to tentatively determine the structural formula as $(R\text{-}NH_3^+)_{2.1}Cs_{0.1}SnI_{4.2}$ (**Figure 3.12**). On the other hand, the PL peak around 781 nm observed in the product at 20 s and 5 min was attributed to small laterally sized $CsSnI_3$ (**Figure 3.11a**), exhibiting a significant blue shift compared to bulk $CsSnI_3$ due to quantum confinement effects.

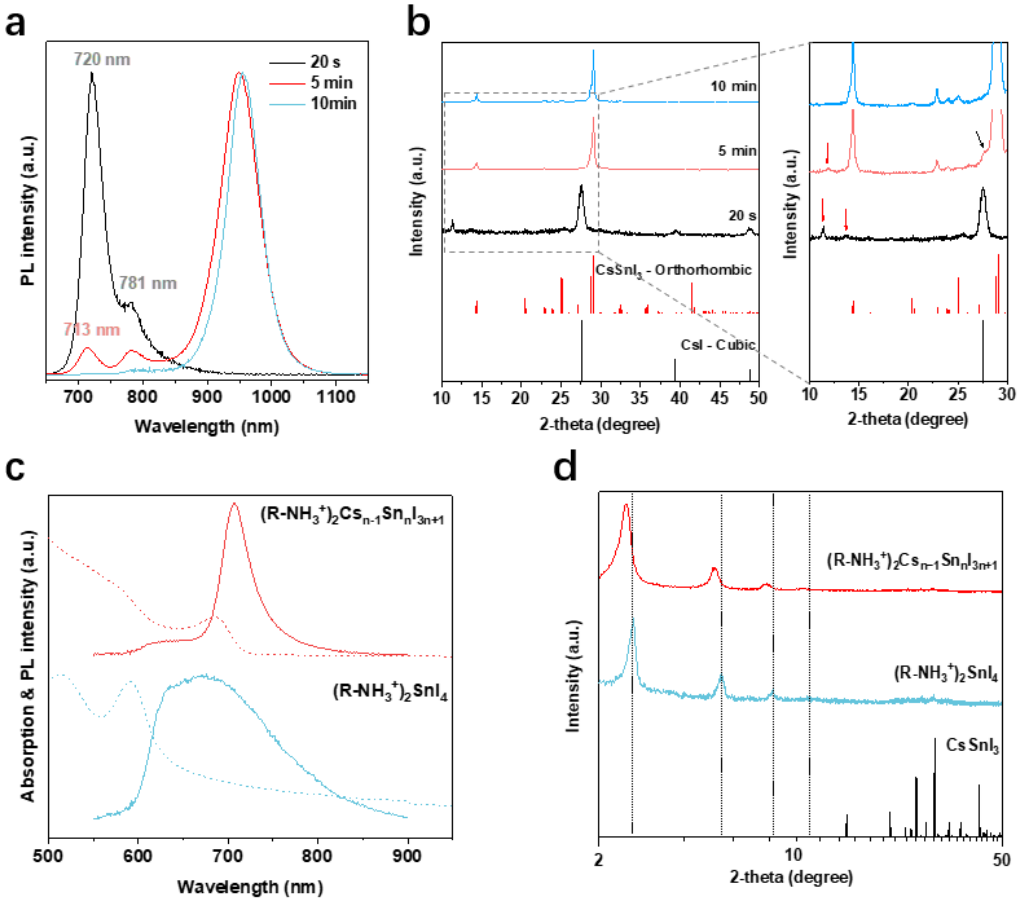

Figure 3.11 (a) PL spectra, (b) XRD patterns and their partial enlargement of the products separated at 20 s, 5 min and 10 min of the reaction are presented. The impurity labeled by the black arrow in the (b) is CsI, and the red arrow is the perovskite phase. (c) PL and absorption spectra, (d) XRD patterns of two-dimensional perovskite $(R\text{-}NH_3^+)_2SnI_4$ and $(R\text{-}NH_3^+)_2Cs_{n-1}Sn_nI_{3n+1}$. Please note that for clarity, the horizontal axis of the XRD patterns has been logarithmically scaled.

Subsequently, products were obtained at 5- and 10-minute (min) intervals during the reaction. The XRD analysis of the product at 5 min revealed that approximately 8% of CsI remained unconverted into $CsSnI_3$. As shown in **Figure 3.11b**, a weak peak at 27.6° (known by the black arrow) in the XRD pattern corresponded to the (110) crystal plane of CsI. At 5 min, the product exhibited a prominent PL peak at 950 nm (**Figure 3.11a**). When the reaction time reaches 10 min, CsI NCs had completely transformed into $CsSnI_3$ NCs. XRD analysis of the product at this stage indicated a single orthorhombic phase of

$CsSnI_3$ (**Figure 3.11b**), with PL only showing a strong fluorescence emission peak at 955 nm (**Figure 3.11a**).

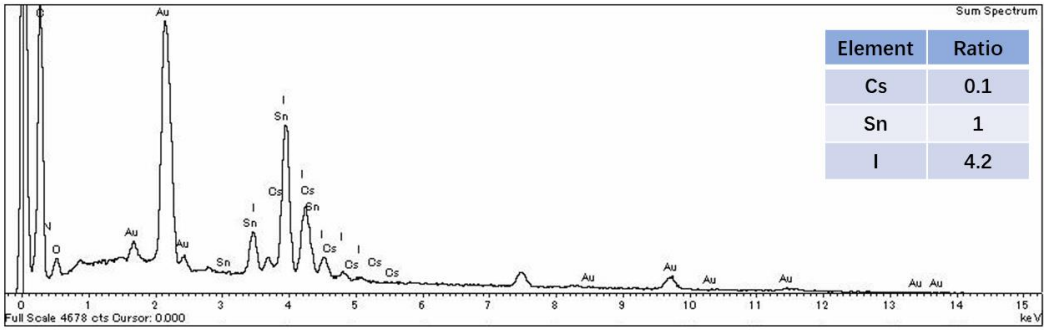

Figure 3.12 SEM-EDS spectrum and elemental quantitative data of two-dimensional perovskite (R-NH_3^+)$_2$$Cs_{n-1}Sn_nI_{3n+1}$.

After centrifugation, although the extracted product allowed for accurate structural analysis, thereby indirectly illustrating the phase transition process, some of the products remained unseparated in the crude solution. Therefore, I investigated the PL spectra of the crude solution throughout the phase transition process. Similar to the precipitate product, the crude solution exhibited PL emission around 710 nm within the initial 20 seconds (**Figure 3.13a**). Additionally, a distinct excitonic absorption peak appeared at 687 nm in its absorption spectrum (**Figure 3.13b**), attributed to the two-dimensional perovskite (R-NH_3^+)$_2$$Cs_{n-1}Sn_nI_{3n+1}$. As the formation of $CsSnI_3$ phase progressed, within 1 min, the PL peak rapidly shifted to 785 nm (**Figure 3.13a**), owing to the $CsSnI_3$ thin layer formed on the surface of CsI NCs. As the reaction proceeded, the thickness of the $CsSnI_3$ thin layer on the surface of CsI increased, resulting in a broad PL peak around 875 nm at 4 min (**Figure 3.13a**). As the $CsSnI_3$ structure gradually formed and grew, the two-dimensional perovskite (R-NH_3^+)$_2$$Cs_{n-1}Sn_nI_{3n+1}$ gradually disappeared, corresponding to the weakening and eventual disappearance of the excitonic absorption peak at 687 nm in the absorption spectrum (**Figure 3.13b**). Evidence of coexistence of CsI and $CsSnI_3$ phases was observed through TEM, as shown in **Figure 3.13c**, where the (220) crystal plane of $CsSnI_3$ was clearly observed on the surface of CsI. This confirmed the gradual

phase transition from the surface of CsI towards the interior. Two possible phase transition processes were considered: one involving the replacement of two Cs atoms in CsI with one Sn atom, and the other involving gradual diffusion of Sn atom and I atom into the CsI lattice. However, by comparing the sizes of CsI and $CsSnI_3$ before and after the phase transition, no significant increase in size was observed (**Figure 3.2** and **Figure 3.5**), suggesting that $CsSnI_3$ was unlikely formed by the insertion of Sn atom and I atom into the CsI lattice. Therefore, it can be inferred that the phase transition mechanism is primarily characterized by the replacement of Cs atom by Sn atom to form $CsSnI_3$.

Upon completion of the phase transition at 10 min, the PL spectrum of the crude solution unequivocally exhibited a strong emission peak at 951 nm (**Figure 3.13a**). It is worth noting that even after 60 min, following the completion of the phase transition, a weak emission at 785 nm was still observed in the PL spectrum of the crude solution (**Figure 3.13a**). This could possibly stem from small-sized $CsSnI_3$ NCs formed due to excess SnI_2-TOP precursor solution and free Cs ions. This speculation was confirmed by TEM analysis of the crude solution, where numerous nanoscale particles ranging in size from 3 to 5 nm were found in the crude solutions at 10 and 60 min of reaction time (**Figure 3.13d, e**). Through HRTEM, lattice spacings of 2.13 Å and 3.00 Å were determined, corresponding to the (401) and (203) crystal planes of orthorhombic $CsSnI_3$, respectively. This result confirms that the emission around 785 nm originates from small-sized $CsSnI_3$ NCs exhibiting quantum confinement effects. Furthermore, the presence of free Cs ions may originate from Cs being replaced by Sn during the phase transition from CsI to $CsSnI_3$, was essential for the formation of these small-sized $CsSnI_3$ NCs.

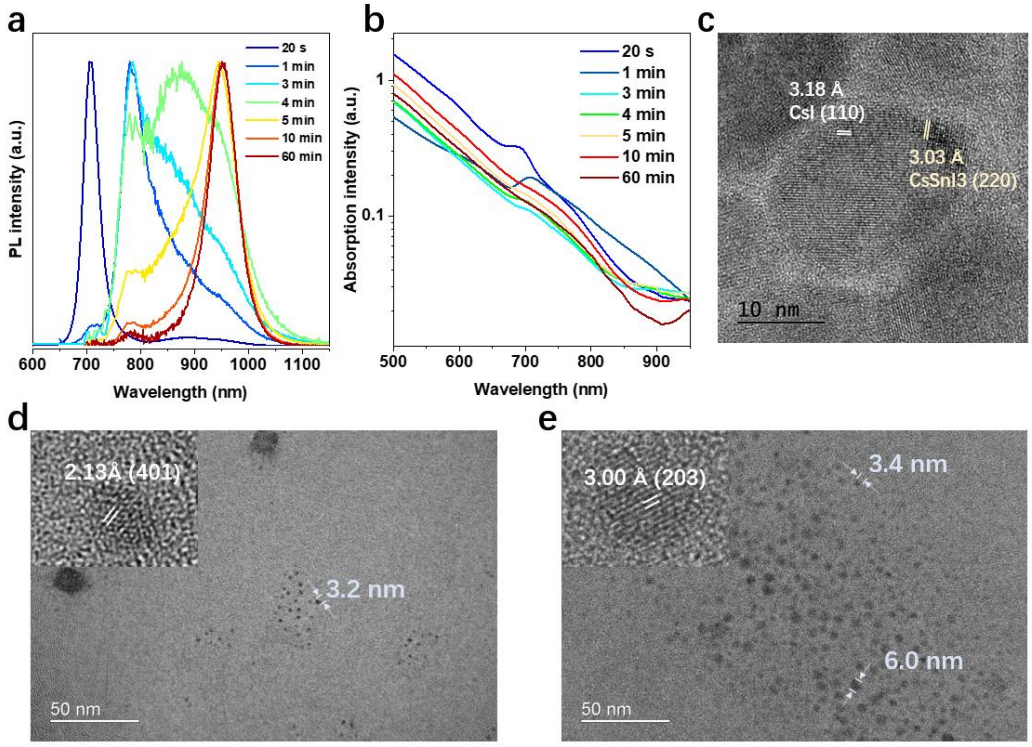

Figure 3.13 PL (a) and absorption (b) spectra of the crude solution during the synthesis of $CsSnI_3$ NCs using CsI NCs. (c) HRTEM image of the intermediate product during the transformation of CsI NCs to $CsSnI_3$ NCs. It is revealed that the surface of these NCs exhibits $CsSnI_3$ structure, while the interior retains CsI structure. TEM and HRTEM images of the crude solution after 10 min (d) and 60 min (d) of the synthesis process of $CsSnI_3$ NCs from CsI NCs.

It is noteworthy that immediately after purification following the completion of the 10 min (NCs-10 min) reaction, the $CsSnI_3$ NCs did not exhibit a significantly high PLQY (21.0%) (**Figure 3.14a**). To eliminate defects in the $CsSnI_3$ NCs, it was found beneficial to perform high-temperature annealing for a certain duration. In addition to the optimal sample obtained after 60 min of reaction, I also investigated the optical properties of samples obtained after 40 and 90 min of reaction (Labeled NCs-40 min and NCs-90 min, respectively). Compared to the sample obtained after 60 min, the $CsSnI_3$ NCs obtained after 40 and 90 min showed no significant changes in PL peak position and absorption spectra, but the PLQY and PL lifetime were significantly reduced (**Figure 3.14a, b**).

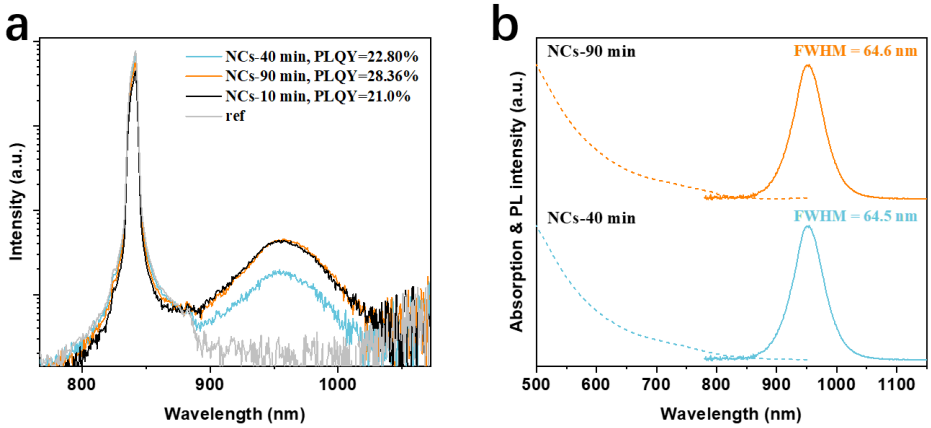

Figure 3.14 (a) PLQYs at 840 nm excitation of $CsSnI_3$ NCs obtained after 10, 40 and 90 min of reaction. (b) PL & absorption spectrum of $CsSnI_3$ NCs obtained after 40 and 90 min of reaction.

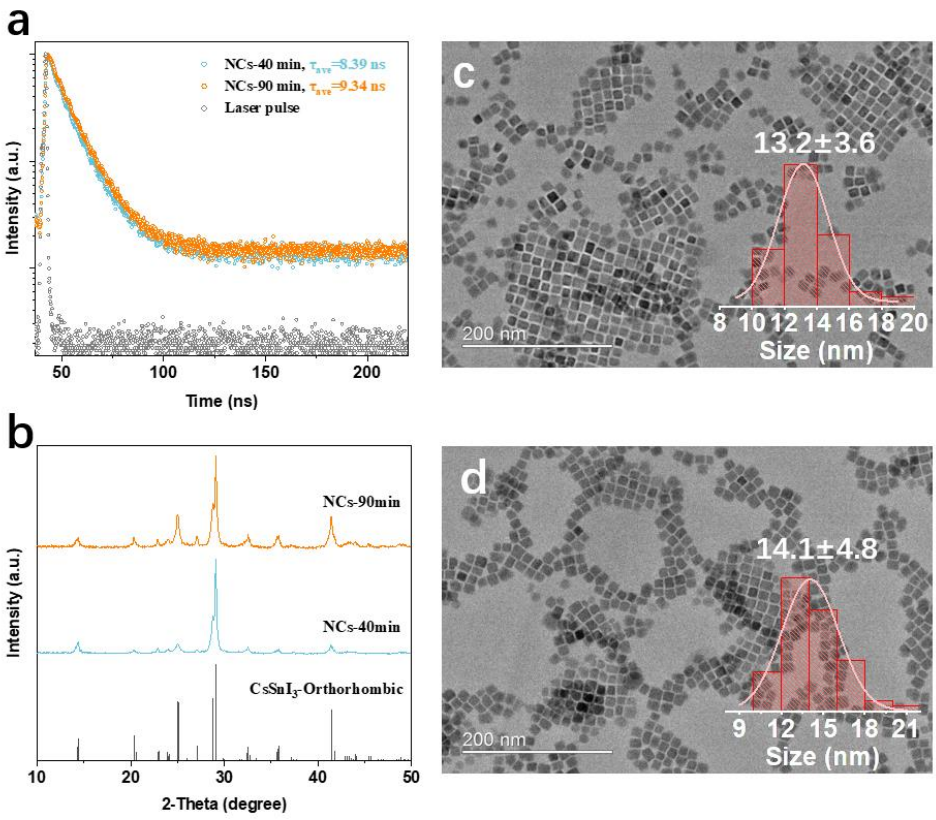

Figure 3.15 (a) PL decay and average lifetimes (τ_{ave}) of $CsSnI_3$ NCs obtained after 40 and 90 min of reaction. (b) XRD patterns of $CsSnI_3$ NCs obtained after 40 and 90 min of reaction. TEM image of $CsSnI_3$ NCs obtained after 40 (d) and 90 min (e) of reaction. Insets show the histograms of edge lengths of corresponding $CsSnI_3$ NCs.

Table 3.3. Fitting results of PL decay curves, τ_{ave}, PLQYs, radiative (Γ_{rad}) and nonradiative ($\Gamma_{non\text{-}rad}$)

decay rates of $CsSnI_3$ NCs. Note that the decays were fitted with a double-exponential function.

Sample	A_1	τ_1 (ns)	A_2	τ_2 (ns)	τ_{ave} (ns)	PLQY (%)	Γ_{rad} (μs^{-1})	$\Gamma_{non\text{-}rad}$ (μs^{-1})
NCs-40 min	0.44	5.03	0.56	11.08	8.39	22.80	27.18	92.01
NCs-90 min	0.35	5.84	0.65	11.20	9.34	28.36	30.36	76.70

Fluorescence lifetime measurements revealed that these NCs exhibited shorter average lifetimes (**Figure 3.15a** and **Table 3.3**), indicating that more defects led to non-radiative recombination of charge carriers. Afterwards, I investigated the morphology and structure of NCs-40 min and NCs-90 min. The average size of the $CsSnI_3$ NCs synthesized at 40 min was 13.2±3.6 nm, while that of the sample synthesized at 90 min was 14.1±4.8nm (**Figure 3.15c, d**). It can be observed that the average size of these $CsSnI_3$ NCs is relatively less influenced by the reaction time, and both samples exhibited similar orthorhombic crystal structures (**Figure 3.15b**).

Finally, I explored the generalizability of this method. In addition to ZnI_2 as an iodine donor, other iodides such as ammonium iodide and metal iodide have also been reported to serve as precursors for CsI synthesis.[33, 42] Here, under the same reaction conditions as the optimal sample, I successfully obtained CsI NCs using I_2 as an iodine donor (denoted as CsI-I_2). Subsequently, I used these CsI NCs to prepare $CsSnI_3$ NCs. The average size of CsI NCs prepared using I_2 was found to be 17.1±2.8 nm (**Figure 3.16a**), and XRD spectra showed no impurity phases (**Figure 3.16b**). These CsI NCs did not exhibit significant differences compared to CsI NCs prepared with ZnI_2, except for a slightly more uniform size (**Figure 3.2b**).

As expected, the $CsSnI_3$ NCs (denoted as $CsSnI_3$-I_2) obtained after the phase transition of these CsI NCs also exhibited a uniform size and purity orthorhombic phase (**Figure 3.17a, b**). Examination of the photophysical properties of these $CsSnI_3$ NCs revealed that their PL emission peaks and absorption spectra were identical to those of $CsSnI_3$ obtained using ZnI_2 as the precursor(**Figure 3.17c**). Furthermore, these $CsSnI_3$ NCs exhibited a high PLQY of 27.6% (**Figure 3.17d**) , only slightly lower than that of

$CsSnI_3$ NCs obtained using ZnI_2 as the precursor (**Figure 3.6c**). This difference may be attributed to variations in the crystal quality and surface structure of CsI NCs prepared under different conditions. I believe that by fine-tuning reaction conditions such as temperature and precursor ratios, it may be possible to achieve $CsSnI_3$ NCs with similar high PLQY as those obtained using ZnI_2 as the precursor.

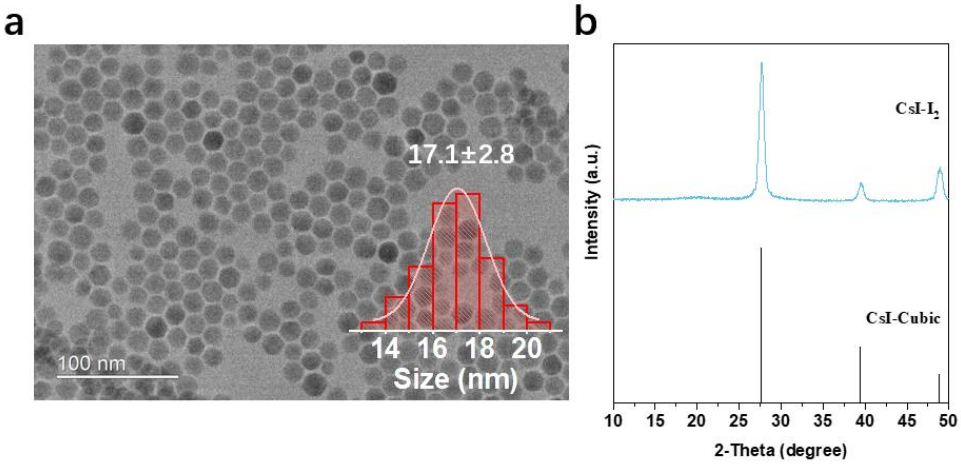

Figure 3.16 (a) TEM image and (b) XRD pattern of CsI NCs synthesized using I_2 as an iodine donor. The Inset in (a) shows the histograms of edge lengths of CsI NCs.

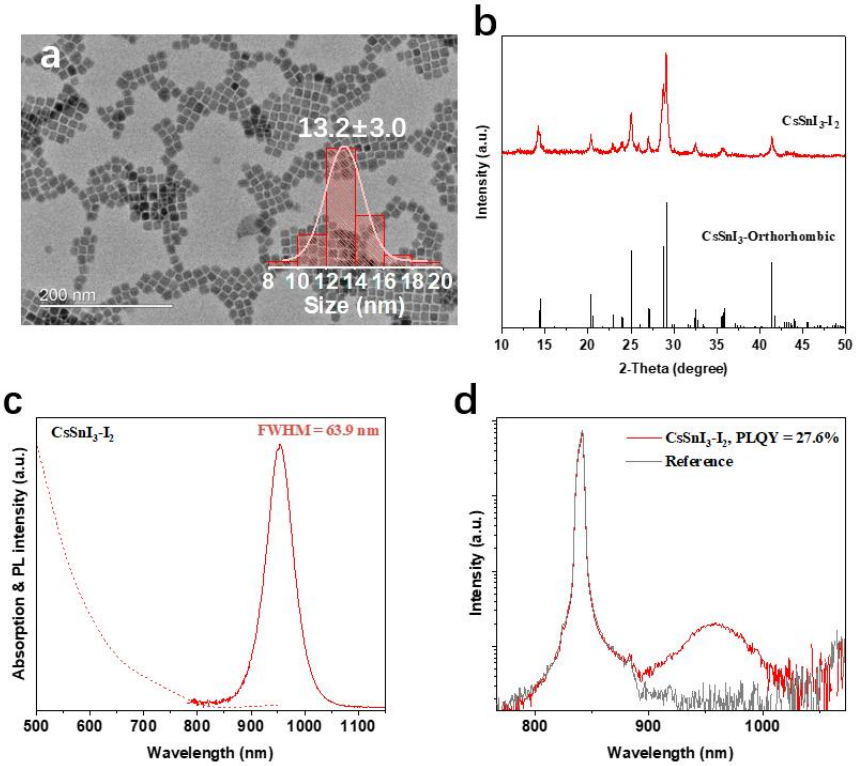

Figure 3.17 (a) TEM image, (b) XRD pattern, (c) PL & absorption spectrum, and (d) PLQY of $CsSnI_3$ NCs synthesized using CsI-I_2. The inset in (a) shows the histograms of edge lengths of $CsSnI_3$ NCs.

Then, I employed the same strategy to synthesize $CsSnBr_3$ NCs. $CsSnBr_3$ NCs were prepared by first synthesizing CsBr NCs using $ZnBr_2$ as the precursor, followed by reaction with $SnBr_2$-TOP precursor. The prepared CsBr NCs exhibited similar shapes to CsI, with average sizes of 13.7±3.1 nm (**Figure 3.18a**). HRTEM revealed a lattice spacing of 3.02 Å in these NCs, consistent with the cubic phase of CsBr (**Figure 3.18b**). Subsequent XRD analysis confirmed their cubic crystal structure (ICSD 236387), and no impurities (**Figure 3.18c**). Elemental composition analysis of CsBr NCs using SEM-EDS indicated a Cs-to-Br ratio of 1:1.17, suggesting a Br-rich surface structure in these CsBr NCs (**Figure 3.18d**).

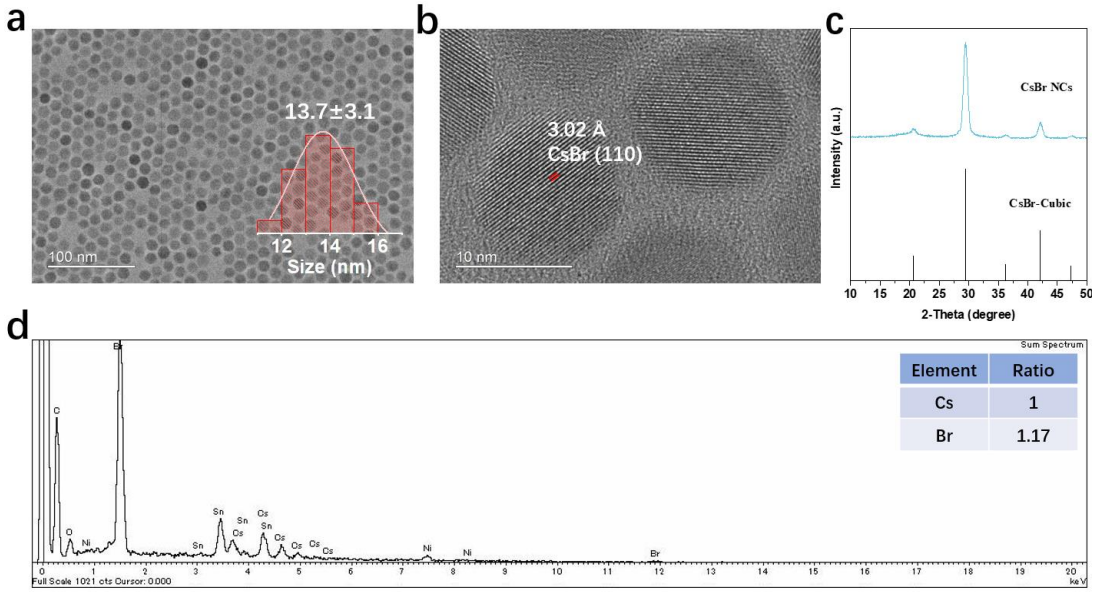

Figure 3.18 (a) TEM image, (b) HRTEM image, (c) XRD pattern of CsBr NCs. The inset in (a) shows the histograms of edge lengths of CsBr NCs. (d) SEM-EDS spectrum and elemental quantitative data of CsBr NCs.

$CsSnBr_3$ NCs obtained after the phase transition of CsBr NCs exhibited a uniform size distribution with an average size of 16.9±5.5 nm. Structural studies revealed that these $CsSnBr_3$ NCs exhibited a cubic phase structure (ICSD 4071) without the presence

of a second phase (**Figure 3.19a, c**). HRTEM also showed lattice spacings consistent with the cubic structure, where 4.10 Å corresponded to the (110) plane of cubic-phase $CsSnBr_3$ (**Figure 3.19b**). Elemental composition analysis of $CsSnBr_3$ NCs using SEM-EDS indicated a Cs-to-Sn-to-Br ratio of 1:1.12:3.92 (**Figure 3.19d**), demonstrating a surface rich in Sn and Br in these $CsSnBr_3$ NCs. Subsequent examination of the photophysical properties of these NCs showed fluorescence emission at 690 nm for $CsSnBr_3$ NCs (**Figure 3.19e**). However, their emission efficiency was very low, and effective PLQY data could not be obtained. Due to the larger optical bandgap of $CsSnBr_3$ compared to $CsSnI_3$, it is more prone to forming deep traps between the valence and conduction bands, leading to efficient non-radiative recombination of carriers. Nevertheless, I have demonstrated the universality of the method for synthesizing $CsSnX_3$ NCs using CsX NCs, laying the foundation for future research on $CsSnX_3$ NCs.

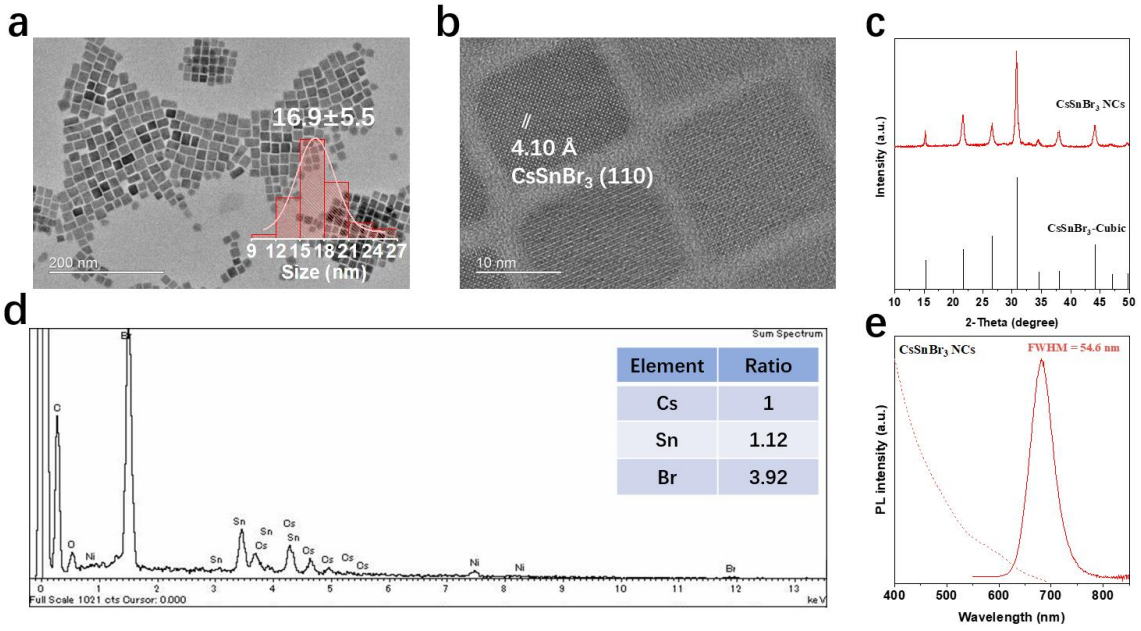

Figure 3.19 (a) TEM image, (b) HRTEM image, (c) XRD pattern of $CsSnBr_3$ NCs. The inset in (a) shows the histograms of edge lengths of $CsSnBr_3$ NCs. (d) SEM-EDS spectrum and elemental quantitative data, (e) PL and absorption spectrum of $CsSnBr_3$ NCs.

3.4 Conclusion

In summary, I have obtained size-uniform and tunable $CsSnX_3$ NCs by reacting CsX

NCs with SnX_2-TOP precursors. My obtained $CsSnI_3$ NCs exhibited the highest PLQY of up to 34.4% reported to date. I investigated the phase transition from CsI to $CsSnI_3$, confirming that the transition starts gradually from the surface of CsI NCs and spreads inward. Finally, I successfully synthesized $CsSnI_3$ NCs using other iodide precursors, demonstrating the generalization of the method. My study demonstrates the potential for developing highly efficient luminescent $CsSnX_3$ NCs and provides insights into pioneering new synthetic methods to obtain high-quality $CsSnX_3$ NCs.

Reference

(1) Protesescu, L.; Yakunin, S.; Bodnarchuk, M. I.; Krieg, F.; Caputo, R.; Hendon, C. H.; Yang, R. X.; Walsh, A.; Kovalenko, M. V. Nanocrystals of Cesium Lead Halide Perovskites ($CsPbX_3$, X = Cl, Br, and I): Novel Optoelectronic Materials Showing Bright Emission with Wide Color Gamut. *Nano Letters* **2015**, *15* (6), 3692-3696.

(2) Akkerman, Q. A.; D'Innocenzo, V.; Accornero, S.; Scarpellini, A.; Petrozza, A.; Prato, M.; Manna, L. Tuning the Optical Properties of Cesium Lead Halide Perovskite Nanocrystals by Anion Exchange Reactions. *Journal of the American Chemical Society* **2015**, *137* (32), 10276-10281.

(3) Akkerman, Q. A.; Nguyen, T. P.; Boehme, S. C.; Montanarella, F.; Dirin, D. N.; Wechsler, P.; Beiglböck, F.; Rainò, G.; Erni, R.; Katan, C. Controlling the nucleation and growth kinetics of lead halide perovskite quantum dots. *Science* **2022**, *377* (6613), 1406-1412.

(4) Jiang, Y.; Sun, C.; Xu, J.; Li, S.; Cui, M.; Fu, X.; Liu, Y.; Liu, Y.; Wan, H.; Wei, K.; et al. Synthesis-on-substrate of quantum dot solids. *Nature* **2022**, *612* (7941), 679-684.

(5) Swarnkar, A.; Marshall, A. R.; Sanehira, E. M.; Chernomordik, B. D.; Moore, D. T.; Christians, J. A.; Chakrabarti, T.; Luther, J. M. Quantum dot–induced phase stabilization of α-$CsPbI_3$ perovskite for high-efficiency photovoltaics. *Science* **2016**, *354* (6308), 92-95.

(6) Quan, L. N.; Rand, B. P.; Friend, R. H.; Mhaisalkar, S. G.; Lee, T.-W.; Sargent, E. H. Perovskites for Next-Generation Optical Sources. *Chemical Reviews* **2019**, *119* (12), 7444-7477.

(7) Dey, A.; Ye, J.; De, A.; Debroye, E.; Ha, S. K.; Bladt, E.; Kshirsagar, A. S.; Wang, Z.; Yin, J.; Wang, Y.; et al. State of the Art and Prospects for Halide Perovskite Nanocrystals. *ACS Nano* **2021**, *15* (7), 10775-10981.

(8) Akkerman, Q. A.; Rainò, G.; Kovalenko, M. V.; Manna, L. Genesis, challenges and opportunities for colloidal lead halide perovskite nanocrystals. *Nature Materials* **2018**,

17 (5), 394-405.

(9) Chen, Q.; Wu, J.; Ou, X.; Huang, B.; Almutlaq, J.; Zhumekenov, A. A.; Guan, X.; Han, S.; Liang, L.; Yi, Z.; et al. All-inorganic perovskite nanocrystal scintillators. *Nature* **2018**, *561* (7721), 88-93.

(10) Akkerman, Q. A.; Gandini, M.; Di Stasio, F.; Rastogi, P.; Palazon, F.; Bertoni, G.; Ball, J. M.; Prato, M.; Petrozza, A.; Manna, L. Strongly emissive perovskite nanocrystal inks for high-voltage solar cells. *Nature Energy* **2016**, *2* (2), 16194.

(11) Hao, M.; Bai, Y.; Zeiske, S.; Ren, L.; Liu, J.; Yuan, Y.; Zarrabi, N.; Cheng, N.; Ghasemi, M.; Chen, P.; et al. Ligand-assisted cation-exchange engineering for high-efficiency colloidal $Cs_{1-x}FA_xPbI_3$ quantum dot solar cells with reduced phase segregation. *Nature Energy* **2020**, *5* (1), 79-88.

(12) Mondal, N.; De, A.; Samanta, A. Achieving Near-Unity Photoluminescence Efficiency for Blue-Violet-Emitting Perovskite Nanocrystals. *ACS Energy Letters* **2019**, *4* (1), 32-39.

(13) Krieg, F.; Ochsenbein, S. T.; Yakunin, S.; ten Brinck, S.; Aellen, P.; Süess, A.; Clerc, B.; Guggisberg, D.; Nazarenko, O.; Shynkarenko, Y.; et al. Colloidal $CsPbX_3$ (X = Cl, Br, I) Nanocrystals 2.0: Zwitterionic Capping Ligands for Improved Durability and Stability. *ACS Energy Letters* **2018**, *3* (3), 641-646.

(14) Mondal, N.; De, A.; Samanta, A. Achieving near-unity photoluminescence efficiency for blue-violet-emitting perovskite nanocrystals. *ACS Energy Letters* **2018**, *4* (1), 32-39.

(15) Pan, J.; Shang, Y.; Yin, J.; De Bastiani, M.; Peng, W.; Dursun, I.; Sinatra, L.; El-Zohry, A. M.; Hedhili, M. N.; Emwas, A.-H.; et al. Bidentate Ligand-Passivated $CsPbI_3$ Perovskite Nanocrystals for Stable Near-Unity Photoluminescence Quantum Yield and Efficient Red Light-Emitting Diodes. *Journal of the American Chemical Society* **2018**, *140* (2), 562-565.

(16) Dutta, A.; Behera, R. K.; Pal, P.; Baitalik, S.; Pradhan, N. Near-unity photoluminescence quantum efficiency for all $CsPbX_3$ (X= Cl, Br, and I) perovskite

nanocrystals: a generic synthesis approach. *Angewandte Chemie International Edition* **2019**, *58* (17), 5552-5556.

(17) Yong, Z.-J.; Guo, S.-Q.; Ma, J.-P.; Zhang, J.-Y.; Li, Z.-Y.; Chen, Y.-M.; Zhang, B.-B.; Zhou, Y.; Shu, J.; Gu, J.-L.; et al. Doping-Enhanced Short-Range Order of Perovskite Nanocrystals for Near-Unity Violet Luminescence Quantum Yield. *Journal of the American Chemical Society* **2018**, *140* (31), 9942-9951.

(18) Koscher, B. A.; Swabeck, J. K.; Bronstein, N. D.; Alivisatos, A. P. Essentially Trap-Free CsPbBr3 Colloidal Nanocrystals by Postsynthetic Thiocyanate Surface Treatment. *Journal of the American Chemical Society* **2017**, *139* (19), 6566-6569.

(19) Pradhan, N. Tips and Twists in Making High Photoluminescence Quantum Yield Perovskite Nanocrystals. *ACS Energy Letters* **2019**, *4* (7), 1634-1638.

(20) Hudait, B.; Dutta, S. K.; Patra, A.; Nasipuri, D.; Pradhan, N. Facets Directed Connecting Perovskite Nanocrystals. *Journal of the American Chemical Society* **2020**, *142* (15), 7207-7217.

(21) Jellicoe, T. C.; Richter, J. M.; Glass, H. F. J.; Tabachnyk, M.; Brady, R.; Dutton, S. E.; Rao, A.; Friend, R. H.; Credgington, D.; Greenham, N. C.; et al. Synthesis and Optical Properties of Lead-Free Cesium Tin Halide Perovskite Nanocrystals. *Journal of the American Chemical Society* **2016**, *138* (9), 2941-2944.

(22) Chung, I.; Song, J.-H.; Im, J.; Androulakis, J.; Malliakas, C. D.; Li, H.; Freeman, A. J.; Kenney, J. T.; Kanatzidis, M. G. CsSnI3: Semiconductor or Metal? High Electrical Conductivity and Strong Near-Infrared Photoluminescence from a Single Material. High Hole Mobility and Phase-Transitions. *Journal of the American Chemical Society* **2012**, *134* (20), 8579-8587.

(23) Tao, S.; Schmidt, I.; Brocks, G.; Jiang, J.; Tranca, I.; Meerholz, K.; Olthof, S. Absolute energy level positions in tin- and lead-based halide perovskites. *Nature Communications* **2019**, *10* (1), 2560.

(24) Huang, L.-y.; Lambrecht, W. R. Electronic band structure, phonons, and exciton binding energies of halide perovskites $CsSnCl_3$, $CsSnBr_3$, and $CsSnI_3$. *Physical Review B*

2013, *88* (16), 165203.

(25) Wong, A. B.; Bekenstein, Y.; Kang, J.; Kley, C. S.; Kim, D.; Gibson, N. A.; Zhang, D.; Yu, Y.; Leone, S. R.; Wang, L.-W.; et al. Strongly Quantum Confined Colloidal Cesium Tin Iodide Perovskite Nanoplates: Lessons for Reducing Defect Density and Improving Stability. *Nano Letters* **2018**, *18* (3), 2060-2066.

(26) Chen, J.-K.; Zhang, B.-B.; Liu, Q.; Shirahata, N.; Mohammed, O. F.; Bakr, O. M.; Sun, H.-T. Advances and Challenges in Tin Halide Perovskite Nanocrystals. *ACS Materials Letters* **2021**, *3* (11), 1541-1557.

(27) Chen, M.-Y.; Lin, J.-T.; Hsu, C.-S.; Chang, C.-K.; Chiu, C.-W.; Chen, H. M.; Chou, P.-T. Strongly Coupled Tin-Halide Perovskites to Modulate Light Emission: Tunable 550–640 nm Light Emission (FWHM 36–80 nm) with a Quantum Yield of up to 6.4%. *Advanced Materials* **2018**, *30* (20), 1706592.

(28) Wang, Y.; Sun, X.; Shivanna, R.; Yang, Y.; Chen, Z.; Guo, Y.; Wang, G.-C.; Wertz, E.; Deschler, F.; Cai, Z.; et al. Photon Transport in One-Dimensional Incommensurately Epitaxial CsPbX3 Arrays. *Nano Letters* **2016**, *16* (12), 7974-7981.

(29) Wu, Z.; Chen, J.; Mi, Y.; Sui, X.; Zhang, S.; Du, W.; Wang, R.; Shi, J.; Wu, X.; Qiu, X.; et al. All-Inorganic $CsPbBr_3$ Nanowire Based Plasmonic Lasers. *Advanced Optical Materials* **2018**, *6* (22), 1800674.

(30) Zheng, Z.; Wang, X.; Shen, Y.; Luo, Z.; Li, L.; Gan, L.; Ma, Y.; Li, H.; Pan, A.; Zhai, T. Space-Confined Synthesis of 2D All-Inorganic $CsPbI_3$ Perovskite Nanosheets for Multiphoton-Pumped Lasing. *Advanced Optical Materials* **2018**, *6* (22), 1800879.

(31) Han, M.; Sun, J.; Peng, M.; Han, N.; Chen, Z.; Liu, D.; Guo, Y.; Zhao, S.; Shan, C.; Xu, T.; et al. Controllable Growth of Lead-Free All-Inorganic Perovskite Nanowire Array with Fast and Stable Near-Infrared Photodetection. *The Journal of Physical Chemistry C* **2019**, *123* (28), 17566-17573.

(32) Liu, Q.; Yin, J.; Zhang, B.-B.; Chen, J.-K.; Zhou, Y.; Zhang, L.-M.; Wang, L.-M.; Zhao, Q.; Hou, J.; Shu, J.; et al. Theory-Guided Synthesis of Highly Luminescent Colloidal Cesium Tin Halide Perovskite Nanocrystals. *Journal of the American Chemical*

Society **2021**, *143* (14), 5470-5480.

(33) Shamsi, J.; Dang, Z.; Ijaz, P.; Abdelhady, A. L.; Bertoni, G.; Moreels, I.; Manna, L. Colloidal CsX (X = Cl, Br, I) Nanocrystals and Their Transformation to CsPbX3 Nanocrystals by Cation Exchange. *Chemistry of Materials* **2018**, *30* (1), 79-83.

(34) Liu, Q.; Yin, J.; Zhang, B.-B.; Chen, J.-K.; Zhou, Y.; Zhang, L.-M.; Wang, L.-M.; Zhao, Q.; Hou, J.; Shu, J. Theory-guided synthesis of highly luminescent colloidal cesium tin halide perovskite nanocrystals. *Journal of the American Chemical Society* **2021**, *143* (14), 5470-5480.

(35) Mahesh, K. P. O.; Chang, C.-Y.; Hong, W.-L.; Wen, T.-H.; Lo, P.-H.; Chiu, H.-Z.; Hsu, C.-L.; Horng, S.-F.; Chao, Y.-C. Lead-free cesium tin halide nanocrystals for light-emitting diodes and color down conversion. *RSC Advances* **2020**, *10* (61), 37161-37167.

(36) Kang, C.; Rao, H.; Fang, Y.; Zeng, J.; Pan, Z.; Zhong, X. Antioxidative Stannous Oxalate Derived Lead-Free Stable $CsSnX_3$ (X=Cl, Br, and I) Perovskite Nanocrystals. *Angewandte Chemie International Edition* **2021**, *60* (2), 660-665.

(37) Li, Y.; Wang, D.; Yang, Y.; Ding, C.; Hu, Y.; Liu, F.; Wei, Y.; Liu, D.; Li, H.; Shi, G.; et al. Stable Inorganic Colloidal Tin and Tin–Lead Perovskite Nanocrystals with Ultralong Carrier Lifetime via Sn(IV) Control. *Journal of the American Chemical Society* **2024**, *146* (5), 3094-3101.

(38) Zhang, J.; Zhu, X.; Wang, M.; Hu, B. Establishing charge-transfer excitons in 2D perovskite heterostructures. *Nature Communications* **2020**, *11* (1), 2618.

(39) Lanzetta, L.; Marin-Beloqui, J. M.; Sanchez-Molina, I.; Ding, D.; Haque, S. A. Two-Dimensional Organic Tin Halide Perovskites with Tunable Visible Emission and Their Use in Light-Emitting Devices. *ACS Energy Letters* **2017**, *2* (7), 1662-1668.

(40) Kore, B. P.; Zhang, W.; Hoogendoorn, B. W.; Safdari, M.; Gardner, J. M. Moisture tolerant solar cells by encapsulating 3D perovskite with long-chain alkylammonium cation-based 2D perovskite. *Communications Materials* **2021**, *2* (1), 100.

(41) Chen, Y.; Wang, Z.; Wei, Y.; Liu, Y.; Hong, M. Exciton Localization for Highly

Luminescent Two-Dimensional Tin-Based Hybrid Perovskites through Tin Vacancy Tuning. *Angewandte Chemie International Edition* **2023**, *62* (18), e202301684.

(42) Song, W.; Wu, X.; Di, Q.; Xue, T.; Zhu, J.; Quan, Z. Morphologically controlled synthesis of ionic cesium iodide colloidal nanocrystals and electron beam-induced transformations. *RSC Advances* **2018**, *8* (33), 18519-18524.

Chapter 4 Synthesis of Highly Luminescent Cesium Tin Halide Perovskite Nanocrystal via Controlled Ion Exchange

4.1 Introduction

Interest in tin halide perovskite nanocrystals (NCs) as alternatives to lead halide NCs has grown. [1-4]Although there has been some progress in the synthesis of tin halide perovskite NCs, effective methods to enhance their luminescence efficiency have not been identified.[1, 5-10] The photoluminescence (PL) properties of tin halide perovskite NCs are highly sensitive to synthesis conditions and composition.[7, 8] Reports indicate lower photoluminescence quantum yields (PLQY) for these perovskites, even with the use of the hot-injection method, which is known for easily synthesizing highly luminescent perovskite NCs.[1, 6, 11, 12] Therefore, this method fails to effectively suppress defects in tin halide perovskite NCs, which can act as charge trapping centers and reduce the luminescence efficiency.

Theoretical studies suggest that tin vacancy (V_{Sn}) defects are the most likely deep defects in tin halide perovskite NCs. Synthesis in a tin-rich environment can effectively reduce V_{Sn}. Following this strategy, Liu et al. synthesized $CsSnI_3$ NCs with a PLQY of 18.4%,[7] while Li et al. achieved a PLQY of 35% for tin-rich tin-lead alloy NCs and a PLQY of 10.7% for uniformly shaped cubic $CsSnI_3$ NCs under synthesis conditions with a SnI_2/Cs ratio of 6.7/1.[8] This emphasizes the importance of the ratio of chemical reactants, especially the amount of tin source.

Additionally, controlling the nucleation and growth of metal halide perovskite NCs is crucial for their optoelectronic properties.[13-16] In my work in Chapter 2, I have discovered that the reactivity of precursors during the synthesis of tin halide perovskite NCs is a crucial factor leading to a significant variation in luminescence efficiency.[17] It is essential not only to consider the effects of chemical synthesis reaction conditions, such as temperature and ratios, but also to pay special attention to the selection of raw materials, such as the combination of different tin and iodine sources. In addition, various methods

have been reported to modulate the growth process of tin halide perovskite materials. Wang et al. introduced pseudohalogen ammonium thiocyanate (NH_4SCN) during the growth of $FASnI_3$, achieving control over the nucleation and crystallization process.[18] The addition of NH_4SCN effectively separated the nucleation and crystalline growth of $FASnI_3$, resulting in higher-quality $FASnI_3$ films and achieving a 9.41% power conversion efficiency in tin-based metal halide perovskite solar cells. Similarly, Meng et al. utilized hydrogen bonding to delay the crystallization rate of $FASnI_3$, obtaining tin halide perovskite with fewer defects, significantly enhancing the efficiency and stability of tin halide perovskite solar cells.[19] Additionally, fluoro-aniline isomers have been reported for modulating the crystallization process of $FASnI_3$ films.[20] The significant impact of nucleation and growth rates on tin halide perovskites is primarily attributed to their low formation activation energy and low formation energy of vacancy defect in their structure.[6, 21-24] Rapid crystallization growth often results in poor crystalline quality, morphology degradation, and higher defect density.[20, 22] Among various reported synthesis methods for cesium tin halide perovskite NCs, the nucleation and growth processes typically complete within one minute or even a few seconds.[12, 21, 25-28] This limitation may account for the challenge in obtaining high-quality $CsSnX_3$ NCs. Therefore, I speculate that slowing down the growth rate of NCs appropriately may be the key to obtaining high-quality $CsSnX_3$ NCs.

Although in Chapter 3, I successfully synthesized the most efficient $CsSnI_3$ NCs to date based on the phase transition method of Sn replacing Cs ions in CsI, there is still further potential to enhance the luminescence efficiency. The key feature of this method is the slow phase transition process. Considering this, perhaps by reasonably altering the ion exchange rate, slightly accelerating or decelerating the phase transition process, I may have the opportunity to further increase the PLQY of $CsSnI_3$ NCs. Therefore, in this chapter, I introduced Tin(II) 2-ethylhexanoate [$Sn(Oct)_2$] as an additional tin source to influence the cation exchange rate during the synthesis process of CsI to $CsSnI_3$ NCs, enabling us to obtain $CsSnI_3$ NCs with a PLQY approaching 50% and excellent stability.

Through quasi in-situ absorption spectroscopy studies of the phase transition process, I found that the addition of $Sn(Oct)_2$ not only accelerated the rate of phase transition from CsX to $CsSnI_3$ but also influenced the behavior of the phase transition reaction, resulting in $CsSnI_3$ NCs with fewer surface defects. Finally, by using Oleylammonium Bromide (OAmBr) as the bromide ion source and employing anion exchange technology, I obtained highly luminescent $CsSnI_{2.1}Br_{0.9}$ nanowires through $CsSnI_3$ phase transition, extending the emission range from 950 nm to 892 nm. This convenient method of enhancing the optical properties of $CsSnX_3$ NCs by controlling cation and anion exchange paves the way for their synthesis and application in optoelectronic devices.

4.2 Experimental Section

4.2.1 Chemicals and experimental

Chemicals

Cesium carbonate (Cs_2CO_3, Sigma, 99.995%), tin 2-ethylhexanoate ($Sn(Oct)_2$, Sigma, 92.5-100.0%), tin(II) iodide (SnI_2, Sigma, 99.999%), Zinc iodide (ZnI_2, Wako, 99.5%), Tin(II) Oxide (SnO, Wako, 99.9%), Oleylammonium Iodide (OAmI, Xi'an Yuri, 98%), 1-octadecene (ODE, Alfa, 90%), oleylamine (OAm, Thermo Fisher, 80–90%), oleic acid (OA, Sigma, 90%), tri-n-octylphosphine (TOP, Thermo Fisher, 90%), Toluene (Wako, 99.5%), n-hexane (Wako, ≥96.0%), Ethanol (Wako, 99.5%), Hydrobromic Acid (HBr, 47% weight), Ethyl Acetate (Wako, 99.5%) were used without purification unless otherwise noted.

Preparation of the Cs precursor.

In an Ar-filled glovebox, Cs_2CO_3 (0.6436 g, 0.988 mmol) and OA (10 mL) were mixed in a 20 mL glass bottle. Subsequently, the mixture was heated at 120 °C and stirred at 400 rpm for 120 minutes (min) to obtain a colorless Cs precursor solution. Afterwards, it was used for the synthesis of CsI NCs.

Preparation of the ZnI_2 precursor.

In an Ar-filled glovebox, ZnI_2 (0.0639 g, 0.2 mmol), OA (1 mL), OAm (1 mL), and

OED (2 mL) were mixed in a 20 mL glass bottle. In this case, ODE needs to be vacuum dried at 120°C for 2 hours before use. Subsequently, the mixture was heated at 120 °C and stirred at 400 rpm for 30 min to obtain a colorless ZnI_2 precursor solution. Afterwards, it was used for the synthesis of CsI NCs.

Synthesis of CsI NCs.

In a topical synthesis, ZnI_2 precursor was heated at 60 °C and stirred at 400 rpm for 20 min on the heating plate, and then 0.55 mL amount of Cs precursor was swiftly injected into the ZnI_2 precursor. After 5 min of reaction, the reaction mixture was cooled to room temperature using a water bath. To collect the CsI NCs, the solution was then centrifuged at 12000 rpm for 5 min. After centrifugation, the supernatant was discarded and the NCs were redispersed in 4 mL toluene.

Preparation of the SnI_2-TOP precursor.

In an Ar-filled glovebox, SnI_2 (0.1863 g, 0.5 mmol) and TOP (0.335 mL) were mixed in a 9 mL glass bottle. Subsequently, the mixture was heated at 120 °C and stirred at 300 rpm for 15 min to obtain a dark yellow clear solution. Subsequently, the obtained solution was cooled to room temperature and then injected with 0.665 mL of toluene and uniformly mixed at room temperature. Afterwards, the SnI_2-TOP precursor (~0.5 mmol/mL) was used for the synthesis of $CsSnI_3$ NCs.

Preparation of the dilute solution of $Sn(Oct)_2$.

I dispersed 0.332 mL (1.0 mmol) of $Sn(Oct)_2$ into 0.668 mL of toluene to prepare diluted $Sn(Oct)_2$ for the synthesis of $CsSnI_3$ NCs. The concentration of dilute solution of $Sn(Oct)_2$ is about 1mmol/mL.

Synthesis of $CsSnI_3$ NCs

In an Ar-filled glovebox, 1.2 mL of CsI NCs solution was load in a 9 mL glass bottle, and then heated at 95 °C and stirred at 200 rpm on the heating plate. After preheating for 45 s, 0.33 mL amount of SnI_2-TOP precursor was swiftly injected into the CsI NCs solution. After injecting the SnI_2-TOP precursor, 160 μL of $Sn(Oct)_2$ was injected into the mixture after another 10 seconds. After 60 min of reaction, the ensuing crude solution

was allocated to a centrifuge tube. After centrifugation at 500 rpm for 1 min, the precipitates were removed, and then the supernatant was centrifugate at 12000 rpm for 5 min, this time the supernatant was removed. After repeating the previous step one more time, the resultant $CsSnI_3$ NCs precipitates were collected and used for the characterization.

Synthesis of Oleylammonium Bromide (OAmBr)

In a 200 mL three-necked flask, 9.9 g (37 mmol, based on 80% purity) of oleylamine was mixed with 100 mL of ethanol. The mixture was cooled to 0°C in an ice-water bath, followed by the dropwise addition of 76 mmol of HBr (8.8 mL, 47% weight). After the addition, the solution was stirred for 20 hours under an argon atmosphere. Subsequently, the solvent was removed under reduced pressure in a rotary evaporator. The resulting crude product was dispersed in the minimum amount of ethyl acetate and sonicated for 1 min. The obtained solution was then centrifuged at 7000 rpm for 5 min. This process was repeated until obtaining a colorless supernatant and a white powdery precipitate.[29]

Synthesis of Sn-Oleate

To synthesize Sn-Oleate, 1.618g of SnO powder and 8 mL of OA were load in a three-neck flask, and then stirred at 400 rpm under an argon flow at 220°C for 3 hours. After cooling, 5 mL of hexane was added to dilute the mixture product, followed by centrifugation at 12000 rpm for 10 min to collect the suspension. Subsequently, hexane was evaporated under anaerobic conditions, leaving behind yellowish waxy Sn-Oleate.

Preparation of the dilute solution of Sn-Oleate.

I dispersed 0.41g (1.0 mmol) of Sn-Oleate into 0.562 mL of toluene to prepare diluted Sn-Oleate for the synthesis of $CsSnI_3$ NCs. The concentration of dilute solution of Sn-Oleate is about 1 mmol/mL.

Synthesis of $CsSnI_3$ NCs using Sn-Oleate

The method for synthesizing $CsSnI_3$ using Sn-Oleate is the same as the method using $Sn(Oct)_2$, except that an equivalent volume of Sn-Oleate dilute solution is used instead of the $Sn(Oct)_2$ dilute solution.

Synthesis of $CsSn(I/Br)_3$ NWs by anion exchange

To synthesize $CsSn(I/Br)_3$ NWs, I conducted an anion exchange reaction using $CsSnI_3$ NCs and OAmBr. The anion exchange reaction took place at room temperature by mixing $CsSnI_3$ NCs with a specific ratio of OAmBr in toluene. Specifically, I prepared a 40 mg/mL solution of OAmBr in toluene and then added 50 μL of the OAmBr solution to the $CsSnI_3$ hexane at room temperature. After the anion exchange reaction for 2 hours, the mixture was centrifuged at 12000 rpm for 5 min to remove the suspension. The precipitate of $CsSn(I/Br)_3$ was then dispersed in hexane for subsequent analysis.

Synthesis of $CsSnI_3$ NWs

The synthesis of $CsSnI_3$ NWs was similar to that of $CsSn(I/Br)_3$ NWs, where the OAmBr was replaced with OAmI.

4.2.2 Characterization

Structure, Morphology, Fourier-transform infrared spectroscopy (FTIR) Characterization, X-ray photoelectron spectroscopy (XPS), Scanning electron microscopy (SEM) and energy dispersive X-ray spectroscopy (EDS).

XRD data were recorded on a MiniFlex 600 diffractometer (Rigaku) with Cu Kα radiation (λ = 1.5418 Å). The NCs were dispersed in hexane to form a concentrated NCs solution, and the solution was dropped on an anaerobic sample holder for the XRD measurements. TEM samples were prepared by dropping a dilute NC-hexane solution onto a TEM copper grid and dried in an Ar-filled glovebox. TEM images were measured by a JEM-2100F (JEOL) microscope operated at 200 kV. FTIR spectra were recorded using a Jasco 4100 FTIR spectrometer. Elemental analysis and chemical bonding were studied by XPS, the samples for the XPS analysis are drop-casted on the silicon substrate. For SEM-EDS, the samples were coated onto conductive adhesive and subjected to gold sputter coating prior to SEM-EDS measurement of the samples

Luminescence and Absorption Characterization.

The PL spectra were measured by a NanoLog Horiba Jovin Yvon spectrofluorometer with a continuous 450 W xenon lamp. The absolute PLQYs were measured by a C9920-03G system equipped with a 150 W xenon lamp (Hamamatsu Photonics). The PL decays were obtained with a time-correlated single photon counting lifetime spectroscopy system (NanoLog, Horiba Jovin Ybon), equipped with a pulse laser (λ_{em} = 726 nm). The absorption spectra were measured by a UV-vis-NIR spectrophotometer (V-770, JASCO).

Detailed method for the calculation of the average lifetime, radiative, and nonradiative recombination rates.

Using PLQYs and average lifetimes, I evaluated the radiative and nonradiative decay rates based on the following equations:

$$\tau_{ave} = (A_1\tau_1^2 + A_2\tau_2^2 + \cdots)/(A_1\tau_1 + A_2\tau_2 + \cdots) \quad (1)$$

$$\Gamma_{rad} = \frac{\mathrm{PLQY}}{\tau_{ave}} \quad (2)$$

$$\Gamma_{non-rad} = \frac{1}{\tau_{ave}} - \Gamma_{rad} = \frac{1 - \mathrm{PLQY}}{\tau_{ave}} \quad (3)$$

where A_i (i=1, 2, and 3) and τ_i (i=1, 2, and 3) are the amplitudes and the corresponding fitted lifetimes, respectively, τ_{ave} is the average lifetime of the samples, and Γ_{rad} and $\Gamma_{non\text{-}rad}$ are the radiative and non-radiative recombination rates, respectively.

4.3 Results and discussion

The synthesis of $CsSnI_3$ NCs follows an improved version of the method used in Chapter 3 for synthesizing $CsSnX_3$ (X=Br or I) NCs. Specifically, I first prepared the SnI_2-TOP precursor by reacting SnI_2 with tri-n-octylphosphine (TOP). Then, I dispersed tin(II) 2-ethylhexanoate [$Sn(Oct)_2$] in toluene to prepare a diluted solution of $Sn(Oct)_2$, hereafter referred to as $Sn(Oct)_2$ unless otherwise specified. Additionally, CsI NCs were synthesized using ZnI_2 and cesium oleate. In Chapter 3, $CsSnI_3$ NCs was synthesized by injecting the SnI_2-TOP precursor into the CsI NCs solution. To further enhance the PLQY of $CsSnI_3$ NCs, in this study, I additionally injected the $Sn(Oct)_2$ into the reaction mixture for $CsSnI_3$ synthesis, 10 seconds after the injection of SnI_2-TOP. **Figure 4.1a** shows the chemical structure of $Sn(Oct)_2$, a chemical commonly used in the synthesis of perovskite

materials.[17,21] By introducing Sn(Oct)2 during the synthesis of $CsSnI_3$ NCs, I successfully obtained higher quality $CsSnI_3$ NCs. **Figure 4.1b** depicts the PLQY of $CsSnI_3$ NCs with different amounts of $Sn(Oct)_2$ added (140, 160, and 180 μL). The results show a clear trend of increase followed by decrease in PLQY with increasing $Sn(Oct)_2$ quantity (**Figure 4.1b**). When 140 μL of $Sn(Oct)_2$ was used, the PLQY of $CsSnI_3$ NCs was only 25.3%. It is exciting that with an increase in $Sn(Oct)_2$ to 160 μL, the PLQY of $CsSnI_3$ NCs improved to 49.7%, the highest efficiency reported to date for $CsSnI_3$ NCs. However, when 180 μL of $Sn(Oct)_2$ was used, the PLQY of $CsSnI_3$ NCs was decrease to 38.4% (**Figure 4.1b**). Subsequently, I examined the PL spectra of these $CsSnI_3$ NCs, which exhibited similar emissions at 953 nm, and their absorption spectra showed no significant differences. Completely consistent PL peak position and PL peak half-maximum width (FWHM) suggesting that there might not be significant differences in structure and size distribution of these NCs (**Figure 4.1c**). XRD analysis confirmed that all these $CsSnI_3$ NCs exhibited the same orthorhombic crystal structure without the detection of a second phase (**Figure 4.1d**).

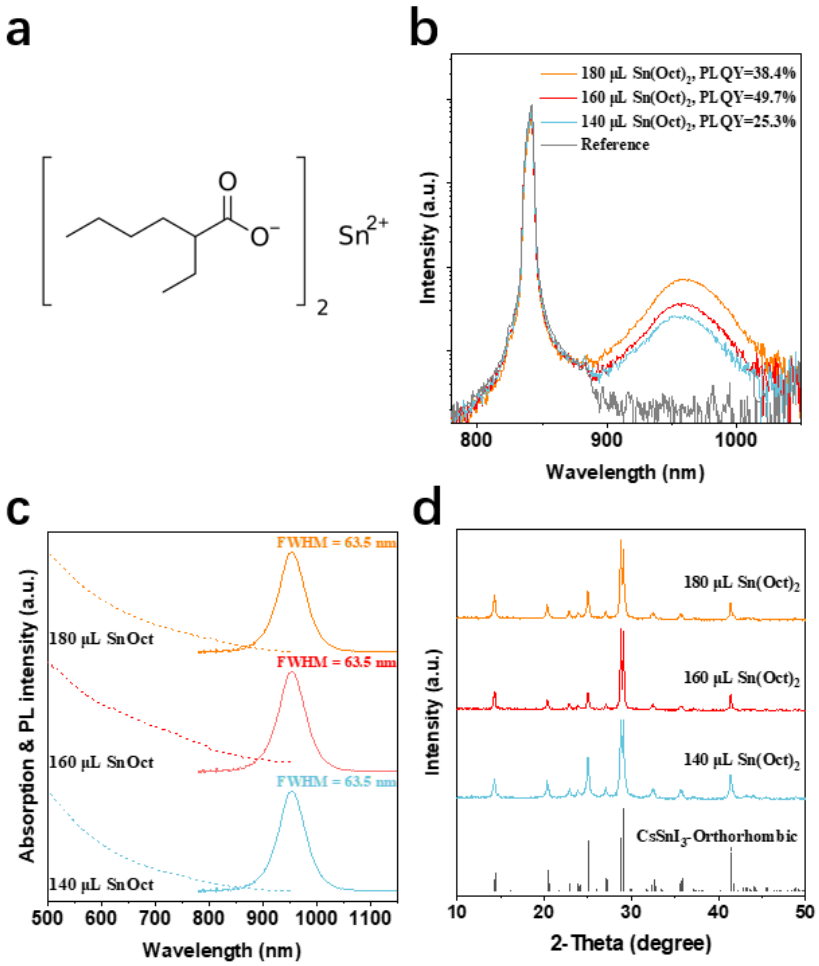

Figure 4.1 (a) schematic chemical structure of $Sn(Oct)_2$. (b) PLQY at 840 nm excitation, (c) PL and absorption spectra, and (d) XRD patterns of $CsSnI_3$ NCs synthesized using different amount of $Sn(Oct)_2$.

Figure 4.2 presents the transmission electron microscope (TEM) images of these $CsSnI_3$ NCs, revealing similar size and distribution of these NCs, which also explains why they did not show PL peak shifts or broadening (**Figure 4.2a-c**). The average sizes of $CsSnI_3$ NCs corresponding to 140, 160, and 180 µL $Sn(Oct)_2$ were 15.1±3.5, 14.7±3.9, and 14.3±4.8 nm, respectively. Excluding statistical errors, they did not exhibit particularly significant differences. High-resolution TEM (HRTEM) of these $CsSnI_3$ NCs showed lattice spacings of 6.20, 3.06 Å, and 3.09 Å, corresponding to the(020), (202), and (040) planes of the orthorhombic phase $CsSnI_3$, respectively (**Figure 4.2d-f**). Scanning electron microscopy (SEM) coupled to an energy dispersive X-Ray

spectrometer (EDS) analysis revealed that in $CsSnI_3$ NCs with a PLQY of 49.7%, the Cs:Sn:I ratio was determined to be 1:1.17:3.45 (**Figure 4.3**), indicating an enrichment of tin and iodine on the surface of these NCs.

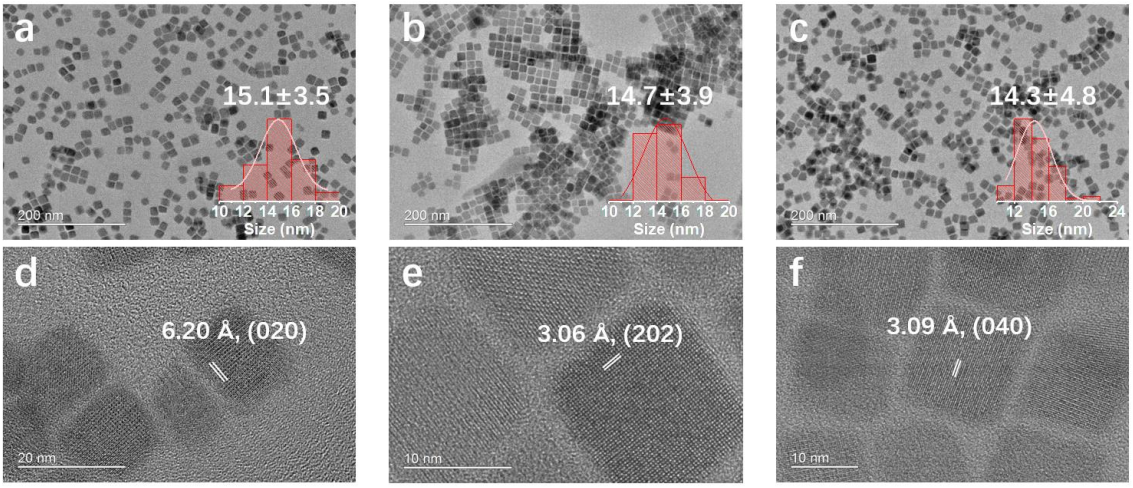

Figure 4.2 (a-c) TEM images and (d-f) HRTEM images of $CsSnI_3$ NCs synthesized using 140 μL, 160 μL, and 180 μL of $Sn(Oct)_2$, respectively. The insets in (a-c) display the size distribution plot of the corresponding $CsSnI_3$ NCs.

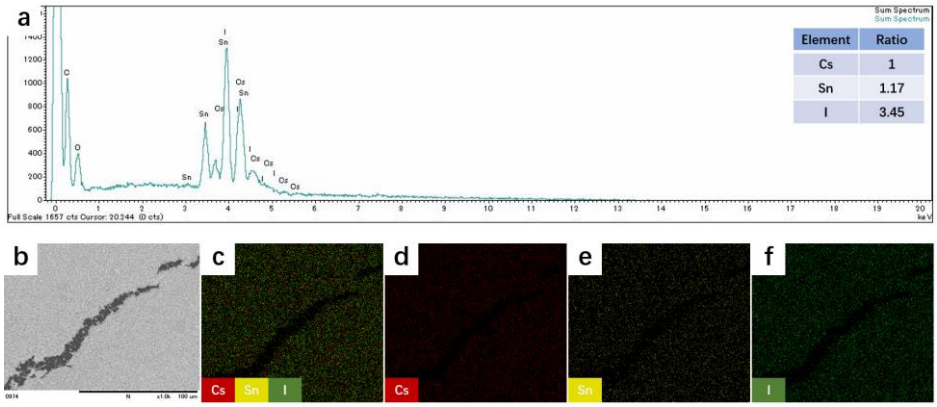

Figure 4.3 (a) SEM-EDS spectrum and elemental quantitative data, (b) SEM image, and (c-f) EDS mapping analysis of $CsSnI_3$ NCs synthesized using 160 μL of $Sn(Oct)_2$.

To further insights into the photophysical properties of these $CsSnI_3$ NCs, I conducted time-resolved PL measurements in order to obtain more information about the transient evolution of photoexcited carriers. **Figure 4.4a** and **Table 4.1** depict the

fluorescence lifetime curves of $CsSnI_3$ NCs with different amounts of $Sn(Oct)_2$. All lifetimes were fitted using a double-exponential function after subtracting the influence of the pulse laser. The results reveal that insufficient or excessive $Sn(Oct)_2$ leads to a significant reduction in the fluorescence lifetime of $CsSnI_3$ NCs, with the longest average fluorescence lifetime (τ_{ave}) observed for $CsSnI_3$ NCs corresponding to 160μL of $Sn(Oct)_2$, measuring 34.58 ns. The longer fluorescence lifetime indicates that photoexcited carriers are not rapidly captured by traps, thereby preventing non-radiative recombination. This suggests that these $CsSnI_3$ NCs have a lower defect density, demonstrating that the introduction of $Sn(Oct)_2$ in reasonable amounts suppresses the generation of defects leading to non-radiative recombination in $CsSnI_3$ NCs. Thus, the amount of $Sn(Oct)_2$ is crucial for obtaining tin halide perovskite NCs with low defect densities. Furthermore, I investigated the stability of the optimal sample (**Figure 4.4b**). I stored the hexane solution of $CsSnI_3$ NCs in an Ar-filled glovebox and measured the PLQY of these NCs after a period of time. The results indicate that these $CsSnI_3$ NCs not only exhibit efficient luminescence but also possess better stability compared to previously reported highly luminescent $CsSnI_3$ NCs. After storage for 5 days, their PLQY remained at 80% of the initial value.

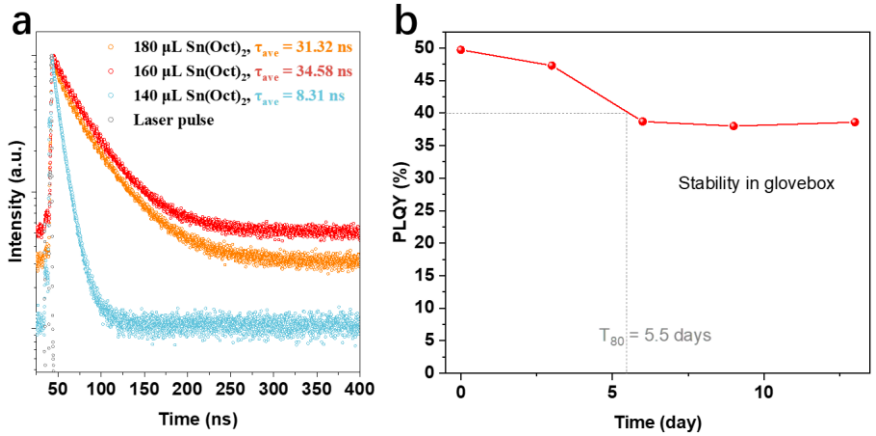

Figure 4.4 (a) PL decay and average lifetimes (τ_{ave}) of $CsSnI_3$ NCs synthesized using different amount of $Sn(Oct)_2$. (b) PLQY stability in Ar-filled glovebox of $CsSnI_3$ NCs synthesized using 160 μL of $Sn(Oct)_2$. The gray dashed line in the figure indicates the time corresponding to when the PLQY drops to 80% of its original intensity.

Table 4.1. Fitting results of PL decay curves, τ_{ave}, PLQYs, radiative (Γ_{rad}) and nonradiative ($\Gamma_{non\text{-}rad}$) decay rates of $CsSnI_3$ NCs. Note that the decays were fitted with a double-exponential function.

Sample	A_1	τ_1 (ns)	A_2	τ_2 (ns)	τ_{ave} (ns)	PLQY (%)	Γ_{rad} (μs^{-1})	$\Gamma_{non\text{-}rad}$ (μs^{-1})
180 μL $Sn(Oct)_2$	0.32	10.54	0.68	41.14	31.32	38.40	12.26	19.67
160 μL $Sn(Oct)_2$	0.05	12.55	0.95	38.05	34.58	49.70	14.37	14.55
140 μL $Sn(Oct)_2$	0.31	3.35	0.69	10.59	8.31	25.30	30.45	89.89

After determining the mount of $Sn(Oct)_2$, I investigated the effect of the injection timing of $Sn(Oct)_2$ on $CsSnI_3$ NCs. I attempted two different methods for adding $Sn(Oct)_2$: mixing $Sn(Oct)_2$ with SnI_2-TOP and injecting them together (labeled as $Sn(Oct)_2$-0 s), and delaying the addition of $Sn(Oct)_2$ until 20 s after injecting SnI_2-TOP (labeled as $Sn(Oct)_2$-20 s). PLQY measurements of the obtained $CsSnI_3$ NCs, I observed a significant decrease in PLQY when $Sn(Oct)_2$ was added either too early or too late (**Figure 4.5a**). The PLQY of $CsSnI_3$ NCs for $Sn(Oct)_2$-0 s and $Sn(Oct)_2$-20 s were 44.0% and 39.8%, respectively. I compared their crystal structures and optical properties. TEM images revealed similar sizes for both, with average sizes of 14.5±4.2 nm and 14.3±3.7 nm, and similar size distributions (**Figure 4.5b, c**). XRD analysis showed lattice spacings consistent with the orthorhombic phase of $CsSnI_3$ NCs, and no impurity (**Figure 4.5d**). Both $Sn(Oct)_2$-0 s and $Sn(Oct)_2$-20 s $CsSnI_3$ NCs demonstrate indistinguishable morphology and structure. Consequently, their PL and absorption spectra also remain virtually identical. Both $CsSnI_3$ NCs exhibit a PL emission peak at 953 nm, characterized by a FWHM of 62.5 nm (**Figure 4.6a**). Just as observed in the experimental outcomes involving different amount of $Sn(Oct)_2$, improper timing of $Sn(Oct)_2$ injection also led to abbreviated fluorescence lifetimes, suggesting a rise in defect density of $CsSnI_3$ NCs. (**Figure 4.6b** and **Table 4.2**). Thus, controlling the injection timing of $Sn(Oct)_2$ also plays a crucial role in the optical performance of $CsSnI_3$ NCs.

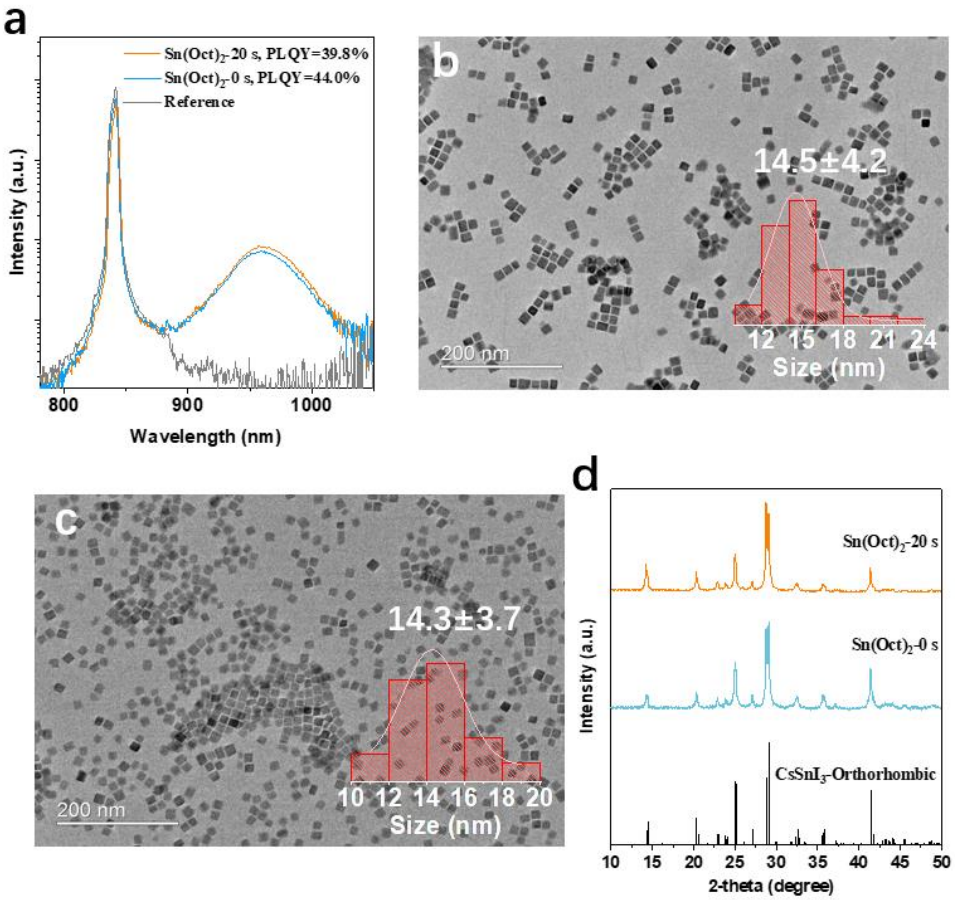

Figure 4.5 (a) PLQYs at 840 nm excitation of $CsSnI_3$ NCs synthesized with $Sn(Oct)_2$ injection at 0 s and 20 s. TEM image of $CsSnI_3$ NCs synthesized with $Sn(Oct)_2$ injection at 0 s (b) and 20 s (c). Insets show the size distribution plot of corresponding $CsSnI_3$ NCs. (d) XRD patterns of $CsSnI_3$ NCs synthesized with $Sn(Oct)_2$ injection at 0 s and 20 s.

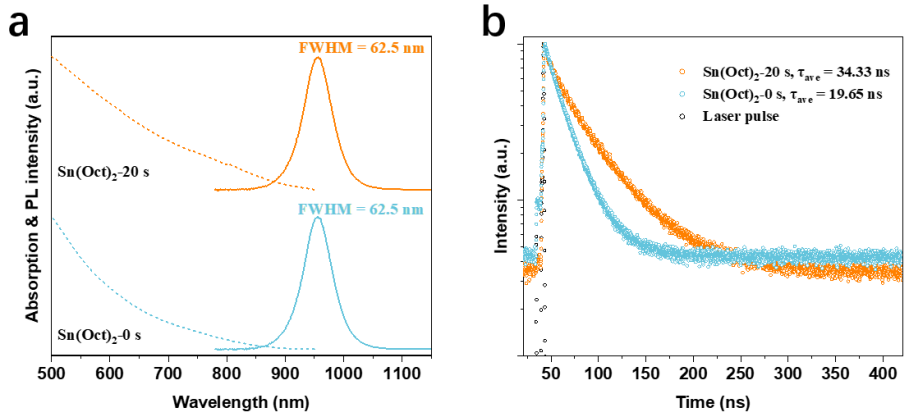

Figure 4.6 (a) PL & absorption spectra, and (b) PL decay and average lifetimes (τ_{ave}) of $CsSnI_3$ NCs synthesized with $Sn(Oct)_2$ injection at 0 s and 20 s.

Table 4.2. Fitting results of PL decay curves, τ_{ave}, PLQYs, radiative (Γ_{rad}) and nonradiative ($\Gamma_{non\text{-}rad}$) decay rates of $CsSnI_3$ NCs. Note that the decays were fitted with a double-exponential function.

Sample	A_1	τ_1 (ns)	A_2	τ_2 (ns)	τ_{ave} (ns)	PLQY (%)	Γ_{rad} (μs^{-1})	$\Gamma_{non\text{-}rad}$ (μs^{-1})
$Sn(Oct)_2$-20 s	0.29	9.60	0.71	44.25	34.44	39.80	11.56	17.48
$Sn(Oct)_2$-0 s	0.10	5.38	0.90	21.27	19.65	44.00	22.39	28.50

To clarify the effect of $Sn(Oct)_2$ on $CsSnI_3$ NCs, I compared the phase transition process from CsI NCs to $CsSnI_3$ NCs with and without the addition of $Sn(Oct)_2$. Through in situ PL spectroscopy during the phase transition reaction, I observed that $Sn(Oct)_2$ led to different phase transition rates and behaviors. As shown in **Figure 4.7**, following the introduction of $Sn(Oct)_2$, the phase transition reaction from CsI to $CsSnI_3$ exhibited a significant PL emission peak at 950 nm as early as 120 s (**Figure 4.7a**). By the time the reaction progressed to 220 s, strong PL emission was observed exclusively at 950 nm, indicating complete transformation of CsI NCs into $CsSnI_3$ NCs by approximately 220 s under these conditions. In contrast, the comparison sample without $Sn(Oct)_2$ showed PL emission at 950 nm only around 250 s, with even stronger emission observed around 360 s (**Figure 4.7b**). These results demonstrate that the addition of $Sn(Oct)_2$ significantly accelerates the reaction rate during the transformation of CsI to $CsSnI_3$.

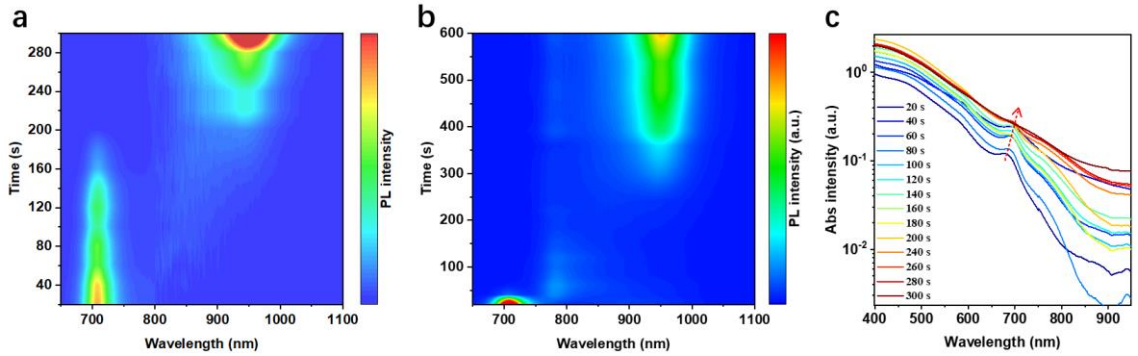

Figure 4.7 Mapping chart illustrating the change in PL of the reaction mixture over time with (a) and without (b) $Sn(Oct)_2$. (c) Absorption spectra of the reaction mixture over time with $Sn(Oct)_2$. The dotted orange line in (c) is drawn to guide the eye.

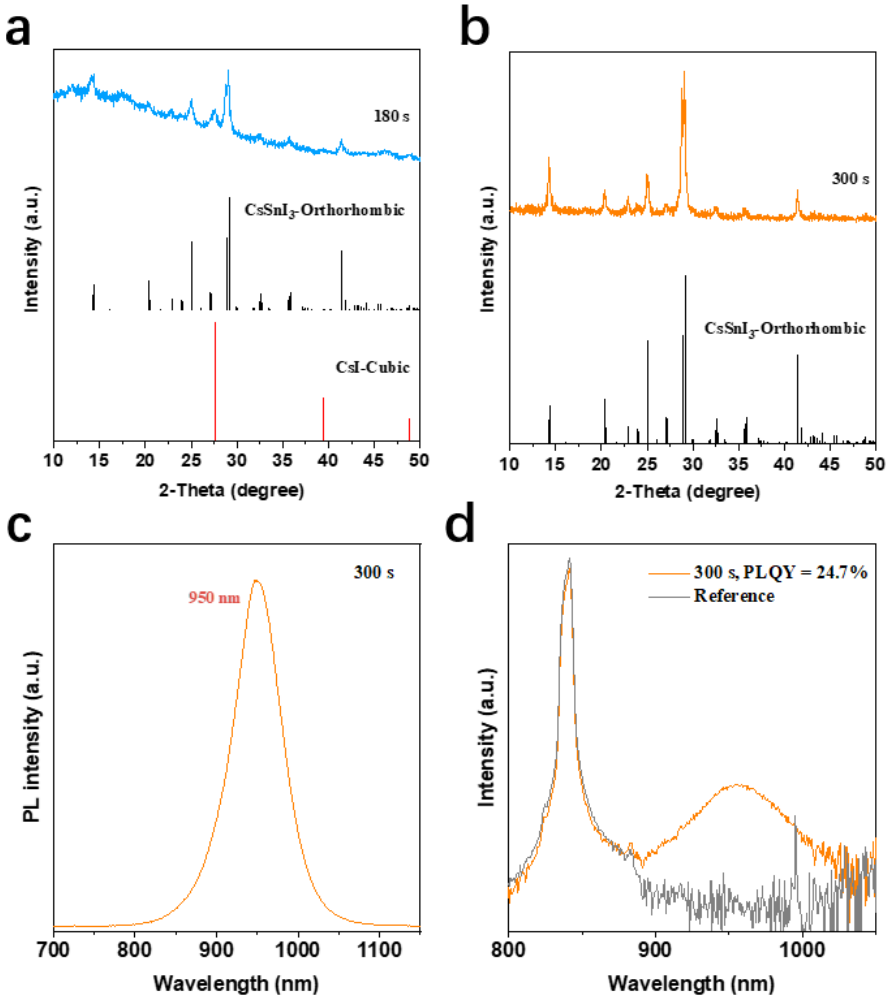

Figure 4.8 XRD patterns of the products separated at 180 s (a), and 300 s (b) of the reaction with $Sn(Oct)_2$. (c) PL spectrum and (d) PLQY at 840 nm excitation of the products separated at 300 s of the reaction involving $Sn(Oct)_2$.

Furthermore, comparing the X-ray diffraction (XRD) patterns of the products obtained after 180 s and 300 s of reaction, I observed that in the system containing $Sn(Oct)_2$, only a small amount of CsI remained around 180 s (**Figure 4.8a**), with the remaining CsI completely converting to orthorhombic-phase $CsSnI_3$ within 300 s (**Figure 4.8b**). At this stage, PL emission was only observed at 950 nm with a relatively symmetric peak shape (**Figure 4.8c**). The PLQY of $CsSnI_3$ NCs obtained after purification at 300 s was measured to be 24.7%. (**Figure 4.8d**).

It is noteworthy that the presence of $Sn(Oct)_2$ significantly influences the changes

observed in the PL peaks at 710 nm and 780 nm (**Figure 4.7a, b**). In the sample with $Sn(Oct)_2$ addition, there is a stronger and more sustained PL emission peak at 710 nm, persisting until around 200s into the reaction before disappearing entirely. Correspondingly, the absorption spectrum shows a pronounced excitonic absorption peak at 695 nm, following a similar trend as the PL peak at 710 nm, gradually red-shifting and weakening until it vanishes entirely towards the end of the reaction (**Figure 4.7c**). As demonstrated in Chapter 3, both the PL peak at 710 nm and the absorption peak at 695 nm originate from the two-dimensional perovskite $(R\text{-}NH_3^+)_2Cs_{n-1}Sn_nI_{3n+1}$ ($n > 1$). Regarding the PL peak at 780 nm, in the sample with $Sn(Oct)_2$ addition, it disappears completely after the completion of the phase transition. Based on the findings of Chapter 3, I have established that the emission at 780 nm after the completion of the phase transition originates from small-sized $CsSnI_3$ NCs. This suggests that $Sn(Oct)_2$ either impedes the formation or causes the decomposition of these small-sized $CsSnI_3$ NCs.

Based on the foregoing information, it can be inferred that $Sn(Oct)_2$ significantly expedites the transformation of CsI NCs into $CsSnI_3$ NCs. Additionally, through a comparison of the in-situ PL spectra under conditions with and without $Sn(Oct)_2$, plausible hypotheses can be formulated regarding the mechanism by which $Sn(Oct)_2$ influences the synthesis process of $CsSnI_3$ NCs. During the phase transition reaction, following the injection of the SnI_2-TOP precursor, Sn^{2+} ions instigate the phase transition by displacing Cs ions on the surface of CsI NCs, commencing from the surface. The surface of CsI NCs is iodine-rich, suggesting the potential presence of numerous oleylammonium cation ($R\text{-}NH_3^+$) coordinating with I ions to form $R\text{-}NH_3I$ salt, which resides on the surface of CsI NCs. Upon the introduction of the SnI_2-TOP precursor, Sn^{2+} ions must initially disrupt the surface $R\text{-}NH_3I$ layer of CsI NCs to substitute Cs^+ ions within CsI NCs. Once detached from CsI NCs, $R\text{-}NH_3^+$ readily associates with Cs^+ and SnI_2-TOP to generate two-dimensional perovskite $(R\text{-}NH_3^+)_2Cs_{n-1}Sn_nI_{3n+1}$, manifesting PL emission at 710 nm. In the case of $Sn(Oct)_2$, its addition accelerates the detachment of the surface $R\text{-}NH_3I$ layer of CsI, leading to enhanced generation of two-dimensional

perovskite. Comparative experiments have revealed $Sn(Oct)_2$'s disruptive impact on both CsI and $CsSnI_3$ (**Figure 4.9a, b**), potentially inducing significant detachment of the surface R-NH_3I layer of CsI during the initial phase of transition. The disruptive effect of $Sn(Oct)_2$ on the NCs surface at the onset of reaction evidently introduces more active sites on the surface of the NCs, thereby accelerating the reaction rate. In this case, the relatively increased reaction rate is advantageous for $CsSnI_3$ NCs. In short, the altered phase transition rate undoubtedly influences the defect density within the crystal structure of $CsSnI_3$ NCs, presenting an avenue for synthesizing $CsSnI_3$ NCs with high-efficiency luminescence through this controllable reaction rate. However, $Sn(Oct)_2$ presence also destabilizes small-sized $CsSnI_3$ NCs, hindering the persistence of PL emission at 780 nm after the reaction is completed.

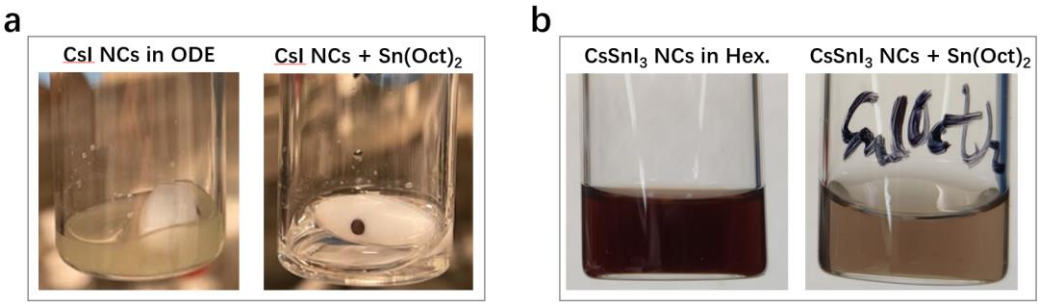

Figure 4.9 (a) Photographs of the CsI NCs dispersed in 1-octadecene (ODE) solution and their mixture with $Sn(Oct)_2$. $Sn(Oct)_2$ leads to the clarification of the CsI colloidal solution, indicating the decomposition of CsI NCs. (b) Photographs of the $CsSnI_3$ NCs dispersed in hexane solution and their mixture with $Sn(Oct)_2$. $Sn(Oct)_2$ leads to the gradual fading of the dark brown $CsSnI_3$ NCs colloidal solution, indicating the decomposition of $CsSnI_3$ NCs.

Next, I further investigated the reaction mechanism of the transformation from CsI NCs to $CsSnI_3$ NCs in the presence of $Sn(Oct)_2$. I investigated the NCs at an intermediate stage of the reaction using HRTEM. The $CsSnI_3$/CsI NCs with a core-shell structure were clearly observed. As shown in **Figure 4.10**, the lattice spacing on the surface of the NCs was measured to be 3.13 Å, corresponding to the (004) crystal plane of the orthorhombic phase $CsSnI_3$. Meanwhile, the spacing between internal lattice fringes measured 2.32 Å,

noticeably smaller than that of the surface lattice fringes, corresponding to the (200) crystal plane of the cubic phase CsI. Hence, these NCs, still in an intermediate state of transformation, comprised a core-shell structure with a $CsSnI_3$ shell, approximately 3 nm thick, enveloping a CsI nanocore with a diameter of around 8 nm. The presence of these core-shell structured NCs suggests that the reaction between CsI NCs and the SnI_2-TOP and $Sn(Oct)_2$ precursors begins at the surface of CsI and gradually propagates inward.

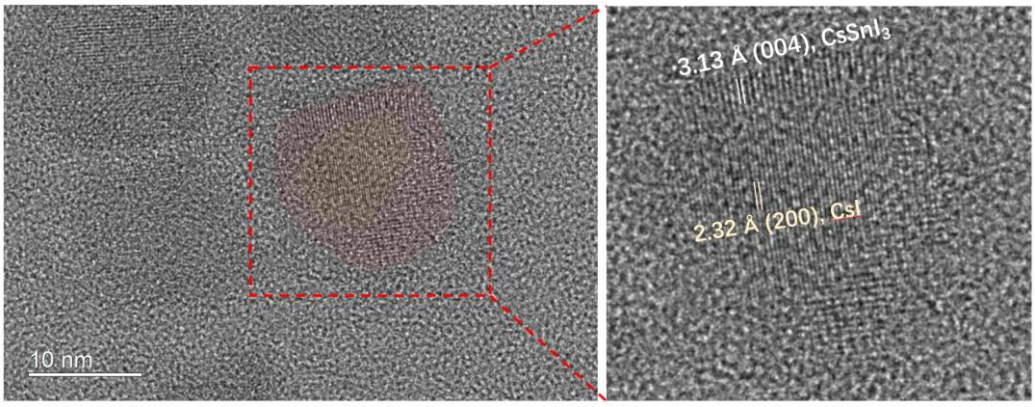

Figure 4.10 The HRTEM image and its partial enlargement reveal the intermediate product during the transformation of CsI NCs to $CsSnI_3$ NCs. It is evident that these NCs exhibit core-shell $CsSnI_3$/CsI NCs.

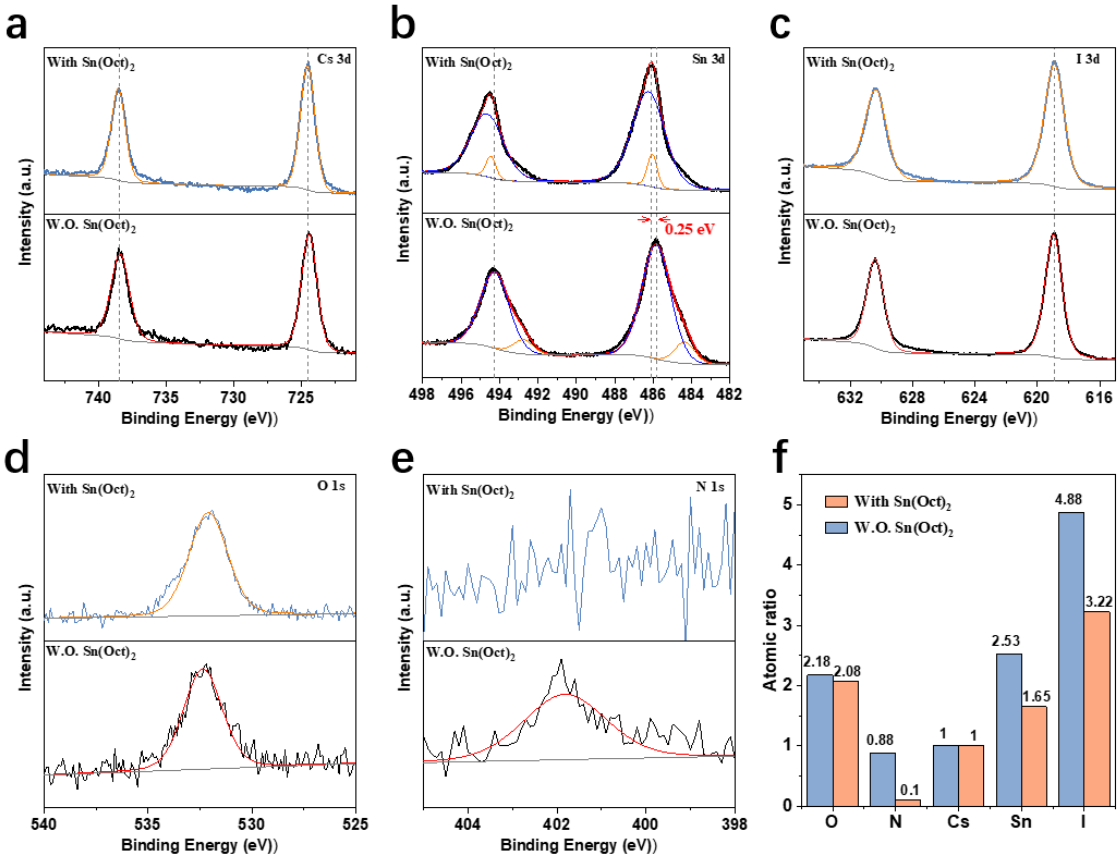

Figure 4.11 The XPS spectra and elemental analysis of $CsSnI_3$ NCs synthesis with and without the involvement of Sn(Oct)2. (a)–(e) The high-resolution XPS profiles of Cs (3d), Sn (3d), I (3d), O (1s), N (1s) energy states of $CsSnI_3$ NCs. (f) The analysis results of the elemental content corresponding to (a)–(e), normalized to the Cs content.

To elucidate the enhancement of PLQY in $CsSnI_3$ NCs after the addition of $Sn(Oct)_2$, I carried out X-ray photoelectron spectroscopy (XPS) studies on the surface structure of $CsSnI_3$ NCs synthesized with and without $Sn(Oct)_2$. As shown in **Figure 4.11**, high-resolution XPS spectra of Cs, Sn, I, O, and N elements are presented for $CsSnI_3$ NCs synthesized with and without $Sn(Oct)_2$. The XPS spectra of Cs and I in both types of $CsSnI_3$ show no significant changes in peak shape or peak position. However, it is noteworthy that the introduction of $Sn(Oct)_2$ resulted in a 0.25 eV shift of the Sn 3d peak to higher energy, indicating the presence of more coordinated states of I around Sn on the $CsSnI_3$ NCs surface. I fitted the peaks of Sn 3d and found two signals of Sn. The weak peak obtained from fitting is attributed to the surface Sn of $CsSnI_3$ NCs, which is under-

coordinated. The strong peak can be attributed to subsurface Sn, which has a batter coordination than surface Sn but still not perfect $[SnI_6]^{4-}$ octahedra. It can be clearly observed that the introduction of $Sn(Oct)_2$ caused all peaks to shift to higher energy, with the surface Sn showing the most significant shift, indicating a significant increase in the coordination number of these Sn atoms. Therefore, the addition of $Sn(Oct)_2$ suppresses the formation of I vacancies in the $[SnI_6]^{4-}$ octahedra,[30, 31] leading to $CsSnI_3$ NCs with a more perfect surface structure, thus resulting in a significant increase in PLQY.

Based on the high-resolution XPS spectra, I also calculated the elemental composition of these $CsSnI_3$ NCs, normalized to the Cs content and reflected in **Figure 4.11f**. It is evident that all $CsSnI_3$ NCs samples exhibit a pronounced enrichment of Sn and I on their surfaces. The surplus of Sn and I, indicates that these Sn-I complexes, deficient in Cs, exist on the surface of $CsSnI_3$ NCs. The introduction of $Sn(Oct)_2$ leads to a significant reduction in these Sn-I complexes, by approximately 50% as calculated based on the change in Sn content. Moreover, the decrease in non-perovskite Sn-I complexes implies a relative increase in the abundance of perfect $[SnI_6]^{4-}$ octahedra, resulting in the high-energy shift of the Sn 3d peak observed in **Figure 4.11b**. Additionally, both in the perovskite and non-perovskite structures, I atoms exhibit sufficient coordination with a substantial amount of Sn. Therefore, no shift is observed in the I 3d peak in the XPS spectra.

The XPS spectra of O 1s and N 1s reflect the presence of organic ligands on the surface of $CsSnI_3$ NCs. Obtaining smooth curves for these spectra is challenging due to weak signals, but I can still analyze changes in the content of O and N elements. In the synthesis of $CsSnI_3$ NCs, the organic ligands mainly consist of oleic acid, oleylamine, and 2-ethylhexanoic acid introduced by $Sn(Oct)_2$. Firstly, the O element represents variations in oleic acid and 2-ethylhexanoic acid containing carboxylate groups. However, the O element content did not increase with the addition of $Sn(Oct)_2$; instead, it showed a slight decrease, indicating no significant change in carboxylic acid ligands on the surface of $CsSnI_3$ NCs. Secondly, the variation of N elements from oleylamine is observed, and

there is a significant decrease in oleylamine ligands on the surface of $CsSnI_3$ NCs with the addition of $Sn(Oct)_2$. This is consistent with my speculation that $Sn(Oct)_2$ can accelerate the reaction rate by causing the detachment of $R\text{-}NH_3^+$ from the surface of NCs during the synthesis of $CsSnI_3$.

Furthermore, Fourier transform infrared spectroscopy (FTIR) reveals a significant reduction in the organic ligands on the surface of synthesized $CsSnI_3$ compared to CsI NCs, yet $Sn(Oct)_2$ does not induce changes in the types of surface ligands on $CsSnI_3$ NCs. As depicted in **Figure 4.12**, FTIR measurements were conducted on samples of approximately equal quantities. The FTIR spectra of the synthesized $CsSnI_3$ NCs, with and without the use of $Sn(Oct)_2$, show comparable peak intensities, both notably weaker than those observed in CsI NCs.

The intense vibrational peaks around 2850 cm^{-1} in the FTIR spectra are attributed to the stretching vibrations of C-H bonds,[32-35] which are associated with the alkyl chains of the oleic acid and oleylamine ligands. Carboxylate group vibrations typically occur in the 1500 to 1700 cm^{-1} range,[32, 34, 35] and the introduction of $Sn(Oct)_2$ did not introduce additional signals corresponding to carboxylate groups in this spectral region. Therefore, the $Sn(Oct)_2$ does not induce changes in the types of carboxylic acid ligands on the surface of $CsSnI_3$ NCs, indicating the absence of 2-ethylhexanoic acid on the surface of $CsSnI_3$ NCs. This further suggests that $Sn(Oct)_2$ introduction enhances PLQY by modulating the reaction rate, thereby mitigating internal structural defects in $CsSnI_3$ NCs.

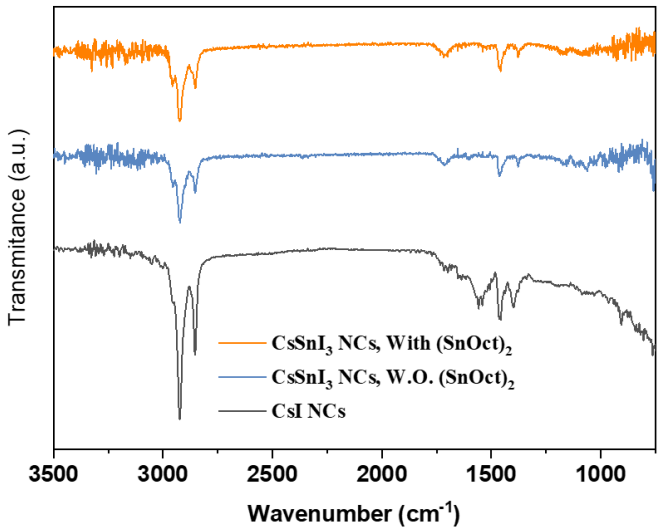

Figure 4.12 The FTIR spectra of CsI NCs and $CsSnI_3$ NCs synthesized with or without the involvement of $Sn(Oct)_2$.

$Sn(Oct)_2$, a tin salt comprising a short-chain carboxylic acid (diethylhexanoate), is commonly employed as a tin source in syntheses.[21] To rule out the influence of $Sn(Oct)_2$-induced changes in the tin-to-iodine ratio on the enhancement of PLQY in $CsSnI_3$ NCs, comparative experiments were conducted. Initially, I endeavored to synthesize $CsSnI_3$ NCs under identical conditions using equimolar stannous oleate (Sn-Oleate) instead of $Sn(Oct)_2$ (The resulting $CsSnI_3$ NCs is labeled NCs-Sn-Oleate). Surprisingly, this led to a substantial PLQY decrease to 15.7% (**Figure 4.13a**), despite maintaining identical crystal structure, morphology, PL, and absorption spectra as those obtained using $Sn(Oct)_2$ (**Figure 4.13b-d**). The only noticeable difference is that the size of the NCs-Sn-Oleate has slightly decreased (**Figure 4.1b**), with an average size of 13.5 ± 2.9 nm (**Figure 4.13d**). To further explore the Sn-to-I ratio's influence, I introduced oleylammonium iodide (OAmI) as an iodine source during synthesis of $CsSnI_3$ NCs (The resulting $CsSnI_3$ NCs is labeled NCs-OAmI), proportionate to 5% of the $Sn(Oct)_2$ amount. However, the PLQY of the resultant $CsSnI_3$ NCs plummeted to 33.2% (**Figure 4.13a**) . Notably, these NCs exhibited analogous size, morphology, crystal structure, PL, and absorption spectra (**Figure 4.11b, c,** and **e**). Evidently, even minor changes in $CsSnI_3$ NCs' crystal structure

resulted in profound PLQY variations across all NCs, highlighting the paramount role of reaction kinetics in $CsSnI_3$ NCs synthesis.

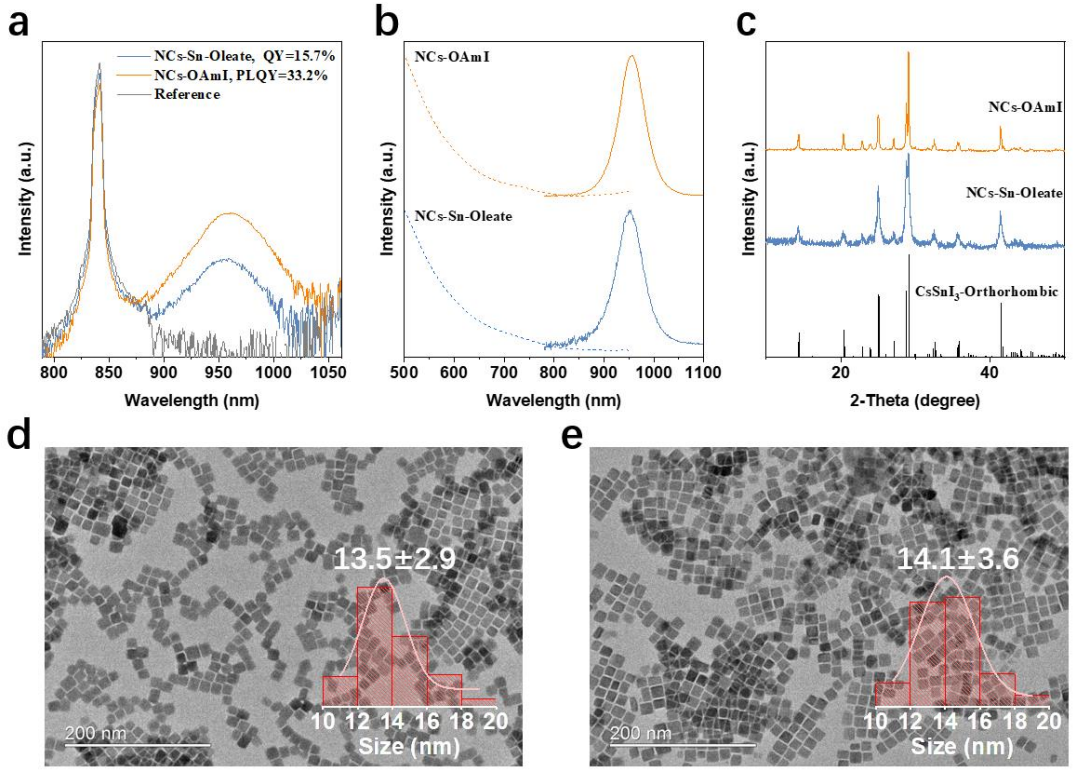

Figure 4.13 (a) PLQYs at 840 nm excitation, (b) PL & absorption spectra, and (c) XRD patterns of $CsSnI_3$ NCs synthesized using Sn-Oleate and $CsSnI_3$ NCs synthesized with the involvement of OAmI. (d) TEM image of $CsSnI_3$ NCs synthesized using Sn-Oleate. (e) TEM image of $CsSnI_3$ NCs synthesized with the involvement of OAmI. Insets in the (d) and (e) show the size distribution plot of corresponding $CsSnI_3$ NCs.

Next, I attempted to obtain other high-quality tin halide perovskite NCs based on the efficient luminescence of $CsSnI_3$ NCs. In addition to the cation exchange method described in this chapter for synthesizing $CsSnI_3$, anion exchange is more commonly used for synthesizing mixed-halide ABX_3 (A = Cs, Methylamine, or Formamidine ; B = Pb, Sn, or other transition metals; X = Cl, Br, I) perovskites, as introduced in the chapter 1. Here, I attempted to synthesize $CsSn(I/Br)_3$ mixed-halide perovskite NCs through anion exchange using oleylammonium bromide (OAmBr) and highly luminescent $CsSnI_3$ NCs. Specifically, I prepared a 40 mg/mL solution of OAmBr in toluene and then added 50 μL

of the OAmBr solution to the $CsSnI_3$ hexane at room temperature. After a 2-hour anion exchange reaction, I successfully synthesized $CsSn(I/Br)_3$ NCs (**Figure 4.14a**) (see Experimental Section for detailed synthesis methods).

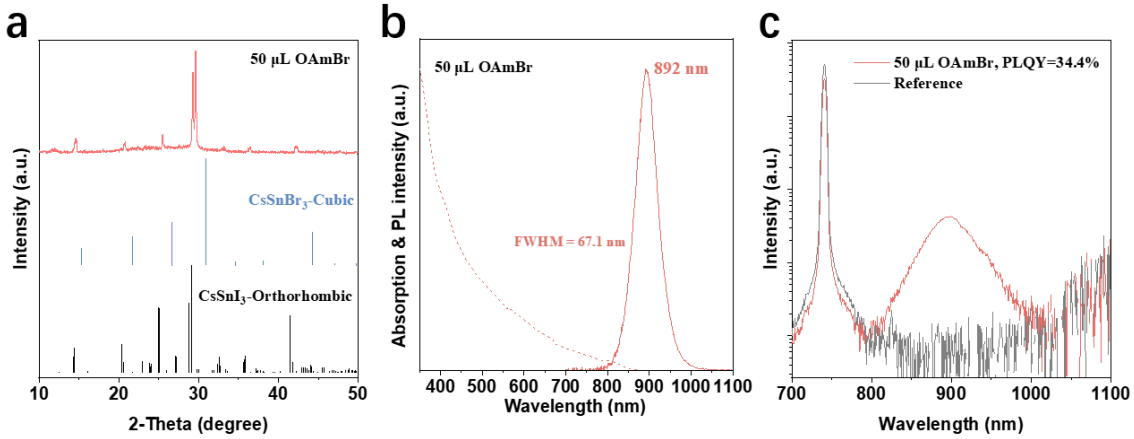

Figure 4.14 (a) XRD pattern, (b) PL & absorption spectra, and (c) PLQY at 740 nm excitation of $CsSn(I/Br)_3$ NCs.

As expected, the PL spectra exhibit a blue shift with the introduction of Br due to the expansion of the band gap (**Figure 4.14b**). And, a strong emission peak is observed at 892 nm, which represents a 60 nm blue shift relative to $CsSnI_3$ NCs. Moreover, the PLQY of 34.4% (**Figure 4.14c**), surpassing that of all previously reported $CsSn(I/Br)_3$ nanomaterials or bulk materials.[1, 5, 21, 36] Subsequently, I examined the $CsSn(I/Br)_3$ NCs corresponding to 50 µL OAmBr using TEM. Interestingly, these $CsSn(I/Br)_3$ NCs did not form nanocubes like $CsSnI_3$; instead, they formed nanowires (NWs) reaching micrometer lengths. The width of these $CsSn(I/Br)_3$ NWs is approximately 13 nm, very close to the size of $CsSnI_3$ NCs (**Figure 4.15a**). The appearance of these width dimensions is not coincidental; through high-resolution TEM, I discovered that these NWs are assembled from individual $CsSnI_3$ NCs along one direction. As shown in **Figure 4.15b**, the assembling NWs are clearly visible.

To investigate how $CsSn(I/Br)_3$ NWs are formed, I employed the same post-treatment method using OAmI instead of OAmBr for $CsSnI_3$ NCs. The results showed that $CsSnI_3$ NCs also underwent self-assembly to form $CsSnI_3$ NWs with an average

width of about 13 nm (**Figure 4.16a**). This suggests that the self-assembly of $CsSnI_3$ NCs is unrelated to Br ions and is likely caused by the oleylammonium cation. Through HRTEM, I found that these $CsSnI_3$ NCs fuse and grow along the [110] direction (**Figure 4.16b**), possibly due to the introduction of oleylammonium cations as surfactants, increasing the reactivity of the $CsSnI_3$ NCs (110) crystal facets.

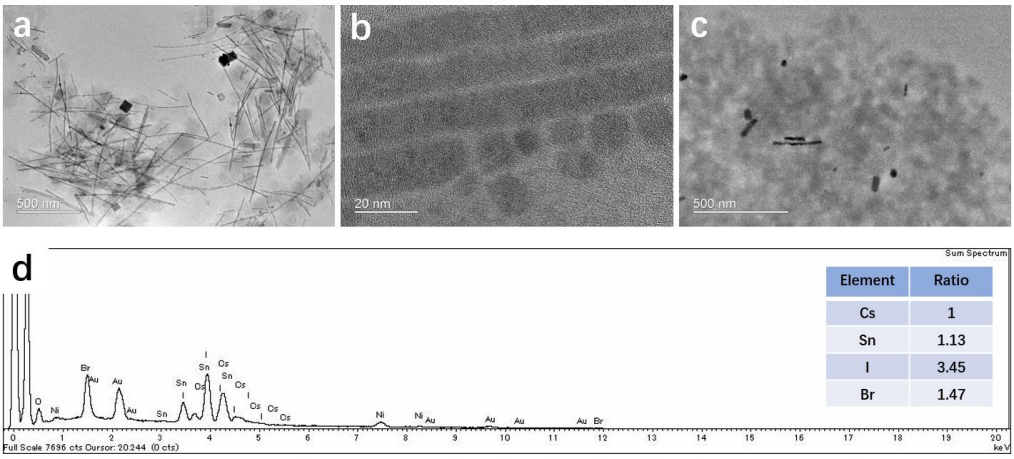

Figure 4.15 (a) TEM image and (b) HETEM image, and (d) SEM-EDS spectrum with elemental quantitative data of $CsSn(I/Br)_3$ NWs synthesized with 50 µL of OAmBr. It is clearly observed in (b) that cubic NCs are assembling into NWs. (c) TEM image of $CsSn(I/Br)_3$ NCs synthesized with 100 µL of OAmBr

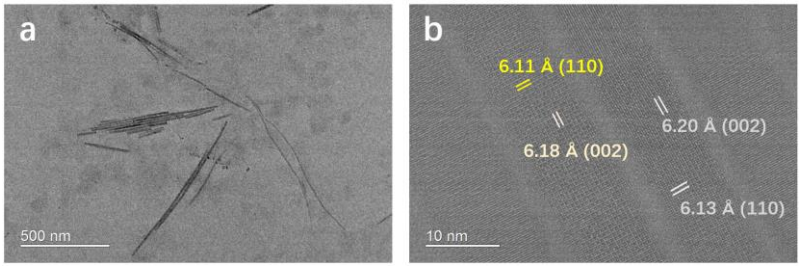

Figure 4.16 (a) TEM image and (b) HETEM image of $CsSnI_3$ NWs synthesized with OAmI.

Additionally, I examined the elemental composition of these $CsSn(I/Br)_3$ NWs, particularly the ratio of I to Br. SEM-EDS analysis revealed that the ratio of Cs/Sn/I/Br was 1/1.13/3.45/1.47, with Br/I ratio being 2.1/0.9 (**Figure 4.15d**). Therefore, the molecular formula of these NCs is suggested to be $CsSnI_{2.1}Br_{0.9}$. I then increased the

amount of OAmBr to 100 μL; unfortunately, excessive OAmBr led to the decomposition of most $CsSnI_3$ NCs, and only products with low contrast could be observed by TEM (**Figure 4.15c**). Nevertheless, I have demonstrated that the Ion exchange method is not limited to $CsSnI_3$ NCs but can be extended to the synthesis of other tin halide perovskites with high PLQY.

4.4 Conclusion

In summary, the synthesis of high-quality $CsSnI_3$ NCs through the ion exchange method using $Sn(Oct)_2$ has been successfully demonstrated. The addition of $Sn(Oct)_2$ significantly impacts the photophysical properties of the resulting $CsSnI_3$ NCs, with optimal luminous efficiency achieved, resulting in a PLQY of 49.7% ,which is the highest reported efficiency for $CsSnI_3$ NCs to date. Moreover, I have shown that $Sn(Oct)_2$ accelerates the reaction rate during $CsSnI_3$ synthesis compared to conditions without $Sn(Oct)_2$. The timing of $Sn(Oct)_2$ injection is crucial, as both early and late additions severely impact the reaction rate, leading to a reduction in PLQY. Additionally, leveraging high-quality $CsSnI_3$ NCs as the foundation, I successfully employed anion exchange to obtain $CsSnI_{2.1}Br_{0.9}$ NWs with efficient luminescence. Overall, this study provides valuable insights into the synthesis mechanism and optimization strategies for achieving high-efficiency luminescence in $CsSnX_3$ NCs, thereby opening avenues for their potential applications in optoelectronic devices and photovoltaics.

Reference

(1) Jellicoe, T. C.; Richter, J. M.; Glass, H. F. J.; Tabachnyk, M.; Brady, R.; Dutton, S. E.; Rao, A.; Friend, R. H.; Credgington, D.; Greenham, N. C.; et al. Synthesis and Optical Properties of Lead-Free Cesium Tin Halide Perovskite Nanocrystals. *Journal of the American Chemical Society* **2016**, *138* (9), 2941-2944.

(2) Chung, I.; Song, J.-H.; Im, J.; Androulakis, J.; Malliakas, C. D.; Li, H.; Freeman, A. J.; Kenney, J. T.; Kanatzidis, M. G. CsSnI3: Semiconductor or Metal? High Electrical Conductivity and Strong Near-Infrared Photoluminescence from a Single Material. High Hole Mobility and Phase-Transitions. *Journal of the American Chemical Society* **2012**, *134* (20), 8579-8587.

(3) Tao, S.; Schmidt, I.; Brocks, G.; Jiang, J.; Tranca, I.; Meerholz, K.; Olthof, S. Absolute energy level positions in tin- and lead-based halide perovskites. *Nature Communications* **2019**, *10* (1), 2560.

(4) Huang, L.-y.; Lambrecht, W. R. Electronic band structure, phonons, and exciton binding energies of halide perovskites $CsSnCl_3$, $CsSnBr_3$, and $CsSnI_3$. *Physical Review B* **2013**, *88* (16), 165203.

(5) Kang, C.; Rao, H.; Fang, Y.; Zeng, J.; Pan, Z.; Zhong, X. Antioxidative Stannous Oxalate Derived Lead-Free Stable $CsSnX_3$ (X=Cl, Br, and I) Perovskite Nanocrystals. *Angewandte Chemie International Edition* **2021**, *60* (2), 660-665.

(6) Wong, A. B.; Bekenstein, Y.; Kang, J.; Kley, C. S.; Kim, D.; Gibson, N. A.; Zhang, D.; Yu, Y.; Leone, S. R.; Wang, L.-W.; et al. Strongly Quantum Confined Colloidal Cesium Tin Iodide Perovskite Nanoplates: Lessons for Reducing Defect Density and Improving Stability. *Nano Letters* **2018**, *18* (3), 2060-2066.

(7) Liu, Q.; Yin, J.; Zhang, B.-B.; Chen, J.-K.; Zhou, Y.; Zhang, L.-M.; Wang, L.-M.; Zhao, Q.; Hou, J.; Shu, J.; et al. Theory-Guided Synthesis of Highly Luminescent Colloidal Cesium Tin Halide Perovskite Nanocrystals. *Journal of the American Chemical Society* **2021**, *143* (14), 5470-5480.

(8) Li, Y.; Wang, D.; Yang, Y.; Ding, C.; Hu, Y.; Liu, F.; Wei, Y.; Liu, D.; Li, H.; Shi,

G.; et al. Stable Inorganic Colloidal Tin and Tin–Lead Perovskite Nanocrystals with Ultralong Carrier Lifetime via Sn(IV) Control. *Journal of the American Chemical Society* **2024**.

(9) Cao, L.; Gu, S.-M.; Liu, B.; Huang, L.; Zhang, J.; Zhu, Y.; Wang, J. Highly Ambient Stable CsSnBr3 Perovskite via a New Facile Room-Temperature "Coprecipitation" Strategy. *ACS Applied Materials & Interfaces* **2023**, *15* (25), 30409-30416.

(10) Chen, J.; Wu, H.; Huang, Y.; Xu, J.; Lu, X.; Zhou, W.; Song, J.; Huang, R. Effect of CrF_3 Addition on Photoluminescence Properties of Lead-Free $Cs_4SnBr_{6-x}F_x$ Zero-Dimensional Perovskite. *Materials* **2023**, *16* (18), 6309.

(11) Protesescu, L.; Yakunin, S.; Bodnarchuk, M. I.; Krieg, F.; Caputo, R.; Hendon, C. H.; Yang, R. X.; Walsh, A.; Kovalenko, M. V. Nanocrystals of Cesium Lead Halide Perovskites ($CsPbX_3$, X = Cl, Br, and I): Novel Optoelectronic Materials Showing Bright Emission with Wide Color Gamut. *Nano Letters* **2015**, *15* (6), 3692-3696.

(12) Xu, H.; Yuan, H.; Duan, J.; Zhao, Y.; Jiao, Z.; Tang, Q. Lead-free $CH_3NH_3SnBr_{3-x}I_x$ perovskite quantum dots for mesoscopic solar cell applications. *Electrochim. Acta* **2018**, *282*, 807-812.

(13) Peng, C.; Zhang, R.; Chen, H.; Liu, Y.; Zhang, S.; Fang, T.; Guo, R.; Zhang, J.; Shan, Q.; Jin, Y. A Demulsification–Crystallization Model for High-Quality Perovskite Nanocrystals. *Advanced Materials* **2023**, *35* (2), 2206969.

(14) Li, F.; Cao, L.; Shi, S.; Gao, H.; Song, L.; Geng, C.; Bi, W.; Xu, S. Controlled growth of $CH_3NH_3PbBr_3$ perovskite nanocrystals via a water–oil interfacial synthesis method. *Angewandte Chemie International Edition* **2019**, *58* (49), 17631-17635.

(15) Akkerman, Q. A.; Nguyen, T. P.; Boehme, S. C.; Montanarella, F.; Dirin, D. N.; Wechsler, P.; Beiglböck, F.; Rainò, G.; Erni, R.; Katan, C. Controlling the nucleation and growth kinetics of lead halide perovskite quantum dots. *Science* **2022**, *377* (6613), 1406-1412.

(16) Li, X.; Zhang, K.; Li, J.; Chen, J.; Wu, Y.; Liu, K.; Song, J.; Zeng, H.

Heterogeneous nucleation toward polar-solvent-free, fast, and one-pot synthesis of highly uniform perovskite quantum dots for wider color gamut display. *Advanced Materials Interfaces* **2018**, *5* (8), 1800010.

(17) Zhang, B.-B.; Chen, J.-K.; Zhang, C.; Shirahata, N.; Sun, H.-T. Mechanistic Insight into the Precursor Chemistry of Cesium Tin Iodide Perovskite Nanocrystals. *ACS Materials Letters* **2023**, *5* (7), 1954-1961.

(18) Wang, F.; Jiang, X.; Chen, H.; Shang, Y.; Liu, H.; Wei, J.; Zhou, W.; He, H.; Liu, W.; Ning, Z. 2D-quasi-2D-3D hierarchy structure for tin perovskite solar cells with enhanced efficiency and stability. *Joule* **2018**, *2* (12), 2732-2743.

(19) Meng, X.; Lin, J.; Liu, X.; He, X.; Wang, Y.; Noda, T.; Wu, T.; Yang, X.; Han, L. Highly stable and efficient $FASnI_3$-based perovskite solar cells by introducing hydrogen bonding. *Advanced Materials* **2019**, *31* (42), 1903721.

(20) Li, P.; Dong, H.; Xu, J.; Chen, J.; Jiao, B.; Hou, X.; Li, J.; Wu, Z. Ligand orientation-induced lattice robustness for highly efficient and stable tin-based perovskite solar cells. *ACS Energy Letters* **2020**, *5* (7), 2327-2334.

(21) Liu, Q.; Yin, J.; Zhang, B.-B.; Chen, J.-K.; Zhou, Y.; Zhang, L.-M.; Wang, L.-M.; Zhao, Q.; Hou, J.; Shu, J. Theory-guided synthesis of highly luminescent colloidal cesium tin halide perovskite nanocrystals. *Journal of the American Chemical Society* **2021**, *143* (14), 5470-5480.

(22) Ke, W.; Stoumpos, C. C.; Kanatzidis, M. G. "Unleaded" perovskites: status quo and future prospects of tin-based perovskite solar cells. *Advanced Materials* **2019**, *31* (47), 1803230.

(23) Savill, K. J.; Ulatowski, A. M.; Herz, L. M. Optoelectronic properties of tin–lead halide perovskites. *ACS Energy Letters* **2021**, *6* (7), 2413-2426.

(24) Yang, W. F.; Igbari, F.; Lou, Y. H.; Wang, Z. K.; Liao, L. S. Tin halide perovskites: progress and challenges. *Advanced Energy Materials* **2020**, *10* (13), 1902584.

(25) Jellicoe, T. C.; Richter, J. M.; Glass, H. F.; Tabachnyk, M.; Brady, R.; Dutton, S. E.; Rao, A.; Friend, R. H.; Credgington, D.; Greenham, N. C. Synthesis and optical

properties of lead-free cesium tin halide perovskite nanocrystals. *Journal of the American Chemical Society* **2016**, *138* (9), 2941-2944.

(26) Wang, A.; Guo, Y.; Muhammad, F.; Deng, Z. Controlled Synthesis of Lead-Free Cesium Tin Halide Perovskite Cubic Nanocages with High Stability. *Chemistry of Materials* **2017**, *29* (15), 6493-6501.

(27) Weidman, M. C.; Seitz, M.; Stranks, S. D.; Tisdale, W. A. Highly Tunable Colloidal Perovskite Nanoplatelets through Variable Cation, Metal, and Halide Composition. *ACS Nano* **2016**, *10* (8), 7830-7839.

(28) Chen, M. Y.; Lin, J. T.; Hsu, C. S.; Chang, C. K.; Chiu, C. W.; Chen, H. M.; Chou, P. T. Strongly Coupled Tin-Halide Perovskites to Modulate Light Emission: Tunable 550–640 nm Light Emission (FWHM 36–80 nm) with a Quantum Yield of up to 6.4%. *Advanced Materials* **2018**, *30* (20), 1706592.

(29) Nedelcu, G.; Protesescu, L.; Yakunin, S.; Bodnarchuk, M. I.; Grotevent, M. J.; Kovalenko, M. V. Fast Anion-Exchange in Highly Luminescent Nanocrystals of Cesium Lead Halide Perovskites ($CsPbX_3$, X = Cl, Br, I). *Nano Letters* **2015**, *15* (8), 5635-5640.

(30) Woo, J. Y.; Kim, Y.; Bae, J.; Kim, T. G.; Kim, J. W.; Lee, D. C.; Jeong, S. Highly Stable Cesium Lead Halide Perovskite Nanocrystals through in Situ Lead Halide Inorganic Passivation. *Chemistry of Materials* **2017**, *29* (17), 7088-7092.

(31) Chen, D.; Zhou, S.; Fang, G.; Chen, X.; Zhong, J. Fast Room-Temperature Cation Exchange Synthesis of Mn-Doped $CsPbCl_3$ Nanocrystals Driven by Dynamic Halogen Exchange. *ACS Applied Materials & Interfaces* **2018**, *10* (46), 39872-39878.

(32) Chiba, T.; Hayashi, Y.; Ebe, H.; Hoshi, K.; Sato, J.; Sato, S.; Pu, Y.-J.; Ohisa, S.; Kido, J. Anion-exchange red perovskite quantum dots with ammonium iodine salts for highly efficient light-emitting devices. *Nature Photonics* **2018**, *12* (11), 681-687.

(33) Li, J.; Xu, L.; Wang, T.; Song, J.; Chen, J.; Xue, J.; Dong, Y.; Cai, B.; Shan, Q.; Han, B.; et al. 50-Fold EQE Improvement up to 6.27% of Solution-Processed All-Inorganic Perovskite $CsPbBr_3$ QLEDs via Surface Ligand Density Control. *Advanced Materials* **2017**, *29* (5), 1603885.

(34) Li, H.; Pokhrel, S.; Schowalter, M.; Rosenauer, A.; Kiefer, J.; Mädler, L. The gas-phase formation of tin dioxide nanoparticles in single droplet combustion and flame spray pyrolysis. *Combust. Flame* **2020**, *215*, 389-400.

(35) Park, H.-H.; Law, W. L.; Zhang, X.; Hwang, S.-Y.; Jung, S. H.; Shin, H.-B.; Kang, H. K.; Park, H.-H.; Hill, R. H.; Ko, C. K. Facile Size-Tunable Fabrication of Functional Tin Dioxide Nanostructures by Multiple Size Reduction Lithography. *ACS Applied Materials & Interfaces* **2012**, *4* (5), 2507-2514.

(36) Mahesh, K. P. O.; Chang, C.-Y.; Hong, W.-L.; Wen, T.-H.; Lo, P.-H.; Chiu, H.-Z.; Hsu, C.-L.; Horng, S.-F.; Chao, Y.-C. Lead-free cesium tin halide nanocrystals for light-emitting diodes and color down conversion. *RSC Advances* **2020**, *10* (61), 37161-37167.

Chapter 5 Conclusions and Future Prospects

5.1 General conclusions

In recent years, colloidal halide perovskite nanocrystals (NCs) have attracted significant attention due to their remarkable optoelectronic properties, including tunable bandgaps, high photoluminescence efficiency, and substantial absorption coefficients. These properties have led to their widespread adoption in various optoelectronic applications, such as lasers, displays, light-emitting diodes (LEDs), scintillators, and photovoltaics. However, as research into the potential of metal halide perovskite NCs in optoelectronic devices progresses, there is a growing need to address safety concerns associated with lead exposure in lead-based halide perovskite materials. Consequently, there is increasing interest in identifying lead-free alternatives, with tin halide perovskites emerging as promising candidates due to their lower toxicity and comparable perovskite-like characteristics. Nevertheless, recent investigations in the field of perovskite materials highlight the significant challenge of achieving high photoluminescence performance in the synthesis of colloidal $CsSnX_3$ perovskite NCs. This challenge underscores the need for further exploration and refinement of synthesis methodologies to unlock the full potential of these materials for next-generation optoelectronic applications.

In this study, I initially delve into the synthesis mechanism and precursor chemistry involved in the formation of tin halide perovskite NCs. Subsequently, armed with valuable insights gained from these investigations, I proceed to devise effective synthetic methodologies conducive to yielding high-quality tin halide perovskite NCs. Herein, I present the detailed findings of my research:

Firstly, in my investigation of representative tin halide perovskite NCs, particularly $CsSnI_3$ NCs, I delved into the precursor chemistry involved in the commonly employed hot-injection method for their synthesis. Understanding the intricacies of precursor chemistry is vital for optimizing the synthesis process and enhancing the quality of the resulting NCs. Previous reports have detailed the synthesis of CsSnI3 NCs using Tin(II)

2-ethylhexanoate [$Sn(Oct)_2$] and trimethylsilyl iodide (TMSI) as precursors under tin- and iodine-rich conditions, resulting in record photoluminescence quantum yield (PLQY) levels. However, subsequent attempts to improve the quality of $CsSnI_3$ NCs have been limited, largely due to a lack of comprehensive understanding regarding the underlying reaction mechanisms and precursor interactions.

Our study uncovered a significant aspect of the reaction mechanism involving the tin-iodide precursor. Specifically, I observed that iodides in the tin-iodide precursor react with $Sn(Oct)_2$, the tin source, to form intermediate products known as polymeric alkanoate iodides. Through detailed analysis using nuclear magnetic resonance (NMR) spectroscopy, I elucidated the pivotal role of these intermediate products in modulating the reactivity of the tin-iodide precursor. This intermediate product, in turn, influences various characteristics of $CsSnI_3$ NCs, including their PLQY, size, morphology, and uniformity. In short, my findings underscore the critical importance of understanding precursor chemistry and reaction mechanisms in the synthesis of tin halide perovskite NCs. Furthermore, I also highlight the potential significance of manipulating precursor reactivity or controlling reaction rates to enhance the quality and properties of these NCs.

Secondly, my development of a simple phase transition synthesis method based on cation exchange for producing cesium tin halide perovskite NCs. Taking the synthesis of $CsSnI_3$ NCs as a case study, I initiated the process by preparing the SnI_2-TOP precursor using SnI_2 and TOP, while simultaneously synthesizing CsI NCs via the reaction of iodides and cesium oleate. Subsequently, by carefully mixing the SnI_2-TOP precursor with CsI NCs under optimized conditions, I successfully obtained high-quality $CsSnI_3$ NCs.

Remarkably, these $CsSnI_3$ NCs exhibited a remarkable PLQY of 34.4%, surpassing the previously reported maximum of 18.4%. Furthermore, employing this synthesis method enabled us to achieve $CsSnI_3$ NCs with tunable sizes ranging from 14 nm to 23 nm, or even larger, while maintaining efficient luminescence properties. Notably, the resulting $CsSnI_3$ NCs demonstrated excellent size uniformity, leading to narrow

photoluminescence peaks, , which is crucial in optoelectronic applications such as LEDs.

The success of this synthetic approach can be attributed to its controlled reaction kinetics, allowing for a slowly phase transition process. In this context, I conducted in-depth investigations into the mechanism underlying the phase transition induced by cation exchange. Finally, to showcase the versatility of this synthetic strategy, I extended my efforts to synthesize $CsSnBr_3$ perovskite NCs, demonstrating its applicability beyond $CsSnI_3$ system.

Finally, based on my in-depth understanding of the synthesis mechanism of tin halide perovskite NCs and their precursor chemistry, as well as more suitable synthetic method I found, I have succeeded in preparing higher-quality tin halide perovskite NCs through controlled ion exchange processes. By incorporating $Sn(Oct)_2$ during the ion exchange synthesis of $CsSnI_3$ NCs, I effectively modulated the reaction rate. Utilizing in-situ photoluminescence (PL) and high-resolution transmission electron microscopy (HRTEM), I observed that $Sn(Oct)_2$ facilitated the acceleration of the reaction rate by stripping the surface layer structure of the NCs. However, despite this enhancement, the synthesis rate remained slower compared to conventional methods like hot injection, a crucial factor for improving crystal quality.

Subsequent analysis using techniques such as X-ray photoelectron spectroscopy (XPS) revealed that the $CsSnI_3$ NCs synthesized at this controlled reaction rate exhibited fewer uncoordinated Sn and I atoms, contributing to a maximum PLQY of approximately 50%. Furthermore, my exploration extended to the synthesis of high-quality tin halide perovskite NCs with other halide compositions through anion exchange. Intriguingly, anion exchange prompted the self-assembly of tin-based perovskite NCs, leading to the formation of $CsSnI_{2.1}Br_{0.9}$ nanowires characterized by a width of approximately 13 nm and lengths approaching micrometers. These $CsSnI_{2.1}Br_{0.9}$ nanowires exhibited a PLQY of 34.4%, with noticeable blue-shifted emission (892 nm) compared to $CsSnI_3$ NCs. In summary, my findings underscore the efficacy of controlled cation exchange and anion exchange methods in obtaining high-quality tin halide perovskite NCs, offering insights

into the synthesis and manipulation of these materials for various optoelectronic applications.

5.2 Future prospects

While achieving $CsSnI_3$ NCs with a PLQY nearing 50% marks a significant milestone, several challenges persist in the realm of tin halide perovskite nanomaterials research. One crucial aspect is the synthesis of a higher-quality series of tin halide perovskite NCs with varied emission wavelengths. Needed a deeper comprehension of defect formation principles and synthesis processes specific to tin halide perovskite NCs. Such insights will enable the development of more suitable synthesis methods to procure high-quality tin halide perovskite NCs.

Another pressing challenge lies in enhancing the stability of tin halide perovskite materials, a paramount factor for their viability in optoelectronic devices. Tin halide perovskite materials often suffer from poor stability, and effective strategies to bolster their structural and optical stability in various environmental conditions remain elusive.

Furthermore, the realization of high-quality optoelectronic devices leveraging tin halide perovskite nanomaterials has yet to be achieved. Despite their promising semiconductor luminescent properties and suitable bandgap, tin halide perovskites have encountered hurdles in transitioning to practical applications such as solar cells, near-infrared displays, or biotechnology. The slow progress in material quality enhancement has impeded the advancement of tin halide perovskites in optoelectronic applications. Addressing these challenges will be pivotal in unlocking the full potential of tin halide perovskites for diverse optoelectronic applications.

In conclusion, the future of tin halide perovskite material is marked by unprecedented opportunities for innovation and advancement across multiple fronts.

Acknowledgements

I extend my deepest gratitude to Prof. Shirahata and Prof. Sun for their invaluable guidance, unwavering support, and insightful feedback throughout my research journey.

I am immensely grateful to my laboratory colleagues: Ms. Kobayashi, Ms. Takazawa, Ms. Soga, Dr. Nemoto, Dr. Yamada, and Dr. Subhashri for their help, as well as our collaborative, and stimulating discussions, which have significantly enriched my research experience.

Special thanks are owed to my dear friends and classmates: Chen Jiakai, Zhang Cong, Ming Hong, Chen Dongxun, and Dr. Huang Xiaoyu. Their friendship, unwavering support, and shared insights have illuminated my academic path and infused it with joy and camaraderie.

Lastly, I express my heartfelt appreciation to my family and friends whose unwavering support, understanding, and encouragement have been my pillars of strength throughout this academic endeavor.

感怀之情，辞藻难尽，笔墨难书，惟有涕零。

ZHANG Binbin

May 7th, 2024

Tsukuba, Japan